THE UNIVERSITY OF CHICAGO

COHERENCE AND CHIRALITY IN ENERGY TRANSFER DYNAMICS OF LIGHT HARVESTING ANTENNA COMPLEXES

A DISSERTATION SUBMITTED TO
THE FACULTY OF THE DIVISION OF THE PHYSICAL SCIENCES
IN CANDIDACY FOR THE DEGREE OF
DOCTOR OF PHILOSOPHY

DEPARTMENT OF CHEMISTRY

BY
VED PRAKASH SINGH

CHICAGO, ILLINOIS
JUNE 2016

To Nitai

"A scientific truth does not triumph by convincing its opponents and making them see the light, but rather because its opponents eventually die and a new generation grows up that is familiar with it."

- *Max Planck*

TABLE OF CONTENTS

LIST OF FIGURES viii

ACKNOWLEDGMENTS x

ABSTRACT xiv

1 PHOTOSYNTHESIS AND ENERGY TRANSFER EFFICIENCY 1
- 1.1 Photosynthesis: An overview 1
- 1.2 Light harvesting unit of purple bacteria 3
- 1.3 Light Harvesting complex 2 (LH2) 5
  - 1.3.1 Building blocks: Bacteriochlorophyll a 5
  - 1.3.2 Physical and electronic structure of LH2 7
- 1.4 Energy transfer mechanisms 10
  - 1.4.1 Förster Resonance Energy Transfer 11
  - 1.4.2 Redfield mechanism of energy transfer 13
- 1.5 References 14

2 LINEAR AND NON-LINEAR SPECTROSCOPY 16
- 2.1 2D Spectrum of a two state system 17
- 2.2 2D spectrum of a three state system 18
- 2.3 Advantages of 2D Electronic spectroscopy 20
  - 2.3.1 Distinguishing between homogeneous and inhomogeneous broadening 20
  - 2.3.2 Observing Excited state dynamics 22
- 2.4 References 24

3 FORMALISM OF SPECTROSCOPY 26
- 3.1 Ultrafast pulses, eigenstates and emitted field 26
- 3.2 Density Matrix 30
  - 3.2.1 Introduction to density matrix 30
  - 3.2.2 Time Evolution of density matrix 32
  - 3.2.3 Interaction picture and perturbation theory 32
- 3.3 Polarization 34
- 3.4 Rotating wave approximation and Feynman pathways 36
  - 3.4.1 Linear Response function and a two level system 36
  - 3.4.2 Rotating wave approximation 39
  - 3.4.3 Feynman diagrams for linear response functions 40
  - 3.4.4 Feynman diagrams for 3^{rd} order non-linear response functions 42
- 3.5 2D Electronic Spectroscopy 43
  - 3.5.1 Design of a two-dimensional electronic spectrometer 44
  - 3.5.2 GRAPES 49
- 3.6 References 50

4 GRAPES AND INDEPENDENT PHASING OF REPHASING AND NON-REPHASING SPECTROSCOPIC SIGNALS . . . 51
4.1 Introduction . . . 51
4.2 Theory . . . 53
4.3 Experimental Methods . . . 56
4.4 Results and discussion . . . 60
4.5 Conclusion . . . 63
4.6 Appendix . . . 63
4.6.1 Pulse ordering in GRAPES . . . 63
4.6.2 Contributions to rephasing signal for finite duration pulses . . . 64
4.6.3 Power variations along the length of the beam . . . 66
4.6.4 Expanded Derivation of Equations in Theory section . . . 66
4.7 References . . . 68

5 QUANTIFYING COHERENCE IN PHOTOSYNTHETIC ANTENNA COMPLEXES 72
5.1 Introduction . . . 72
5.2 Experiment . . . 73
5.2.1 Optical apparatus . . . 73
5.2.2 Sample Preparation . . . 74
5.3 Results . . . 75
5.3.1 Incoherent dynamics . . . 76
5.3.2 Coherent dynamics . . . 76
5.4 Theoretical Model . . . 80
5.5 Discussion . . . 84
5.6 Conclusion . . . 87
5.7 Appendix . . . 88
5.7.1 Linear absorption spectrum of R26.1 LH2 and excitation laser spectrum 88
5.7.2 Derivation of rate constants for NBO states . . . 88
5.7.3 Orientation of transition dipoles of R26.1 LH2 . . . 94
5.7.4 Estimating mixing of vibrational and electronic states . . . 95
5.7.5 Comparison of signals stemming from different transition dipoles . . . 98
5.7.6 Incoherent dynamics from $B850^*$ states to $B850$ states . . . 100
5.7.7 Non-linear regression of coherence signals confidence in fit parameters 101
5.8 References . . . 103

6 OBSERVATION OF ENHANCED CIRCULAR DICHROISM AND CHIRAL DYNAMICS IN LH2 . . . 109
6.1 Introduction . . . 109
6.2 Results and discussion . . . 111
6.3 Methods . . . 116
6.3.1 Sample Preparation . . . 116
6.3.2 IR144 control along with LH2 . . . 116
6.3.3 Two-dimensional electronic spectroscopy . . . 117
6.3.4 Controlling and analyzing polarization of pulses . . . 117
6.4 References . . . 118

7 FUTURE DIRECTIONS 120
7.1 Development of broad band Chiral Two-Dimensional Electronic Spectroscopy 120
7.2 Simultaneous study of photosynthetic antenna complexes and metal nanoparticles 123
7.3 References 124

8 CONCLUSIONS 125

LIST OF FIGURES

1.1 Cartoon representation of an invagination in purple bacteria's cell membrane . . 4
1.2 Bacteriochlorophyll a and its absorption spectrum 6
1.3 Physical structure of LH2 with membrane and cytoplasmic view 8
1.4 Absorption spectrum and electronic structure of LH2 9
1.5 Configuration of bacteriochlorophylls 11
1.6 Förster Resonance Energy Transfer mechanism 12
1.7 Redfield mechanism of energy transfer 13

2.1 Linear absorption spectrum of a three-state system 16
2.2 Linear and 2D spectrum of simple two state system 18
2.3 2D spectrum of the simplest multi-state system 19
2.4 Comparison of homogeneously and in-homogeneously broadened spectra 21
2.5 Signature of spectral diffusion in a 2D spectrum 21
2.6 Observing energy transfer dynamics using 2D spectrum 23

3.1 Ultrafast laser pulses 27
3.2 Time ordering in perturbative expansion in the interaction picture 33
3.3 Time intervals for evaluating n^{th} order polarization 35
3.4 Feynman diagrams for linear response function explaining the rotating wave approximation 41
3.5 Feynman diagrams for 3^{rd} order non-linear response function for a two state system that survive rotating wave approximation 43
3.6 Feynman diagram enumerating phase evolution as as function of time during different time intervals 44
3.7 An overview of the laser setup with all the important components 46
3.8 White light after argon gas tube and light-filament after chirp mirrors 46
3.9 Time controllers for the individual pulses. 48
3.10 Phase matching at the position of the sample position 48
3.11 Pulses in GRAPES 49

4.1 Comparison of projection of simulated 2D spectrum to frequency resolved pump probe spectra. 55
4.2 Optical apparatus to acquire rephasing and non-rephasing signals from GRAPES. 58
4.3 Raw rephasing and non-rephasing signals from GRAPES. 59
4.4 Comparison of experimental 2D rephasing and non-rephasing spectra to pump probe data. 61
4.5 Comparison of experimental 2D rephasing and non-rephasing spectra to pump probe data. 62
4.6 Pulse ordering in GRAPES 64
4.7 Feynman diagram for overlapping pulses 65

5.1 2D ES of R26.1 LH2 for Canonical and Coherence specific sequence. 77
5.2 Incoherent dynamics of R26.1 LH2 from Canonical sequence. 77

5.3 Coherence signals from canonical and coherence specific sequence observed in R26.1 LH2 78
5.4 Mixing of Born-Oppenheimer states to give non-Born-Oppenheimer states. . . . 81
5.5 Theoretical calculation to estimate vibronic coherence 86
5.6 Linear absorption spectrum of R26.1 LH2, and its cartoon representation 88
5.7 Mixing of Born-Oppenheimer states to give non-Born-Oppenheimer states . . . 89
5.8 Angle between transition dipoles of LH2 95
5.9 Mixing of Born-Oppenheimer states and their transition dipoles 97
5.10 Comparing diagonal and off-diagonal signals under different polarization excitation conditions 99
5.11 Lower off-diagonal peak for energy transfer from $B850^*$ states to $B850$ states . . 101
5.12 Coherence signal nonlinear regression 102

6.1 2D map of LH2 acquired with LYYY and RYYY polarization scheme 112
6.2 Dynamics of LH2 and IR144 with LYYY and RYYY polarization scheme 112
6.3 Dynamics of LH2 with LYYY and RYYY polarization scheme, acquired with regen pulse 114
6.4 Power dependent studies of LH2 with LYYY and RYYY 115

7.1 Old geometry of GRAPES for doing Chiral Two-Dimensional Electronic Spectroscopy 121
7.2 New geometry of GRAPES for doing Chiral Two-Dimensional Electronic Spectroscopy 122
7.3 Comparison of current C2DES and proposed broadband C2DES with GRAPES at the sample position 123

ACKNOWLEDGMENTS

I would like to express my deep gratitude to the many people who have nurtured me in various ways throughout my graduate studies. First and foremost, I would like to thank my advisor Professor Greg Engel. Greg's enthusiasm is viral and I picked it up whenever I needed motivation. And like any graduate student, I would need it many times and Greg was there to help. He was constantly encouraging his graduate students to come up with their own research ideas and he was happy to invest in them.

I want to thank my committee members, Professors David Mazziotti and Andrei Tokmakoff. Professor Mazziotti's class instilled me with a better understanding of quantum mechanics, which I found very useful later on when I had to put on a theorist's cap for work on coherent energy transfer. His enthusiasm as a teacher is always inspiring. I also had the great fortune of interacting with Professor Tokmakoff. I learned a lot of ultrafast spectroscopy from his comprehensive notes even before I had a chance to meet him in person. I had the opportunity to talk to him about my latest work on chiral two-dimensional electronic spectroscopy. He provided me with feedback which I found very helpful in advancing my understanding of physical phenomena observed through ultrafast spectroscopy.

My scientific career as a graduate student would not be possible without the help of my fellow senior graduate students, most notably Andrew Fidler. Andrew is a remarkable person for many reasons. He is very calm and composed, even in the most testing situations. And in an ultrafast lab such testing situations are aplenty. He set a very high standard of work ethic through his personal example. He was good with experiments and his skills with lasers were useful to many other graduate students. He had a good grasp of the theory of spectroscopy, quantum mechanics and ultrafast phenomena. The perfect combination of experimental skills and theoretical finesse enabled Andrew to ask new scientific questions, perform the right kind of experiments and also do theoretical work to explain the experimental results. I found him to be a very inspiring person and imbibed, as much as I could, of what he tried to teach me.

My learning was also immensely enriched by other graduate students such as Justin Caram, Dugan Hayes and Phil Long. Justin is a perfect example of how one could try his hands at different things as he worked with biological samples, quantum dots, instrument development and theory. He tackled a wide spectrum of topics and it was inspiring to see how he switched form one topic to the other with great ease. Dugan took the group in a whole new direction by designing molecules and also synthesizing them to study their ultrafast coherent dynamics. He too was an example of how to go in new directions to answer important scientific questions. Phil, just like Andrew, was extremely patient in training me as an experimentalist. He was a pioneer in the lab when it came to growing biological samples. Phil's work made it possible for the group to study biophysics of LH2.

While it was fun to struggle and learn from senior graduate students, it was immensely satisfying to teach new members of the group. These were post-doctoral scholars, graduate, undergraduate and high-school students. Cheng "Wave" Wang joined the group as a post-doctoral scholar. He came in as a synthetic inorganic chemist. It was a great learning experience to mentor him on ultrafast experiments and theory of spectroscopy. With Wave, I did some of the most important experiments of my graduate career, which I believe brought about a fundamental understanding of coherent phenomena in energy transfer process. Wave and I had numerous conversations on a new form of spectroscopy to detect the effect of chirality on dynamics of photosynthetic antenna complexes. The idea for these new experiments came from Andrew's chiral two-dimensional electronic spectroscopy, but I needed Wave's scientific curiosity to polish them. After working with me for a while, Wave started working with others and mentoring them. Wave was so brilliant that not only he quickly picked up the basics but he got so good at it that it was difficult for others to keep up with him. Wave is truly a perfect combination of brilliance and humility, and that made him an appealing person. Wave is now a professor at Xiamen University, China. Tobias Gellen was an undergraduate student in the group and he was eager to learn and tackle new problems. Within a period of three months, Tobias not only learned a new programming

language but also used it to help me with important calculations that ultimately led to a concrete understanding of how to think of vibronic coupling in photosynthetic antenna complexes. It was also a pleasure working with Po-Chieh Ting. As a rising second year graduate student, Po-Chieh showed the courage of thinking of new ideas and investing in new experiments. While still early in his career, he has been instrumental in creating knowledge for chiral two-dimensional electronic spectroscopy. I had the opportunity to work with Ishaan Dayal, who is a high school student. I was inspired by how quick he was in picking up new problems and making significant progress on the same. I wish him the best in his future endeavors.

I would like to thank the rest of the Engel group who have been a pleasure to work and share my office with: Dr. Brian Rolczynski, Polina Navotnaya, Peter Dahlberg, Sara Massey, Hunter Davis, Moira Flanagan, Dr. Kelly Fransted, Dr. Graham Griffin, Lane Gunderman, Dr. Tom Jarvis, Amir Khadivi, Nick Lewis, Alex Linkin, Ryan McGillicuddy, Dr. Gitt Panitchayangkoon, Dr. Subha Viswanathan, Michael Westberg Sørensen, Lili Wang, Haibin Zheng, Marco Allodi, RJ Bogdan, Thomas Gao, Ruvim Ginzburg, Sean Harding, Sara Hess, Nanzhu Li, Richard Mazuski, Jonathan Michelsen, John Otto, Hallie Sussman, Matthew Talaga, Nick Williams, Ryan Wood, Alice Zhang, Sara Wichner, Elad Harel and Pegg Anderson.

I cannot overemphasize the influence of my mentors from my undergraduate college in helping me deciding to go for higher education. As my faculty advisor Prof. Raghavan B. Sunoj, a.k.a ChemOrbitals, was a constant source of motivation, instilling in his students the same enthusiasm that he had for science. His enthusiasm for teaching showed up in his personality and made us all experience the fun in science. As my junior and senior thesis advisor Prof. Sambhu N. Datta, a.k.a Sam, instilled in me what any theorist would in his student - the need to keep an eye on the problem and then take minimum but sufficient steps to solve it. Later on in my graduate career this approach to problem solving was very instrumental in effectively tacking problems. I cannot miss the opportunity to mention a

few of my teachers from my middle and high school. Rita Singhal, Pinky Shrivastava and Shivana Arora were some of the teachers who showed confidence in me which was a source of motivation.

My stay in Chicago has been immensely enriched by my friends, most notably Abhishek Ghosh and my friends in the cricket club.

Last but not least, I would like to thank my mom and my dad for raising me up the way they did. Despite their humble upbringing, they did their best to provide resources to me. Of all the gifts that they have given me, the most precious is the desire to dream the impossible. And they have raised me to develop self-confidence that is born out of humility, fierce determination and lack of sense of entitlement; something they do not fail to remind me of till this day.

ABSTRACT

Photosynthetic antenna complexes harvest sunlight and efficiently transport energy to the reaction center where charge separation powers biochemical energy storage. Under low light conditions, the quantum efficiency of light harvesting complexes is almost unity. The high quantum efficiency of photosynthetic antenna complexes has attracted immense theoretical and experimental studies. It is understood that energy transfer is an incoherent process. However, it was hypothesized that the energy transfer can have significant coherent contribution before it becomes completely incoherent in nature. Recent discovery of existence of long-lived quantum coherence during energy transfer has sparked the discussion on the role of quantum coherence on the energy transfer efficiency. Early works assigned observed coherences to electronic states, and theoretical studies showed that electronic coherences could affect energy transfer efficiency by either enhancing or suppressing the transfer. However, the nature of coherences has been fiercely debated as coherences only report the energy gap between the states that generate coherence signals, and this information is insufficient for its unambiguous assignment. Recent works have suggested that either the coherences observed in photosynthetic antenna complexes arise from vibrational wave packets on the ground state or, alternatively, coherences arise from mixed electronic and vibrational states.

The work presented here enumerates various technical, experimental and theoretical advances made over the past few years to understand the nature of coherent energy transfer dynamics in photosynthetic antenna complexes. The experimental and theoretical advances in interpreting 3^{rd} order spectroscopic signals made GRAPES a powerful spectrometer to perform 3^{rd} order non-linear electronic spectroscopy. This spectroscopy provides insight into correlations responsible for energy transfer and long-lived coherence. The ability to further control each light-matter interaction by altering the state of polarization of light has been used to decipher the nature of coherence during energy transfer. The control over polarization of individual light-matter interactions has been used to explore the chiral dynamics of photosynthetic antenna complexes. These experiments suggest that chirality, or handedness,

of light harvesting complexes is not only responsible for differential absorption of left- and right-circularly polarized light, but is also responsible for ensuing exciton dynamics.

CHAPTER 1

PHOTOSYNTHESIS AND ENERGY TRANSFER EFFICIENCY

The industrial revolution has raised standards of living. Ever since, for all these years, fossil fuels have been the main source to satisfy energy needs of industries that keep improving the standard of living. While living standards are non-negotiable, societies' continuing dependence on fossil fuel to maintain its living standards has led to global warming. Limited fossil fuel reserves and global warming have propelled development of clean and renewable sources of energy. Some of these developments include harnessing wind energy and using nuclear energy. Meanwhile harnessing solar energy has presented itself as a serious alternative to fossil fuels. The idea of solar energy harvesting is attractive specially because of naturally occurring photosynthetic organisms. Naturally occurring photosynthetic organisms are great model systems to study and learn nature's design principles from; design principles that have arguably sustained life on earth. A detailed understanding of photosynthetic processes will lead to technologies that will efficiently harvest energy from sun, for example, efficient solar cells.

While all processes that happen in photosynthetic machinery are important and require exhaustive study, my interest lies in a particular process that involves energy transfer that happens immediately after energy is harvested from sunlight. In the following sections I will be providing an overview of processes that are collectively known as photosynthesis, with focus on energy transfer, and why I find it an exciting phenomenon to study.

1.1 Photosynthesis: An overview

When we think about photosynthesis we think about plants that harvest energy from sunlight and produce animal-consumable products such as oxygen and sugar. A lot of chemical and non-chemical processes take place in between absorption of light and production of

animal consumable products. Chemical processes involve making or breaking of chemical bonds, e.g formation of sugar. Non-chemical processes do not involve making or breaking of chemical bonds. Instead, non-chemical processes involve quantum mechanical phenomenon. The events that happen immediately after harvesting energy from sunlight, i.e energy transfer, fall in this category of processes that involve quantum mechanical principles. The kind of systems where these quantum mechanical processes take place are soft materials at relatively high temperatures; not exactly the kind of system we associate quantum mechanical phenomena with.

The entire gambit of processes that are collectively known as photosynthesis can be classified into three major steps,[1;2]

- The first step is harvesting energy from sunlight. Photosynthetic organisms employ a network of light harvesting antenna complexes to harvest energy from sunlight. When compared with a single light harvesting complex, a network of light harvesting complexes greatly increase the amount of light that can be absorbed by the photosynthetic organism. The reason behind this is that sunlight is a relatively dilute source of energy. Within the network of light harvesting complexes, the excited state, in the form of an exciton, moves from one point in space to another before it reaches the reaction center (RC). The motion of exciton to RC is thermodynamically favoured because it is energetically downhill process. The network of light harvesting antennas is designed in such a way that the antenna farthest away from the RC absorbs shorter wavelength photons than does the antenna complex closer to the RC. In the downhill energy transfer process, a small fraction of excion's energy is lost to the environment as heat. Upon receiving the heat energy, the environment rapidly thermalizes making the process practically irreversible. In principle, energy transfer event can be uphill as well. Uphill energy transfer can take place when heat energy is transferred from the environment to the antenna complex instead of from antenna complex to the environment. But the

probability of uphill energy transfer resulting from heat transfer from environment to antenna complex goes down exponentially and such events are extremely rare.

- Once the exciton reaches RC, the energy goes to a special pigment (P) that is similar to a chlorophyll. The environment of P makes excited P a highly reducing agent. Excited P ejects an electron to form P^+. The ejected electron is accepted by a nearby electron acceptor A to form A^-. The electron transfer process results in the formation of P^+A^- ion pair. Formation of the ion pair signifies conversion of exciton energy to chemical redox energy. A series of processes happen that increase the separation between the anion and the cation. This reduces the probability of electron transfer form A^- to proximially close P^+, in which case energy would be lost as heat.

- The electron transport in the RC is coupled to a machinery that creates a proton gradient across the cell membrane. The net result is a photon-driven pH difference across the cell membrane. This electro-chemical pH gradient is used to drive ATP-synthase to synthesize ATP.

The above three steps provide the framework for any photosynthetic machinery. The framework will manifest itself in varying degrees of sophistication dependent on the species.

My interest lies in efficiency of energy transfer which is almost 100%. The 100% quantum efficiency of energy transfer means that once a photon is absorbed and an excited state is created, then no matter how the excited state meanders the antenna complex network, it will reach the RC and initiate the electron transfer process.

1.2 Light harvesting unit of purple bacteria

Purple bacteria are an ideal system to study to understand energy transfer efficiency. It is a special kind of bacteria that lives at the bottom of lakes and ponds. It lives under a couple of inches of sludge and receives very few photons. The efficiency with which these bacteria

use the absorbed photon is crucial for the survival of the species. It has been shown that the efficiency of energy transfer in purple bacteria is nearly 100%.[1;2]

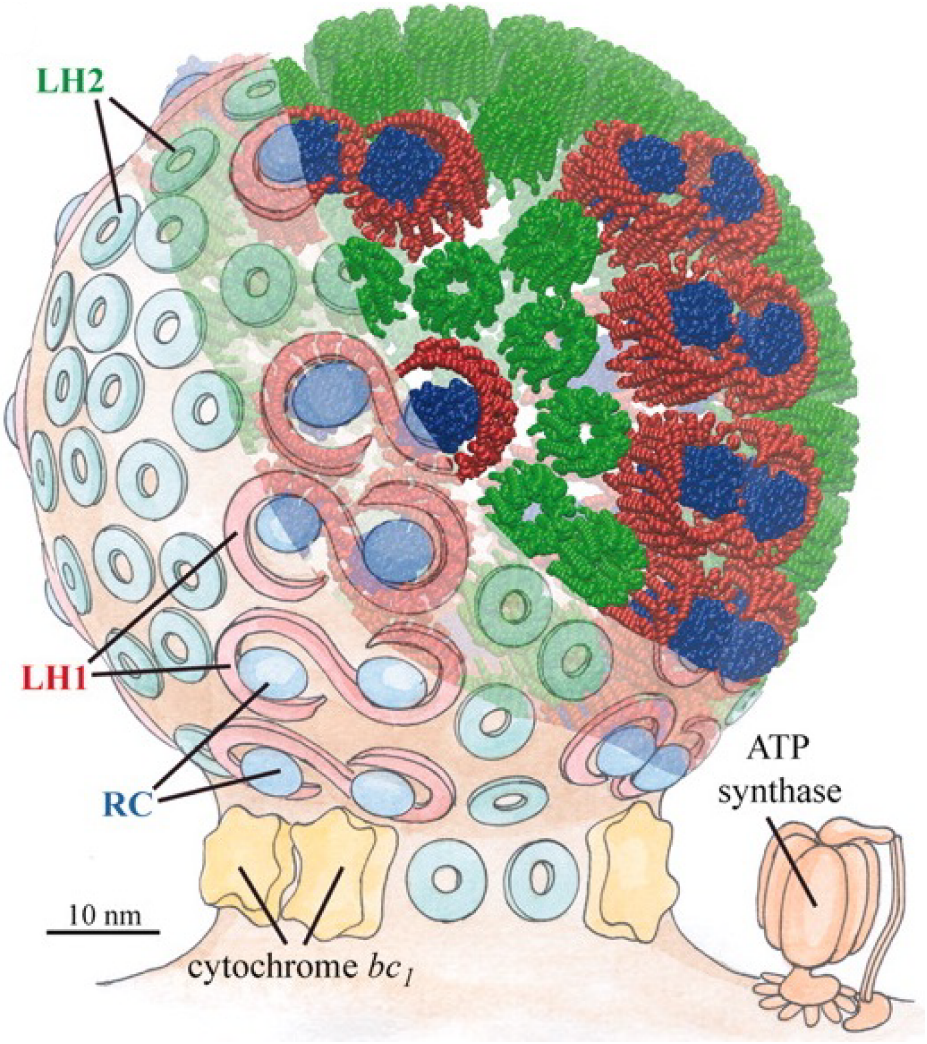

Figure 1.1: Cartoon representation of an invagination in purple bacteria's cell membrane. The invagination contains a network of light harvesting complexes LH2 (green), LH1 (red) and reaction center (blue). Copyright (2007) National Academy of Sciences, U.S.A.

The light harvesting unit purple bacteria is housed in invaginations in cell membrane. Figure 1.1 shows a cartoon representation of one such invaginations.[3] The cartoon shows Light Harvesting complex 2 (LH2)in green, Light Harvesting complex 1 (LH1) in red and reaction center (RC) in blue. When this particular purple bacteria absorbs photon it is most probably absorbed by LH2 just because of its sheer abundance. Upon absorbing a photon, LH2 creates an exciton that is shuttled from one LH2 to another until it reaches LH1. LH1

then transfers it to RC that initiates charge separation. The charge separation is coupled to a machinery that creates proton gradient across the membrane. The cartoon also shows the ATP synthase that use the proton gradient to synthesize ATP.

1.3 Light Harvesting complex 2 (LH2)

1.3.1 Building blocks: Bacteriochlorophyll a

There are different light harvesting antenna complexes that absorb light in different regions of solar spectrum. Despite the difference in overall structures, there is a remarkable similarity in the building blocks of various antenna complexes. The building blocks are either chlorophyll (Chl) or bacteriochlorophyll (BChl).[2] Figure 1.2 shows the structural formula of Bacteriochlorophyll *a* (BChla).[1] The Mg^{2+} in the middle is coordinated to four nitrogen atoms. Only a few species of purple bacteria have been found that contain Zn^{2+} atom instead of Mg^{2+}. This is usually the case when bacteria grow in acidic environments where Mg^{2+} can be easily replaced by H^{+}. Mg^{2+} and Zn^{2+} are the only two cations that have been found in bacteriochlorophylls.[1] In the planar ring, each of the nitrogen atoms is a part of a substructural element of the molecule that is derived from pyrrole. Because there are four such subunits in the molecule, bacteriochlorophyll is also referred to as tetrapyrrole, and so are other chlorophylls and bacteriochlorophylls. Each of the pyrrole rings in the molecule has a name that is irrespective of the type of Chl or BChl. Figure 1.2 shows the name of the rings as determined by the IUPAC nomenclature. An alternative way of addressing the rings is by numbering them, which is the Fischer nomenclature. According to Fischer nomenclature, instead of referring the rings as A-E, the rings are referred to by the Roman numerals I-V.

The spectroscopic properties of BChla involve the conjugated π electrons of the chlorin macrocycle. Figure 1.2 shows the absorption spectrum of BChla. The spectrum can be

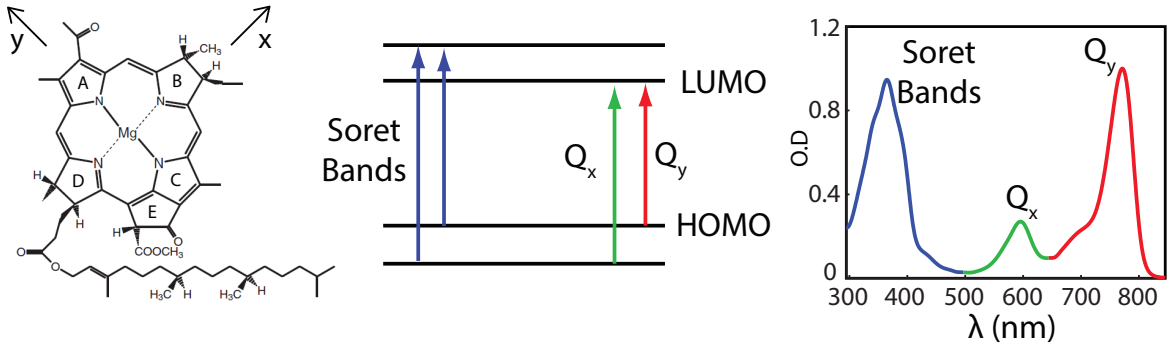

Figure 1.2: Left: A BChla ring with IUPAC name for the rings. The x-axis and the y-axis define the direction for Q_x and Q_y transitions. Centre: The electronic states that are involved in Q_x and Q_y transitions. Right: Absorption spectrum of BChla that shows the peaks corresponding to Q_x, Q_y and Soret transitions.

described using the "four orbital" model that involve $\pi \rightarrow \pi^*$ transitions. The four orbitals that are primarily involved are the two highest occupied molecular orbitals (HOMOs) and the two Lowest Unoccupied Molecular Orbitals (LUMOs). In the absorption spectrum, the two peaks with lowest energies are called Q bands, and the higher energy bands are called B bands or just Soret bands. The distinction between Q and Soret bands is that in Q bands the final state of the system is LUMO and in Soret bands the final state of the system is LUMO+1. There are two Q bands. The Q band at longer wavelength, 770 nm, is called Q_y and corresponds to the transition from HOMO to LUMO. The Q band at shorter wavelength, 595 nm, is called Q_x and corresponds to transition from HOMO-1 to LUMO. Not only Q_y and Q_x absorb at different wavelengths, they also have different dipole strengths with different orientations. The Q_y and Q_x are polarized in almost perpendicular direction. Q_y point form N-atom of C ring to N-atom of A ring. Q_x points from N-atom of D ring to N-atom of B ring. When many BChlas are packed in a protein scaffold, the BChla's give rise to several excited states that can be understood in terms of Q_y and Q_x transitions. We will look at LH2 and understand how the packing of BChlas affect the electronic structure of LH2.

1.3.2 Physical and electronic structure of LH2

LH2 is a circular pigment protein complex with two rings.[4–6] The pigments that make up LH2 are BChlas. The pigments are embedded in a scaffold of eighteen α apoprotein helices. Figure 1.3 shows the structure of LH2 with the protein scaffold (on the left) and without the scaffold (on the right). The inner apoproteins are called α-apoprotein helices, and there are nine of them. The outer apoproteins are called β-apoprotein helices, and there are nine of them as well. The BChlas of the lower ring are strongly covalently bonded to the apoproteins while those of the upper ring are bonded weakly; this alters the absorption spectrum of individual BChlas.

The physical structure of the LH2 plays a crucial role in determining its electronic structure. An important factor in determining the electronic structure and its eigenstates is the separation between the BChlas. The BChlas of the upper ring are separated by about 21 Å which results in weak Coulombic coupling between them. As a result the BChlas mix weakly and the absorption peaks of the upper ring are similar to absorption peaks of the nine individual BChla molecules. The separation between the BChlas of the lower ring is on an average 9 Å. The close proximity of the BChlas of the lower ring results in strong mixing of the electronic states of the individual BChlas. The strong mixing gives rise to eigenstates of lower ring that are significantly different from the eigenstates of the individual BChlas. As a result the absorption peaks of the lower ring appear at significantly different positions compared to those of individual BChlas.

For most spectroscopic studies, it suffices to understand the electronic structure of LH2 in terms of Q_y transition of individual BChlas. For the upper ring, the Q_y states of the nine BChlas mix weakly and give rise to nine states that absorb at 800 nm as shown in figure 1.4. For the lower ring, the strong mixing between the Q_y states of the eighteen BChlas give rise to eighteen excited states. However, only a few of those are bright and absorb at 850 nm. Based on where the rings absorb, the upper ring is called B800 because it absorbs at

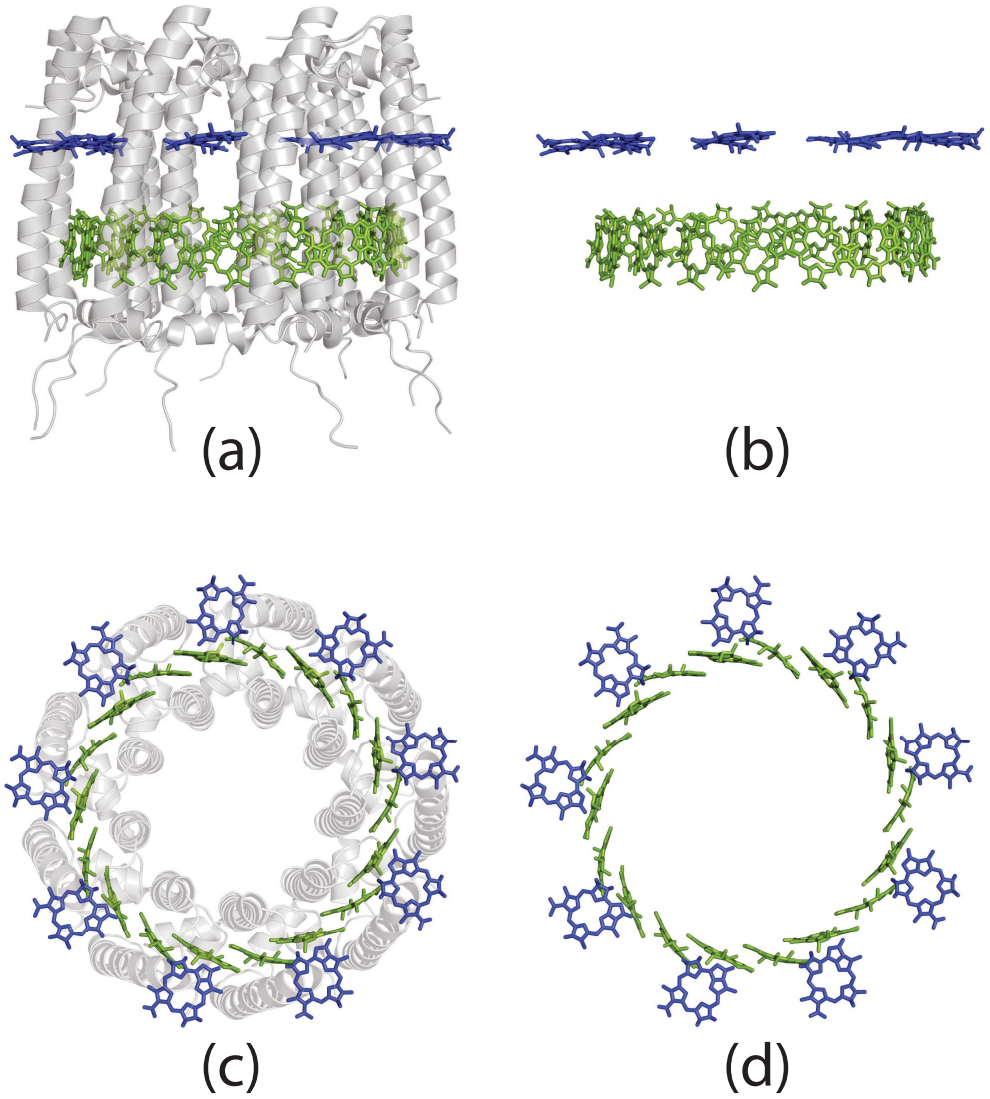

Figure 1.3: Physical structure of LH2 with B800 ring in blue, B850 in green and the protein scaffold in silver. (a) and (b) give the membrane view of LH2 with and without the protein scaffold, respectively. (c) and (d) give the cytoplasmic view of LH2 with and without the protein scaffold, respectively. Drawn using PDB file 2FKW

800 nm, and the lower ring is called B850 because it absorbs at 850 nm.

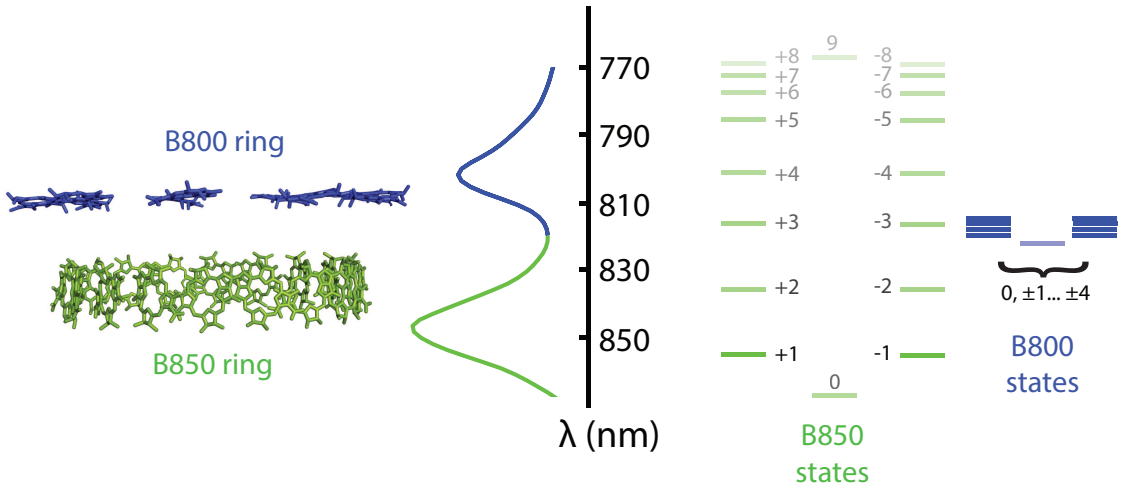

Figure 1.4: The absorption spectrum of LH2 has two peaks shown in blue and red, that correspond to B800 and B850 rings, respectively. The exciton states on B850 ring are labeled $0, \pm 1, \pm 2, ..., \pm 8, 9$. However, most of the dipole strength lies in the ± 1 states that absorb around 850 nm. The exciton states on B800 ring are labeled $0, \pm 1, ..., \pm 4$. The dipole strength of B800 band is almost equally shared by $k = \pm 1, ..., \pm 4$ states, and a small fraction by $k = 0$ state, all of which absorb around 800 nm.

The circular structure of LH2 imparts a special property to the excited states of LH2. Because of the circular structure the electronic states acquire clockwise and anticlockwise angular momentum as deduced from a simple quantum mechanical model of a particle on a ring. The clockwise and anticlockwise sense is allocated with cytoplasm as the reference (figure 1.3c,d). Each excited state is assigned a quantum number, k, that represents the state of angular momentum. For B800 ring, the nine states have quantum numbers $k = 0, \pm 1, ..., \pm 4$. The eighteen states of B850 ring are assigned quantum numbers $k = 0, \pm 1, ..., \pm 8, 9$. The state $k = 0$ does not have any angular momentum. The states $k = +1$ and $k = -1$ have opposite angular momenta. As a convention we refer to states with +ve quantum number as having clockwise angular momentum and states with -ve quantum number as having anticlockwise angular momentum. States with same absolute numerical value are degenerate in a perfectly circular complex. Hence, states with $k = +1$ and $k = -1$ have same energy but opposite angular momentum.

1.4 Energy transfer mechanisms

It is incumbent to first look at energy transfer mechanisms before we start considering mechanisms that make energy transfer efficient. There are two common mechanisms of energy transfer in light harvesting complexes. These mechanisms are Förster Resonance Energy Transfer (FRET) mechanism and Redfield mechanism. Any mechanism, be it FRET or Redfield, involves a few key components and principles.[7;8] These are:

1. Donor and acceptor of energy
2. The coupling between the donor and the acceptor, that forms the conduit for energy
3. Energy conservation

The above principles are succinct captured in the Fermi's golden rule that is described by the equation 1.1

$$k = \frac{2\pi}{\hbar}|V_{kl}|^2\delta(E_k - E_l) \tag{1.1}$$

where k and l are the donor and acceptor states, V_{kl} is the coupling between the donor and the acceptor, and the Dirac delta function $\delta(E_k - E_l)$ ensures energy conservation as it gets transferred from state k to state l. The physical conditions in which Fermi's golden rule is applied to the system under study is different for FRET and Redfield mechanism. To understand this difference consider figure 1.5 The transition dipoles of the individual bacteriochlorophylls are shown in green and are defined by vectors $\vec{r}_1$ and $\vec{r}_2$. The center to center separation between the two transition dipoles is defined by the vector $\vec{R}$. The entire system can be described by the Hamiltonian given in the following equation[9]

$$H = \epsilon_1 + \epsilon_2 + V_{12} + V_{21} + H^{e-p} \tag{1.2}$$

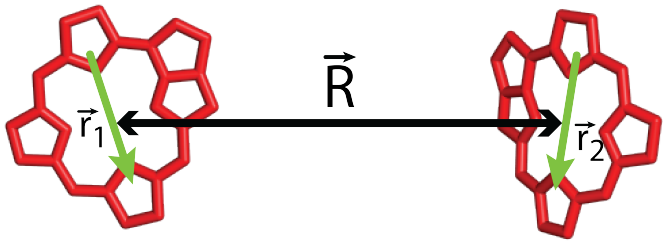

Figure 1.5: A simple configuration of bacteriochlorophylls (red). The transition dipole of the respective bacteriochlorophylls is shown in green. The vector that define center-to-center separation between the transition dipoles is $\vec{R}$.

where ϵ_1 and ϵ_2 are the site energies of the two chromophores, V_{12} and V_{21} are the Coulombic coupling between the two chromophores and H^{e-p} is the electron-phonon coupling between the electronic state of the chromophores and its environment. The site energies are at optical frequencies in the range 12000 cm^{-1} - 18000 cm^{-1}, whereas the Coulombic and electron-phonon couplings are usually in the 10 cm^{-1} - 500 cm^{-1} range. While the electronic transitions define the states between which energy transfer takes place, the relative strength of Coulombic and electron-phonon coupling dictates whether the the mechanism of energy transfer is Förster Resonance Energy Transfer or the Redfield Energy Transfer. We will now look at each of them to understand the difference between the two.

1.4.1 Förster Resonance Energy Transfer

Förster Resonance Energy Transfer applies when Coulombic coupling V_{12} between the donor and the acceptor is smaller than the electron-phonon coupling H^{e-p}.[10;11] This usually is the case when the separation between the chromophores is large compared to the length of the transition dipoles, i.e. $|\vec{R}| \gg |\vec{r_1}|$ and $|\vec{R}| \gg |\vec{r_2}|$. Under such circumstances the Coulombic coupling between the two chromophores is approximated by the dipole-dipole interaction and is given by

$$V = \frac{|\vec{\mu}_1||\vec{\mu}_1|}{4\pi\varepsilon_\circ|\vec{R}|^3}(3\cos\theta_1\cos\theta_2 - \cos\theta_{12}) \tag{1.3}$$

where $|\vec{\mu}_1|$ and $|\vec{\mu}_2|$ are the transition-dipole strengths of the two chromophores, $\vec{R}$ is the vector that defines the center-to-center separation between the two chromophores, θ_1 and θ_2 are the angles that the transition dipoles make with respect to the vector $\vec{R}$, and θ_{12} is the angle between the transition dipoles of the individual chromophores. The application of Fermi's golden rule for energy transfer from one chromophore to another gives

$$k_{1\to 2} = \frac{4\pi}{3\hbar}\frac{|\vec{\mu_1}|^2|\vec{\mu_2}|^2}{|\vec{R}|^6}J_{12} \tag{1.4}$$

where $k_{1\to 2}$ is the rate of non-radiative energy transfer from chromophore 1 to chromophore 2, and J_{12} is the overlap between the emission spectrum of chromophore 1 and the absorption spectrum of chromophore 2. The overlap factor ensures energy conservation and dependence on $|\vec{\mu_1}|$, $|\vec{\mu_2}|$ and $|R|$ comes from Coulombic interaction between the two dipoles. Figure 1.6 is a schematic representation of FRET mechanism.

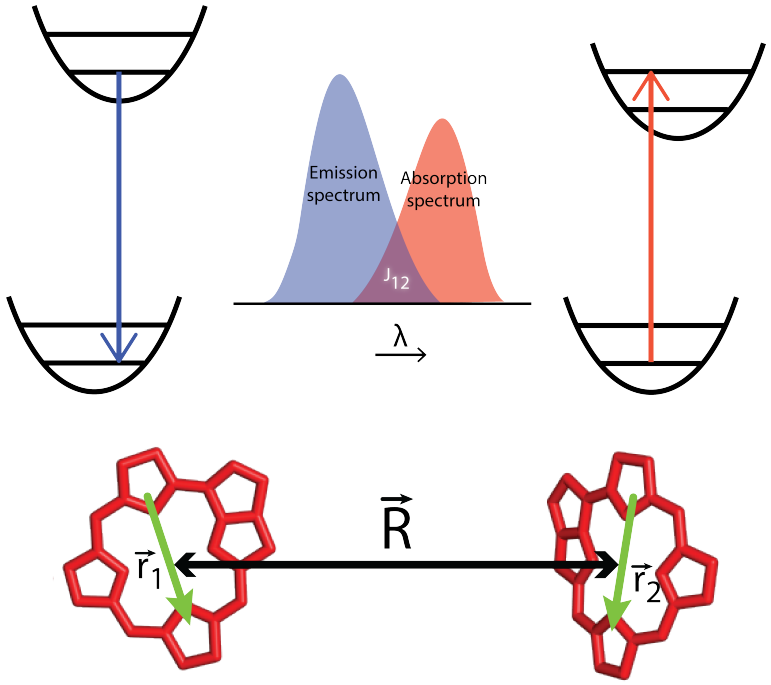

Figure 1.6: The two electronic states of the chromophore 1 and chromophore 2, that act as donor and acceptor of energy in FRET mechanism of energy transfer. J_{12} is the overlap between the absorption and emission of chromophore 1 and 2, respectively.

1.4.2 Redfield mechanism of energy transfer

Redfield mechanism of energy transfer operates when the Coulombic coupling is much stronger than the electron-phonon coupling in equation 1.2.[12–16] This is usually the case when chromophores are closely packed and $|\vec{R}| \sim |\vec{r}_1|,|\vec{r}_2|$. Under such conditions the electronic states ϵ_1 and ϵ_2 of the two chromophores mix under the influence of Coulombic coupling V to give rise to new delocalized states, E_1 and E_2 as shown in figure 1.7. Mathematically, this can be expressed as

$$\begin{bmatrix} \epsilon_1 & V \\ V & \epsilon_1 \end{bmatrix} \xrightarrow{diagonalization} \begin{bmatrix} E_1 & 0 \\ 0 & E_2 \end{bmatrix} \tag{1.5}$$

The energy of the electronic states depends on the position of the nuclei. The dependence

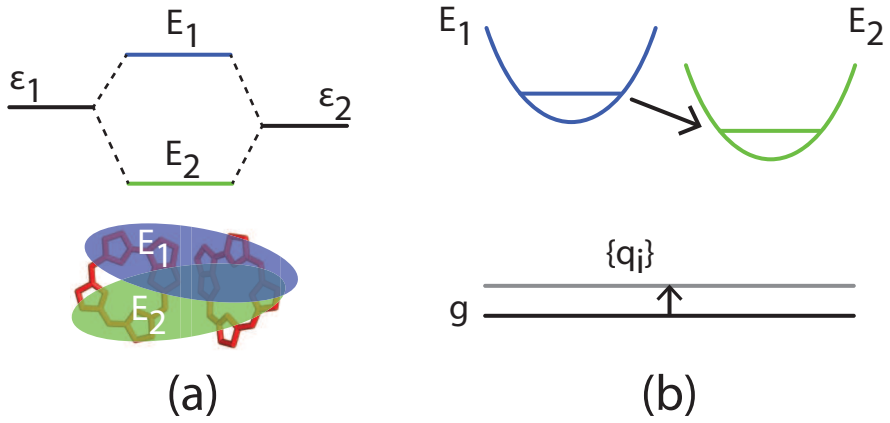

Figure 1.7: (a) The two electronic states ϵ_1 and ϵ_2 mix because of the strong Coulombic coupling between chromophore 1 and chromophore 2. The mixing gives rise to two delocalized electronic states E_1 and E_2.

comes through the Born-Oppenheimer approximation. According to Born-Oppenheimer approximation, the nuclei are heavy compared to the electrons and can be considered stationary while the electrons move around them. Consequently, change in the position of the nuclei results in change in energy of the nuclei. Since the electronic states E_1 and E_2 are delocalized, there will some nuclear modes that will affect both the electronic states E_1 and E_2. This dependence of E_1 and E_2 on such nuclear modes gives rise to coupling between the two

states and is responsible for energy transfer between them. Applying Fermi's golden rule for transition from E_1 to E_2 gives

$$k_{1\to 2} = (p.r) \cdot 2Re\left(\int_0^{+\infty} dtC(t)exp(-i\omega_{12}t)\right) \tag{1.6}$$

where $(p.r)$ tells about the spatial overlap between the states E_1 and E_2, $C(t)$ is the system-bath coupling.

1.5 References

[1] Blankenship, R. *Molecular Mechanisms of Photosynthesis*; Blackwell Science: Oxford, 2002.

[2] van Amerongen, H., Valkunas, L., and van Grondelle, R. *Photosynthetic Excitons*; World Scientific: Singapore, 2000.

[3] Sener, M. K., Olsen, J. D., Hunter, C. N., and Schulten, K. (2007) Atomic-level structural and functional model of a bacterial photosynthetic membrane vesicle. *Proceedings of the National Academy of Sciences 104*, 15723–15728.

[4] McDermott, G., Prince, S. M., Freer, A. A., Hawthornthwaite-Lawless, A. M., Papiz, M. Z., Cogdell, R. J., and Isaacs, N. W. (1995) Crystal structure of an integral membrane light-harvesting complex from photosynthetic bacteria. *Nature 374*, 517–521, 10.1038/374517a0.

[5] Cogdell, R. J., Gall, A., and Kohler, J. (2006) The architecture and function of the light-harvesting apparatus of purple bacteria: from single molecules to in vivo membranes. *Quarterly Reviews of Biophysics 39*, 227–324.

[6] *PDB file 2FKW for crystal structure of LH2*

[7] Mukamel, S. *Principles of Nonlinear Optical Spectroscopy*; Oxford University Press: New York, 1995.

[8] Kuhn, O., Renger, T., and May, V. (1996) Theory of exciton-vibrational dynamics in molecular dimers. *Chemical Physics 204*, 99–114, Ua824 Times Cited:36 Cited References Count:43.

[9] Cho, M., Vaswani, H. M., Brixner, T., Stenger, J., and Fleming, G. R. (2005) Exciton Analysis in 2D Electronic Spectroscopy. *The Journal of Physical Chemistry B 109*, 10542–10556.

[10] Förster, T. (1948) Zwischenmolekulare Energiewanderung und Fluoreszenz. *Annalen der Physik 2*, 55–75.

[11] Knox, R. S. (2012) Frsters resonance excitation transfer theory: not just a formula. *Journal of Biomedical Optics 17*, 011003–1–011003–6.

[12] Redfield, A. G. (1957) On the Theory of Relaxation Processes. *IBM Journal of Research and Development 1*, 19–31.

[13] Zhang, W. M., Meier, T., Chernyak, V., and Mukamel, S. (1998) Exciton-migration and three-pulse femtosecond optical spectroscopies of photosynthetic antenna complexes. *Journal of Chemical Physics 108*, 7763–7774, Zl319 Times Cited:238 Cited References Count:43.

[14] Chen, X., and Silbey, R. J. (2010) Effect of correlation of local fluctuations on exciton coherence. *The Journal of Chemical Physics 132*.

[15] Cho, M. *Two-Dimensional Optical Spectroscopy*; Taylor & Francis, 2010.

[16] Yang, M., and Fleming, G. R. (2002) Influence of phonons on exciton transfer dynamics: comparison of the Redfield, Forster, and modified Redfield equations (vol 275, pg 355, 2002). *Chemical Physics 282*, 161–+, 580YA Times Cited:7 Cited References Count:46.

CHAPTER 2

LINEAR AND NON-LINEAR SPECTROSCOPY

Molecules are in a constant state of fluctuation. However, linear absorption spectrum such as the one in figure 2.1 does not convey such dynamic information. Even though linear spectrum such NMR, IR and UV/Vis spectrum give information about nuclear magnetic coupling, vibrational states and electronic states, respectively, this information is an average over an ensemble of molecules.

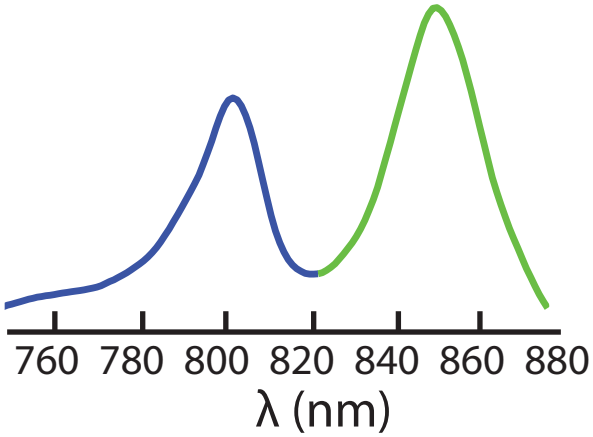

Figure 2.1: Linear absorption spectrum of a system that shows two absorption peaks - one that is centered at 800 nm and the other that is centered at 850 nm. Even though molecules are always in a dynamic state, a liner spectrum such as this fails to provide any dynamics information.

Measuring linear absorption spectrum, such as in figure 2.1, requires systematically changing one parameter. This parameter could be frequency of incident light as in a frequency domain measurement of linear spectrum. Or, it could be timing between two ultrafast pulses in an time domain measurement of linear absorption spectrum. Measuring dynamic properties such as structural changes and energy transfer requires combining multiple parameters. For example, measuring energy transfer requires measuring excitation and emission frequency, and a time domain to measure energy transfer dynamics. Two dimensional (2D) electronic spectroscopy (ES) is one such spectroscopy that combines these parameters and

gives information about dynamics of excited states.[1–5] The result of 2D ES is presented in the form of a 2D map and a collection of such 2D maps provides information that is inaccessible through 1D spectrum as I discuss in the following sections.

2.1 2D Spectrum of a two state system

Consider a simple case of a two state system with a ground state g and excited state e, as in figure 2.2. For laser dye IR144 and given the light source centered at 800nm with 30nm FWHM, the linear absorption spectrum is effectively centered at 800 nm as shown in red. The linear absorption spectrum shows the absorption frequencies. The two dimensional spectrum shows both the absorption frequency and the emission frequency.[6;7] Linear absorption spectrum can be measured in the frequency domain by scanning colors and observing the absorption of each color. The 2D ES can me measure in the time as well as in the frequency domain. While the experiments are performed in the time domain, the plot is easily understood when interpreted in the frequency domain. The molecular system is pumped with laser of resonant frequency, and the corresponding wavelength is plotted on the x-axis as λ_τ in nanometers (nm). When the molecular system comes in resonance with the pump frequency, a certain fraction of molecules transition from the ground state g to the excited state e. After pump pulse dynamics of excited state ensues during the waiting time T after which the system is probed by scanning the colors of the probe pulse.

The probe pulse can bring about two transitions. First, it can result in stimulated emission from the excited state to the ground state. The stimulated emission is 'extra' light field and as a convention is assigned positive sign, as indicated by the colormap. The probe pulse can also be absorbed to transition the system to an excited state. The absorption of probe pulse is assigned negative signal. Given the current bandwidth, the molecular system does not show excited state absorption, and hence a negative signal. Another possibility is absorption of probe beam by the molecules in the ground state. After the pump beam shines

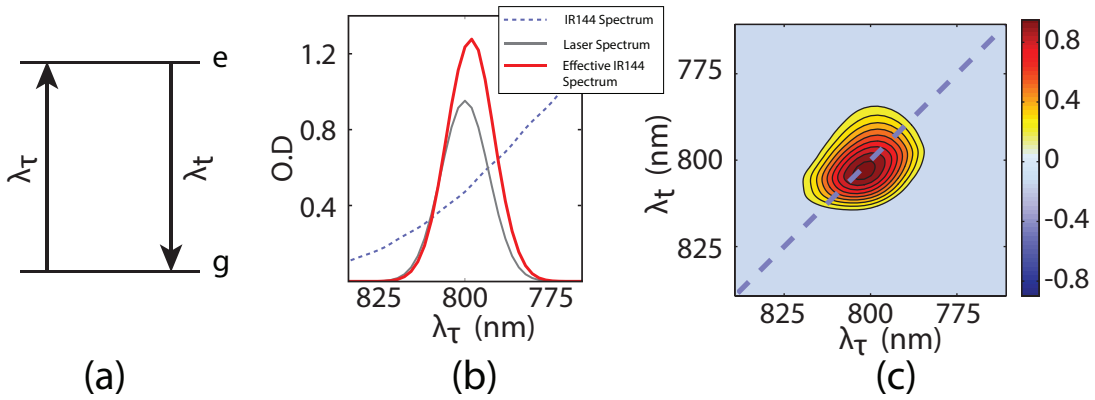

Figure 2.2: (a): A schematic of a simple two state system with ground state g and excited state e. (b): The effective linear absorption spectrum of IR144 given the bandwith of the laser pulse. (c): 2D spectrum of IR144 for T=0 f.s.

onto the sample there are lesser molecules in the ground state. Hence, when the probe beam gets absorbed lesser than it would if there was no pump beam. The lesser absorption of the probe beam by the ground state is known as ground state bleach signal and is positive signal. Both stimulated emission and ground state bleach occur at the same frequency as the absorption frequency in absence of dynamics, and hence are on the diagonal.

2.2 2D spectrum of a three state system

Building on the principles from the last section we can now consider the 2D ES spectrum of a multistate system.[7] The simplest multistate system is a three state system - a ground state g and two singly excited states e_1 and e_2. The molecular system further has doubly excited state f. State e_1 absorbs around 840 nm and e_2 absorbs around 780 nm. The excited state f is located such that e_1 and f are approximately 830 nm apart. We scan the pump beam from 750 nm to 860 nm.

When the light comes in resonance with the state centered at 780 nm we observe the stimulated emission and ground state bleach, and the resulting positive signal is situated on the diagonal corresponding to [λ_τ=780 nm, λ_t=780nm]. As the pump frequency is scanned and the pump pulse comes in resonance with e_1, we see a positive feature on the diago-

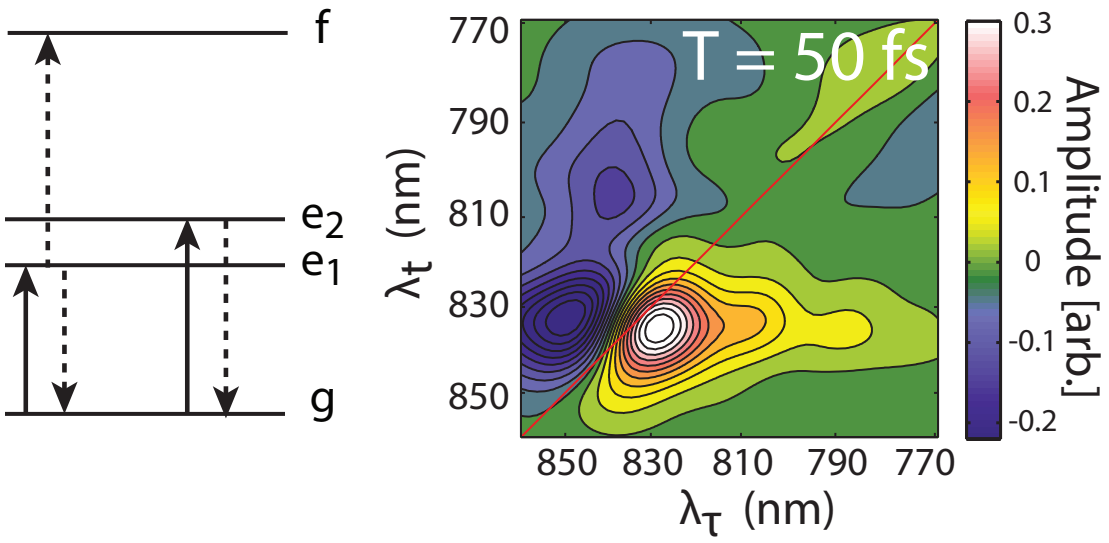

Figure 2.3: Left: Homogeneously broadened linear absorption spectrum where all the members of the ensemble absorb at the same wavelength. Right: In-homogeneously broadened linear absorption spectrum where different members of the ensemble absorb at different wavelengths.

nal coming form stimulated emission and ground state bleach of state e_1. In addition to the stimulated emission and ground state bleach, we also see the negative signal from the absorption of the pump beam to transition the state from e_1 to f.

In addition to the diagonal peaks, we also see off diagonal features. For example, consider the off-diagonal feature at [λ_τ=780 nm, λ_t=830nm]. The off-diagonal feature appears between two diagonal peaks because of the coupling between the states. The off-diagonal feature can be interpreted as following. The molecular system is pumped at λ_τ = 780 nm and then re-emits upon probing at λ_t=830 nm. The observation of a molecule absorbing in one state and re-emit from a different state is attributed to coupling between the two states. The molecular system is excited at λ_τ = 780 nm but because of coupling between e_2 and e_1, the system ends up in state e_1 and hence is an off-diagonal peak.

2.3 Advantages of 2D Electronic spectroscopy

Linear spectroscopy gives information about the states that absorb and the energy they absorb at. Third-order nonlinear spectroscopy gives the same information as well. For example, in figures 2.2 and 2.3 above, the diagonal feature corresponds to the peaks in the linear absorption spectrum. However, third-order spectroscopy provides information that is inaccessible by linear spectroscopy. In the following section we will briefly discuss some of the advantages of third-order spectroscopy over linear spectroscopy.

2.3.1 Distinguishing between homogeneous and inhomogeneous broadening

Consider a simple case of measurement of linear absorption spectrum of an ensemble of molecules that are in an identical microscopic environment and absorb at identical frequency. The linear absorption spectrum of such an ensemble will have a finite width which is called the homogeneous width. However, far from this ideal scenario the molecules in an ensemble have slightly different microenvironment and, hence, each member of the ensemble will absorb at different frequency as shown in figure 2.4. The linear absorption spectrum will still look the same, however, it would be difficult to deduce if peak is homogeneously broadened or inhomogenously broadened. However, 2D ES can help us distinguish between the two scenario. Consider figure 2.5. The anti-diagonal peak width corresponds to the homogeneous width of the different members of the ensemble. The projection of the peak on λ_τ corresponds to the inhomogeneous width of the members of the ensemble. The various members of the ensemble are in a constant state of fluctuation. A change in the microscopic environment of a member results in a change in resonance frequency. The change in the resonance frequency with time, due to fluctuations in the environment, is known as spectral diffusion.

2D spectrum maps out the time scale of spectral diffusion. Because of spectral diffusion, a member of the ensemble will absorb and emit at different frequencies, that results in rounded peaks. Consider figure 2.5. At $T = 0$ fs, the diagonal peak is elongated due to

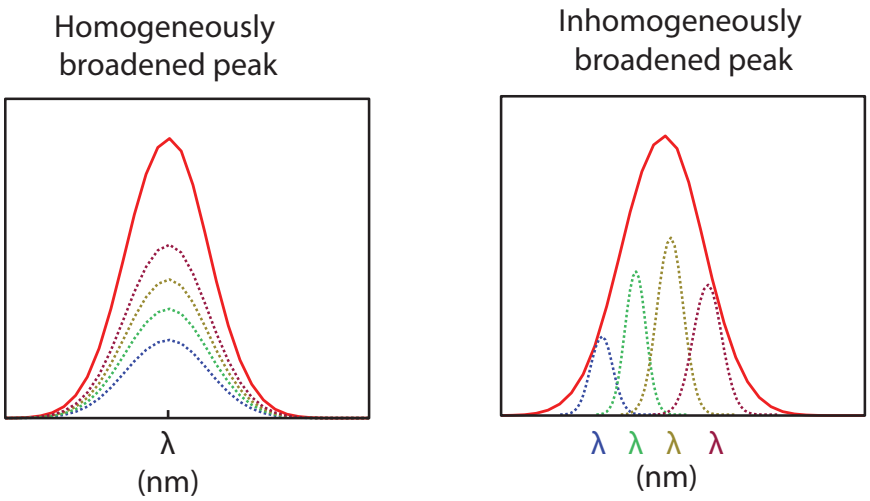

Figure 2.4: Left: Homogeneously broadened linear absorption spectrum where all the members of the ensemble absorb at the same wavelength. Right: In-homogeneously broadened linear absorption spectrum where different members of the ensemble absorb at different wavelengths.

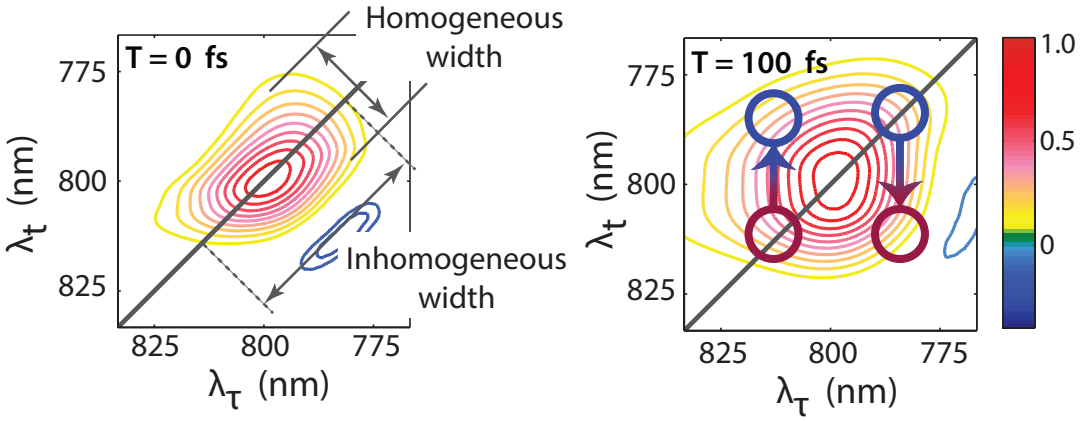

Figure 2.5: Left: Homogeneous width is the anti-diagonal width of the diagonal peak. Inhomogeneous width is the diagonal width of the peak. Right: Spectral diffusion results in a rounded peak. Due to spectral diffusion the members of the ensemble that absorb on the blue side of the spectrum, re-emit at the redder side of the spectrum hence broadening the peak on the lower side. The molecules that were pumped at the redder side of the spectrum re-emit on the bluer side of the spectrum hence broaden the peak on the upper side of the peak.

inhomogeneous distribution of molecules. Let us focus on a small subset of members of the ensemble at absorb at $\lambda_\tau = 815$ nm. The $T = 0$ fs 2D map shows that these members of the ensemble absorb at $\lambda_\tau = 815$ nm and emit at the same. The $T = 100$ fs 2D map shows that the members of the ensemble that absorbed at $\lambda_\tau = 815$ nm (shown in red circle) emit at $\lambda_\tau = 780$ nm (shown in blue circle). This difference in absorption and emission frequency results from spectral diffusion, and the 2D map provides the time scale of this process; in this case the time scale is 100 fs.

2.3.2 Observing Excited state dynamics

2D spectrum shows coupling between the excited states, and helps to monitor the dynamics of excited states.[7;8] The figure below shows how 2D ES helps measure the dynamics of excited states.

Figure 2.6(a) is a schematic of the energy level diagram of Light Harvesting Complex 2 (LH2). The state B800 absorbs at 800 nm and the B850 state absorbs at 850 nm. LH2 is pumped at both the resonant frequencies as shown by the upward pointing blue and green arrows. The system is let to evolve for certain amount of waiting time, T, where the system relaxes form B800 to B850 as shown by the red arrow. The system is then probed that results in stimulated emission from each of the states. We also see ground state bleach from each of the states. Both stimulated emission and ground state bleach signals show up on the diagonal. Figure 2.6(b) shows the 2D map for $T = 0$ fs. Figure 2.6(c) is a stack of 2D maps for various waiting times. In order to extract the dynamics we observe the evolution of the diagonal peak at 800 nm. The diagonal peak at 800 nm has two contributions - stimulated emission from B800 state and the ground state bleach signal. While the ground state bleach signal is constant, the stimulated emission from B800 varies because part of excitation from B800 lands in B850 state. The rate at which the stimulated emission dies out is also the rate at which excitation transfers form B800 to B850. By fitting the experimentally obtained curve we can estimate the rate of excitation transfer. The trace in figure 2.6(d) was fitted

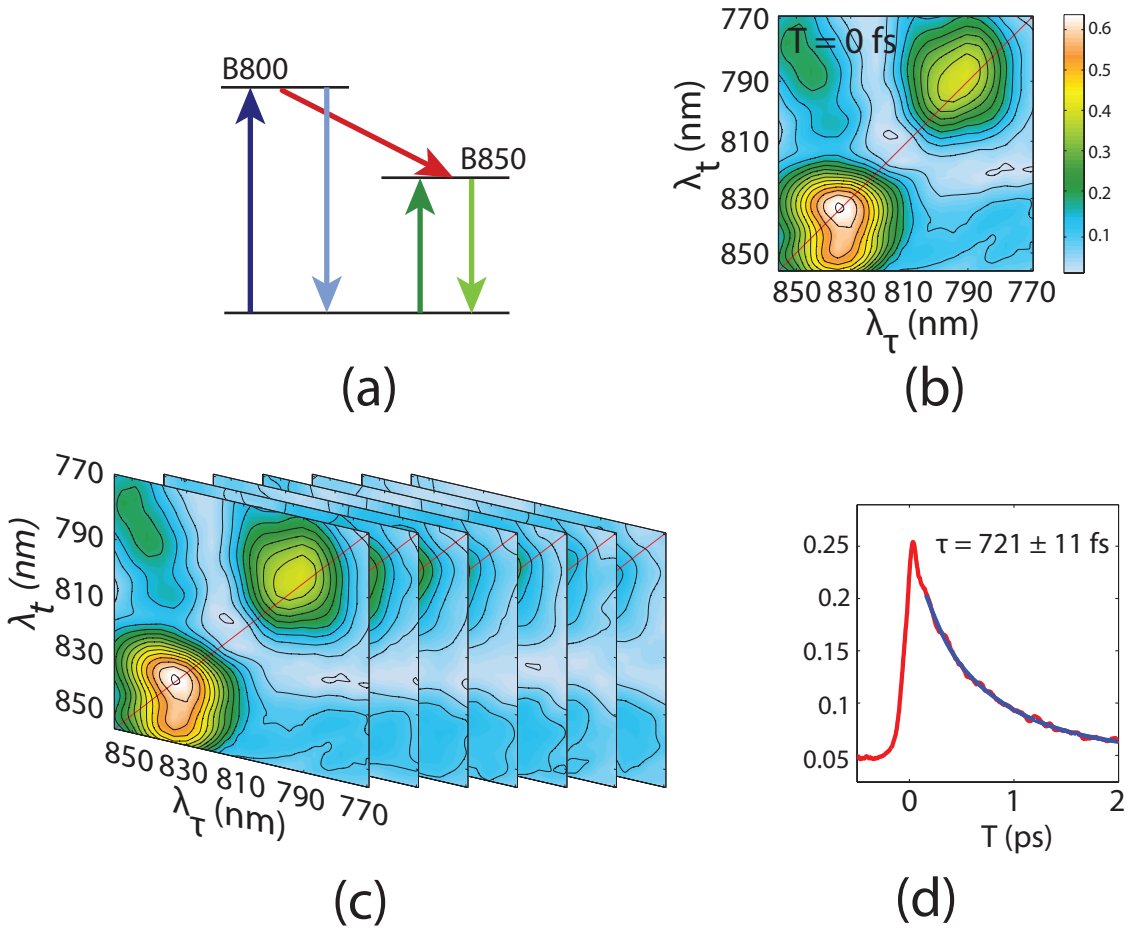

Figure 2.6: (a): A schematic energy level diagram of Light Harvesting Complex 2 (LH2). B800 is the state that absorbs at 800 nm and B850 absorbs at 850 nm. (b): 2D ES map for $T = 0$ fs. (c): A stack of 2D maps for different waiting times. (d): The trace of the peak at [$\lambda_\tau = 800$ nm, $\lambda_t = 800$ nm] for different waiting times. Red trace is experimental data and the blue trace is fit to the trace.

to a monoexponential function and the fit gave a life time of $\tau = 721 \pm 11$ fs for the excited state. Sometime, a highly delocalized electronic state's synamics might not be appropriately modeled as a monoexponential function. This is because before energy transfer takes place, the delocalized state localizes that gives rise to a trace that decays as a gaussian function at short times. In such cases, the experimental trace has to be fitted to a gaussian and an exponential function.

2.4 References

[1] Zanni, M. T., Ge, N. H., Kim, Y. S., and Hochstrasser, R. M. (2001) Two-dimensional IR spectroscopy can be designed to eliminate the diagonal peaks and expose only the crosspeaks needed for structure determination. *Proceedings of the National Academy of Sciences of the United States of America 98*, 11265–11270.

[2] Hybl, J. D., Albrecht, A. W., Faeder, S. M. G., and Jonas, D. M. (1998) Two-Dimensional Electronic Spectroscopy. *Chemical Physics Letters 297*, 307–313.

[3] Hybl, J. D., Ferro, A. A., and Jonas, D. M. (2001) Two-dimensional Fourier transform electronic spectroscopy. *The Journal of Chemical Physics 115*, 6606–6622.

[4] Cowan, M. L., Ogilvie, J. P., and Miller, R. J. D. (2004) Two-dimensional spectroscopy using diffractive optics based phased-locked photon echoes. *Chemical Physics Letters 386*, 184–189.

[5] Brixner, T., Mancal, T., Stiopkin, I. V., and Fleming, G. R. (2004) Phase-stabilized two-dimensional electronic spectroscopy. *The Journal of Chemical Physics 121*, 4221–4236.

[6] Jonas, D. M. (2003) TWO-DIMENSIONAL FEMTOSECOND SPECTROSCOPY. *Annual Review of Physical Chemistry 54*, 425–463.

[7] Hamm, P., and Zanni, M. *Concepts and Methods of 2D Infrared Spectroscopy*; Cambridge University Press, 2011.

[8] Brixner, T., Stenger, J., Vaswani, H. M., Cho, M., Blankenship, R. E., and Fleming, G. R. (2005) Two-dimensional spectroscopy of electronic couplings in photosynthesis. *Nature 434*, 625–628.

CHAPTER 3

FORMALISM OF SPECTROSCOPY

In the last chapter I described interpretation of a 2D spectrum. 2D ES experiments can be described in both the time domain and the frequency domain,[1] however the experiments are almost exclusively performed in the time domain. Time domain experiments require the use of ultrafast laser pulse. Performing non-linear spectroscopy to probe the molecular properties requires understanding basic quantum mechanics, nature of light-matter interaction and basic electromagnetic theory. To develop a concrete understanding and description of non-linear spectroscopic signals we need to get into the idea of density matrix, response functions and double sided Feynman diagrams. All of this will be covered in the context of time domain experiments. I will convey the basic concepts by applying it to linear spectroscopy and then move on to non-linear spectroscopy.

3.1 Ultrafast pulses, eigenstates and emitted field

Commercially available UV/Vis or IR spectrometers measure linear absorption spectrum by shining different colors at the sample at different times and recording the absorption of each color to give the absorption spectrum of the molecular system. In ultrafast pulses, all colors are put together and maintain a fixed phase relationship with respect to each other. Ideally if the ultrafast pulses are transform limited, the different colors interfere constructively for only a few femtoseconds for 2DES experiments (and few pico-seconds for 2DIR experiments). In 2D-ES experiments ultrafast pulses can be anywhere between 5 fs to 50 fs.

In semiclassical theoretical treatment of ultrafast spectroscopy, ultrafast pulses are usually modeled as monochromatic light of frequency ω_o with a femtosecond time scale pulse envelope.[1–4] The pulse is interpreted as femtosecond pulse with ω_o center frequency. Figure 3.1(b) shows the monochromatic light with a pulse envelope and the corresponding Fourier

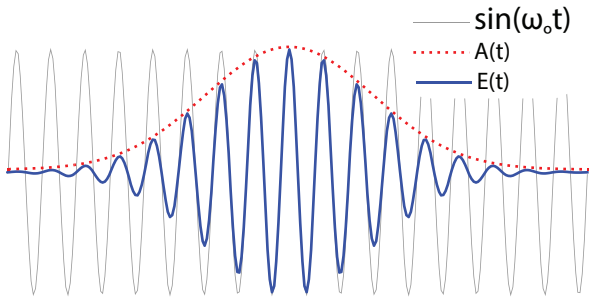

Figure 3.1: A femtosecond pulse (blue) can be modeling as a monochromatic ligh (black)t with a femtosecond time scale pulse envelope (dotted red).

transform. The ultrafast pulse can be modeled using equation 3.1

$$\vec{E}(t) = A(t)\sin(\vec{k}\cdot\vec{r} - \omega_o t + \phi)\hat{e} \tag{3.1}$$

where $A(t)$ is the pulse envelope, $\vec{k}$ is wave vector, $\vec{r}$ is position vector, ω_o is the center frequency, t is time, ϕ is phase under the envelope and $\hat{e}$ contains the information about the state of polarization of the electric field associated with the pulse. If the pulse is linearly polarized, $\hat{e}$ is the unit vector pointing in the direction of polarization of electric field. The interaction of electric field with matter is semiclassically described as

$$\hat{V}(t) = -\hat{\mu}\cdot\vec{E}(t) \tag{3.2}$$

where $\hat{V}$ is the interaction Hamiltonian, $\hat{\mu}$ is the dipole operator and $\vec{E}(t)$ is the time-dependent electric field. Therefore the Hamiltonian that describes the dynamics of the system under the influence of the electric field is given by the Hamiltonian $\hat{H}(t)$

$$\hat{H}(t) = \hat{H}_o + \hat{V}(t) \tag{3.3}$$

where $\hat{H}_o$ is the system Hamiltonian without the field. The eigenstates $|n\rangle$ of $\hat{H}_o$ are obtained

form solving the time-independent Schrödinger

$$\hat{H}_o \left|n\right\rangle = E_n \left|n\right\rangle \tag{3.4}$$

where E_n is the eigenvalue of the state $|n\rangle$. The states $\{|n\rangle\}$ form are complete basis set and a linear combination of these states can describe any state. We are interested in finding out the dynamics of the system after the system has interacted with the electric field. To obtain this information we want to estimate the state of the molecular system under the influence of the electric field. The system can be described as

$$\left|\Psi\right\rangle = \sum_n a_n(t) e^{-iE_n t/\hbar} \left|n\right\rangle \tag{3.5}$$

The wavefunction $|\Psi\rangle$ satisfies the time-dependent Schrödinger equation

$$i\hbar \frac{\partial \left|\Phi\right\rangle}{\partial t} = \hat{H} \left|\Phi\right\rangle \tag{3.6}$$

The time-dependent Schrödinger equation couples the set of coefficients $\{a_n(t)\}$. For the molecular system with only two states, ground state g and excited state e 3.5 and 3.6 give

$$\begin{aligned} \frac{\partial a_e(t)}{\partial t} &= \frac{i}{\hbar} a_g(t) e^{-i\omega_{eg}t} \mu_{eg} E(t) \\ \frac{\partial a_g(t)}{\partial t} &= \frac{i}{\hbar} a_e(t) e^{+i\omega_{eg}t} \mu_{ge} E(t) \end{aligned} \tag{3.7}$$

where $\omega_{eg} = (E_e - E_g)/\hbar$ and $\mu_{eg} = \langle e \left|\hat{\mu}\right| g \rangle$ is the transition dipole moment. From the coupled set of equations 3.7 we can conclude that the application of electric field leaves the system in a superposition of the ground state g and excited state e. The exact value of a_g and a_e is not as important as understanding that they are not zero. At time t after the

electric field has interacted with the system, the system is described as

$$|\Psi(t)\rangle = a_g e^{-iE_g t/\hbar} |g\rangle + a_e e^{-iE_e t/\hbar} |e\rangle \tag{3.8}$$

The linear superposition of states, a wavepacket, has intrinsic time dependence which is described by the response function of the molecular system. The intrinsic time dependence of wavepacket gives rise to homogeneous linewidth. Semiclassically wavepacket can be interpreted as the electric field pushing and pulling on the charges of the molecular system, hence creating polarization in the molecular level. Quantum mechanically polarization $P(t)$ is the expectation value of the dipole operator and is given as

$$\begin{aligned} P(t) &= \langle \hat{\mu} \rangle \\ &= \langle \Psi(t) | \hat{\mu} | \Psi(t) \rangle \\ &= 2Re\left(a_g^* a_e e^{-i\omega_{eg} t} \langle g | \hat{\mu} | e \rangle \right) + \underbrace{a_g^* a_g \langle g | \hat{\mu} | g \rangle + a_e^* a_e \langle e | \hat{\mu} | e \rangle}_{constant} \end{aligned} \tag{3.9}$$

From 3.9 we can conclude that application of the electric field results in charges oscillating about a mean position. From Maxwell's equations we can conclude that accelerated or deaccelerated charges result in emission of electromagnetic fields. Hence forth I will not consider the constants that contribute to $P(t)$ as they do not contribute to an electromagnetic signal. The emitted field is 90° out-of-phase with respect to the polarization of the system. Thus the electric field of the electromagnetic signal can be described as $-\sin(\omega_{eg} t)$. The electric field of course does not last forever, as suggested by the form, but in fact dies out after a certain amount of time that is dictated by the intrinsic lifetime of the wavepacket. A more appropriate description of $P(t)$ is $P(t) = \left|\mu_{eg}\right|^2 \cos(\omega_{eg} t - t/\tau)$ where τ is the lifetime of macroscopic polarization $P(t)$. Consequently the electromagnetic signal E_{sig} can be described as

$$E_{sig} = -\left|\mu\right|^2 \sin(\omega_{eg} t - t/\tau) \tag{3.10}$$

Fourier transform of the time domain electromagnetic signal in equation 3.10 gives the linear absorption spectrum.[2] The Characteristic lifetime τ of E_{sig} gives rise to the homogeneous line width to the absorption spectrum.

3.2 Density Matrix

In the previous section we used the eqn. 3.5 to describe the molecular system and then used eqn. 3.9 to examine the nature of polarization, and hence linear absorption signal from eqn. 3.10. We can conclude that the system must be in a linear superposition of eigenstates to create time varying polarization, and hence electromagnetic radiation. The polarization $P(t)$ in equation 3.9 had constant as well as time varying terms. But only the time varying terms contributed towards emission of the signal. The wavefunction in eqn. 3.8 can be interpreted as follows: the system has a finite probability $a_e^* a_e$ (or $|a_e|^2$) of being found in state $|e\rangle$. However, it is terms like $a_g^* a_e$ that contribute towards emission of signal. $a_e^* a_e$ is referred to as population as it gives information about the probability of occupancy of a particular state. $a_g^* a_e$ is referred to as coherence since it tells about the coherent nature of the superposition of states. The density matrix formalism lets us treat populations and coherences separately. A major advantage of density matrix formalism is that, as we will see, it allows us to treat a ensemble where that cannot be described by a single wavefunction. For example an ensemble of mixed states cannot be represented by one wavefunction but can be described by a density matrix. Below I will introduce density matrix and its operational use.

3.2.1 Introduction to density matrix

The state $|\Psi\rangle$ of a system can be expressed in a basis set $|n\rangle$ as[2]

$$|\Psi(t)\rangle = \sum_n a_n(t)\,|n\rangle \tag{3.11}$$

where $a_n(t)$ are the expansion coefficients. The expectation values of an operator, for example the dipole operator $\hat{\mu}(t)$ is given by

$$\begin{aligned}\langle\hat{\mu}(t)\rangle &= \langle\Psi(t)\,|\hat{\mu}|\,\Psi(t)\rangle \\ &= \sum_{n,m} a_n(t)a_m(t)^*\,\langle m\,|\hat{\mu}|\,n\rangle \\ &= \sum_{n,m} a_n(t)a_m^*(t)\mu_{mn} \end{aligned} \tag{3.12}$$

The above motivates the definition of the density matrix

$$\begin{aligned}\rho(t) &= \sum_{n,m} a_n(t)a_m^*(t)\,|n\rangle\,\langle m| \\ &= |\Psi(t)\rangle\,\langle\Psi(t)| \end{aligned} \tag{3.13}$$

For an ensemble of statistical mixture of states the density matrix is given as

$$\rho(t) = \sum_n p_n\,|\Psi_n(t)\rangle\,\langle\Psi_n(t)| \tag{3.14}$$

where p_n is the probability of finding a system of the ensemble in the state $|\Psi_n(t)\rangle$. The n^{th}, m^{th} element of the density matrix is thus $\rho_{n,m} = a_n(t)a_m^*(t)$ and the expectation value of the dipole operator assumes the form

$$\langle\hat{\mu}(t)\rangle = Tr\,[\hat{\mu}\rho(t)] \tag{3.15}$$

where Tr stands for the trace operator.

In order to understand linear signal (eqn. 3.10) we needed the time evolution of wave function (eqn. 3.6) and perturbative expansion of the wavefunction (eqn. 3.7, 3.8) to estimate the effect of wavepacket on molecular polarization (eqn. 3.9) that ultimately helped to understand the origin of linear signal (eqn. 3.10). To develop a similar understanding using density matrix we need to know the time evolution and perturbative expansion of the density

matrix.

3.2.2 Time Evolution of density matrix

From the definition of density matrix, eqn. 3.13 and time evolution of the wavefunction is given by eqn. 3.4, the differential form of evolution of the density matrix is given by the Liouville-von Neumann equation

$$\begin{aligned} \frac{\partial \rho}{\partial t} &= \left(\frac{\partial}{\partial t}\left|\Psi(t)\right\rangle\right)\left\langle\Psi(t)\right| + \left|\Psi(t)\right\rangle\left(\frac{\partial}{\partial t}\left\langle\Psi(t)\right|\right) \\ &= -\frac{i}{\hbar}\left[H,\rho\right] \end{aligned} \tag{3.16}$$

The above is shown for a pure state where the system is described by a single wavefunction. The density matrix that described the statistical mixture of states, eqn 3.14, is just a linear transform of pure states. The Liouville-von Neumann equation is a linear transform as well hence eqn. 3.16 holds for a statistical mixture as well.

3.2.3 Interaction picture and perturbation theory

The system is described by the Hamiltonian $\hat{H}(t) = \hat{H}_o + \hat{V}(t)$ (eqn. 3.3). H_o is the Hamiltonian that system free of any external perturbation, and $\hat{V}(t)$ is the perturbation. While the system evolves under the influence of the entire Hamiltonian $\hat{H}(t)$, we want to understand the influence of the external perturbation on the system. To that end we define a wavefunction in the "interaction" picture that removes evolution from field-free Hamiltonian. The interaction wavefunction $\left|\Psi_I(t)\right\rangle$ is defines as

$$\left|\Psi_I(t)\right\rangle = e^{\frac{i}{\hbar}\hat{H}_o(t-t_o)}\left|\Psi(t)\right\rangle \tag{3.17}$$

Using the time dependent Schrödinger equation, eqn. 3.6 we get the time evolution of the wavefunction in the interaction picture

$$\frac{\partial}{\partial t}\left|\Psi_I(t)\right\rangle = -\frac{i}{\hbar}\hat{V}_I(t)\left|\Psi_I(t)\right\rangle \tag{3.18}$$

where the operator $\hat{V}_I(t)$ is the matter-field Hamiltonian in the interaction picture, given as

$$\hat{V}_I(t) = e^{\frac{i}{\hbar}\hat{H}_o(t-t_o)}\hat{V}(t)e^{-\frac{i}{\hbar}\hat{H}_o(t-t_o)} \tag{3.19}$$

The definition in eqn. 3.19 is true for any operator in the interaction picture. Using eqns. 3.18 and 3.19, we arrive at the perturbative expansion of wavefunction

$$\begin{aligned}\left|\Psi(t)\right\rangle = \left|\Psi^{(0)}(t)\right\rangle + \sum_{n=1}^{\infty}\left(-\frac{i}{\hbar}\right)^n \int_{t_0}^{t} d\tau_n \int_{t_0}^{\tau_n} d\tau_{n-1}... \int_{t_0}^{\tau_2} d\tau_1 \times \\ e^{-\frac{i}{\hbar}\hat{H}_0(t-\tau_n)}\hat{V}(t_n)e^{-\frac{i}{\hbar}\hat{H}_0(\tau_n-\tau_{n-1})}\hat{V}(t_{n-1})... \\ e^{-\frac{i}{\hbar}\hat{H}_0(\tau_2-\tau_1)}\hat{V}(\tau_1)e^{-\frac{i}{\hbar}\hat{H}_0(\tau_1-t_0)}\left|\Psi(t_0)\right\rangle\end{aligned} \tag{3.20}$$

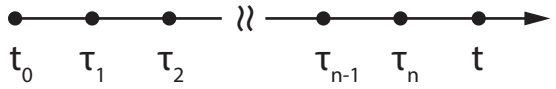

Figure 3.2: Ordering of time variables in a perturbative expansion of wavefunction in interaction picture. The figure shows time ordering in the n^{th} term of the expansion. The interaction takes place at times $\tau_1, \tau_2, ...\tau_n$ and the system evolves under the field free Hamiltonian, H_0, between any two interactions.

The eqn. 3.20 can be interpreted using figure 3.2. The n^{th} term in the expansion includes n matter-field interactions. The n matter-field interactions take place in a time ordered fashion at $\tau_1, \tau_2, ...\tau_n$. In between any two interactions the system evolves under the matter-free Hamiltonian, H_0.

Just as the wavefunction was defined in the interaction picture and then expanded using

the time dependent Schrödinger equation, we can define the density matrix in the interaction picture as

$$\rho_I(t) = e^{\frac{i}{\hbar}\hat{H}_0(t-t_0)}\rho(t)e^{-\frac{i}{\hbar}\hat{H}_0(t-t_0)} \tag{3.21}$$

and there after using the Liouville-von Neumann equation (3.16) we get the perturbative expansion of the density matrix given as

$$\begin{aligned}\rho(t) = \rho^{(0)}(t) + \sum_{n=1}^{\infty}\left(-\frac{i}{\hbar}\right)^n \int_{t_0}^{t} d\tau_n \int_{t_0}^{\tau_n} d\tau_{n-1} \ldots \int_{t_0}^{\tau_2} d\tau_1 \times \\ e^{-\frac{i}{\hbar}\hat{H}_0(t-t_0)}\left[\hat{V}_I(\tau_n), \left[\hat{V}_I(\tau_{n-1}), \ldots \left[\hat{V}_I(\tau_1), \rho(t_0)\right] \ldots\right]\right] e^{\frac{i}{\hbar}\hat{H}_0(t-t_0)}\end{aligned} \tag{3.22}$$

where $\rho^{(0)}(t)$ is the unperturbed density matrix and $\hat{V}_I(\tau)$ is the matter-field interaction in the interaction picture. The n^{th} term in the density matrix, $\rho^{(n)}(t)$, is interpreted in the same way as the the n^{th} term in the perturbative expansion of the wave function. The only extra point to note here is the interpretation coming from the application of commutators. Because of the commutators, $\hat{(}V)_I(\tau)$ can interact with the density matrix ρ either from the left or from the right; the two modes of interactions have different effect on the direction in which the signal will be emitted. More on this later.

3.3 Polarization

In order to understand spectroscopic signals using density matrix we need to be able to evaluate polarization in terms of density matrix. As give by eqn. 3.12, expectation value of the an operator is given by the trace over the density matrix. The macroscopic polarization $P(t)$ is given by the tracing the dipole operator over the density matrix

$$P(t) = Tr\left[\hat{\mu}\rho(t)\right] \tag{3.23}$$

where $\hat{\mu}$ is the dipole operator. The n^{th} order polarization that depends the n^{th} power of electric field is given by (after changing variables)

$$\begin{aligned} P^{(n)}(t) &= Tr\left[\hat{\mu}\rho^{(n)}(t)\right] \equiv \left\langle \hat{\mu}\rho^{(n)}(t)\right\rangle \\ &= -\left(-\frac{i}{\hbar}\right)^n \int_0^\infty d\tau_n \int_0^\infty d\tau_{n-1} ... \int_0^\infty d\tau_1 E(t-t_n)E(t-t_n-t_{n-1})...E(t-t_n-t_{n-1}...-t_1) \\ &\langle \hat{\mu}(t_n+...t_1)\left[\hat{\mu}(t_{n-1}+...t_1),\left[\hat{\mu}(t_{n-2}+...t_1),...\left[\hat{\mu}(0),\rho(0)\right]...\right]\right]\rangle \end{aligned} \tag{3.24}$$

The equation 3.24 can be interpreted in the following way. The n^{th} order polarization is

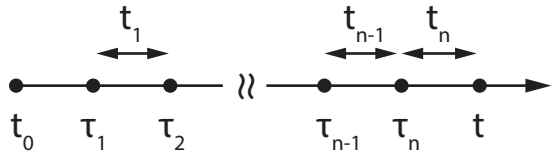

Figure 3.3: Time ordering of time intervals for perturbatively evaluating n^{th} order polarization. The matter-field interactions takes place at times $\tau_1, \tau_2, ...\tau_n$ and $t_1, t_2, ...t_n$ are the corresponding time intervals between the interactions during which the system evolves under the free Hamiltonian, H_0.

determined by the n system field interaction that take place at $t_1, t_2, ...t_n$ time intervals. The system is intially in equilibrium state and the time of first matter field interaction is set as the origin of time. The corresponding density matrix and dipole moment at the first interaction are $\rho(0)$ and $\hat{\mu}(0)$. The polarization is generated by components that are intrinsic to the system, i.e the equilibrium density matrix and the transition dipole moments, and components that are extrinsic to the system, i.e electric field. The invariant intrinsic properties of the system can be lumped up into what is called response function. Given the response function of the system, polarization can be evaluated when given the external perturbating electric field. In terms of response function, the n^{th} order polarization can be

expressed as

$$P^{(n)}(t) = -\left(-\frac{i}{\hbar}\right)^n \int_0^\infty d\tau_n \int_0^\infty d\tau_{n-1} ... \int_0^\infty d\tau_1 R^{(n)}(t_1, ..., t_n) \times E(t - t_n) E(t - t_n - t_{n-1}) ... E(t - t_n ... - t_1) \tag{3.25}$$

where the n^{th} order response function $R^{(n)}$ is given by

$$R^{(n)}(t_n, ..., t_1) = -\left(-\frac{i}{\hbar}\right)^n \times \langle \hat{\mu}(t_n + ...t_1) \left[\hat{\mu}(t_{n-1} + ...t_1), \left[\hat{\mu}(t_{n-2} + ...t_1), ... \left[\hat{\mu}(0), \rho(0)\right] ...\right]\right]\rangle \tag{3.26}$$

The response function is single sided which means $R^{(n)}(t_n, ..., t_1) \neq 0$ when all time intervals are positive, i.e $t_1 > 0, ..., t_n 0$.

3.4 Rotating wave approximation and Feynman pathways

I will now show how to figure out different components of spectroscopic signals through response functions using Feynman diagrams under the rotating wave approximation. I will use first order response function with a two level system as an example to explain the involved principles.

3.4.1 Linear Response function and a two level system

From eqn. 3.26 the linear response function $R^{(1)}(t)$ is given as

$$\begin{aligned} R^{(1)}(t_1) &= i \langle \hat{\mu}(t_1), [\hat{\mu}(0), \rho(0)]\rangle \\ &= i \langle \hat{\mu}(t_1)\hat{\mu}(0)\rho(0)\rangle - i \langle \rho(0)\hat{\mu}(0)\hat{\mu}(t_1)\rangle \qquad (3.27) \\ &= R_1^{(1)}(t_1) - R_2^{(1)}(t_1) \qquad (3.28) \end{aligned}$$

Each of the terms in the linear response function are visualized using the Feynman diagrams. Let's first take a look at $R_1^{(1)}(t_1)$.[1] We first begin with the equilibrium density matrix. For a two state system with ground state $|g\rangle$ and excited state $|e\rangle$, the density matrix $\rho(t)$ at any time t will be a $2x2$ matrix where the diagonal elements are molecular system's probability of being in either of the two states. The $(1,1)^{th}$ element, ρ_{11} is the probability of finding the system in ground state and $(2,2)^{th}$ element of the density matrix, ρ_{22}, is the probability of finding the system in excited state. The off-diagonal elements of the density matrix, ρ_{12} and ρ_{21}, represent coherence between states. At time $t = 0$ system can be assumed to be in the ground state if we are only considering electronic transitions. The underlying assumption is that thermal energy is way smaller than electronic energy. Therefore

$$\rho(0) = \begin{pmatrix} 1 & 0 \\ 0 & 0 \end{pmatrix} \tag{3.29}$$

As deduced previously only the transition dipole moment contribute to electronic spectroscopic signals. In a matrix representation, the off-diagonal elements of the dipole operator are the transition dipoles and the diagonal elements are the permanent dipoles. For simplicity I will consider only the off-diagonal elements of the dipole operator. The strength of the transition dipole is μ_{eg}. The dipole matrix is

$$\mu = \begin{pmatrix} 0 & \mu_{ge} \\ \mu_{eg} & 0 \end{pmatrix} \tag{3.30}$$

Now consider the case of $R_1^1(t)$. The dipole operator operates on the density matrix on the left

$$\mu(0)\rho(0) = \begin{pmatrix} 0 & \mu_{ge} \\ \mu_{eg} & 0 \end{pmatrix} \times \begin{pmatrix} 1 & 0 \\ 0 & 0 \end{pmatrix} = \begin{pmatrix} 0 & 0 \\ \mu_{eg} & 0 \end{pmatrix} \tag{3.31}$$

Thus density matrix's first interaction with the dipole operator from the left creates an $|e\rangle\langle g|$ coherence. After the first interaction the system evolves phase under the influence of the field-free Hamiltonian, H_0, as deduced from eqns. 3.17 and 3.21. Since the interaction before phase evolution took place from the left, phase evolves on the left side of the density matrix as $e^{-i\omega_{eg}t_1}$, where $\omega_{eg} = (E_e - E_g)/\hbar$. From eqn. 3.31,

$$e^{-i\omega_{eg}t_1}\mu(0)\rho(0) = \begin{pmatrix} 0 & 0 \\ e^{-i\omega_{eg}t_1}\mu_{eg} & 0 \end{pmatrix} \tag{3.32}$$

Therefore first matter field interaction results in the creation of $|e\rangle\langle g|$ coherence that evolves as with the phase $e^{-i\omega_{eg}t_1}$. The coherence results in the emission of electromagnetic field. This emission is the second interaction that takes place that at t_1 time interval after the first interaction. From equation 3.32,

$$\langle\hat{\mu}(t_1)\hat{\mu}(0)\rho(0)\rangle = \begin{pmatrix} 0 & \mu_{ge} \\ \mu_{eg} & 0 \end{pmatrix} \times \begin{pmatrix} 0 & 0 \\ e^{-i\omega_{eg}t_1}\mu_{eg} & 0 \end{pmatrix} = \begin{pmatrix} \mu_{ge}\mu_{eg}e^{-i\omega_{eg}t_1} & 0 \\ 0 & 0 \end{pmatrix} \tag{3.33}$$

Hence upon emission the system goes back to the ground state. We can summarize the sequence as follows. The system starts off in the ground state population $|g\rangle\langle g|$. Immediately after the first interaction from the left the system lands in the $|e\rangle\langle g|$ and evolves phase as $e^{-i\omega_{eg}t_1}$ for t_1 time period. Upon signal emission an interval of t_1 the system goes to the ground state population, $|g\rangle\langle g|$. Using the method above we can show that the second term in eqn. 3.28 is complex conjugate of the first term. The second term can be interpreted as follows. The first interaction from the right transitions the system from the ground state population $|g\rangle\langle g|$ to the coherence $|g\rangle\langle e|$. The phase evolves as $e^{i\omega_{eg}t_1}$ since the first interaction took place on the right. After phase evolution for t_1 time duration, signal emission results in the system relaxing back to ground state. The above interpretation of the response functions can be drawn as Feynman diagrams with rotating wave approximation as discussed

in the following subsection.

3.4.2 Rotating wave approximation

From the last section the linear response function goes as

$$R_1^{(1)} = i\mu_{ge}\mu_{eg}e^{-i\omega_{eg}t_1 - t_1/\tau} \tag{3.34}$$

The applied electric field convolutes with the response function to generate macroscopic polarization $P^{(1)}(t)$ as described by the general case in eqn. 3.25. For first order polarization,

$$P^{(1)}(t) = \int_0^\infty dt_1 R^{(1)}(t_1)E(t - t_1) \tag{3.35}$$

The electric field used in ultrafast experiments can be described as a sinusoidal wave with a pulse envelope that lasts for a few femtoseconds. So the field can be something like $E(t) = A(t)\cos(\omega t)$. It is useful to write the field in terms of complex exponentials as

$$\begin{aligned} E(t) = 2 * A(t)\cos(\omega t) &= A(t)\left(e^{-i\omega t} + e^{+i\omega t}\right) \\ &= A(t)e^{-i\omega t} + A^*(t)e^{+i\omega t} \end{aligned} \tag{3.36}$$

Here $A(t)$ and $A^*(t)$ are the same but the "$*$" is used as a bookkeeping tool for the complex conjugate. Although I have only shown temporal evolution, the electric field also has spatial evolution determined by the wavevector $\vec{k}$ and the total phase evolves as $\vec{k}.\vec{r} - \omega t$ where $\vec{r}$ is spatial coordinate. Above notation helps to associate $A(t)$ with $+\vec{k}$ (propagating right for reference), and $A^*(t)$ with $-\vec{k}$ (propagating left). Assuming that the field is resonant with

the energy levels, i.e $\omega = \omega_{eg}$, polarization becomes

$$P^{(1)}(t) \propto ie^{-i\omega t} \int_0^\infty d\tau_1 A(t-t_1)e^{-t_1/\tau} + ie^{i\omega t} \int_0^\infty d\tau_1 A^*(t-t_1)e^{-t_1/\tau}e^{-i2\omega t_1} \tag{3.37}$$

The second integral has a term that oscillates at optical frequency and does not survive integration. The second term has a slowing varying term that survives the integration and contributes to polarization. The equation 3.37 uses $R_1^{(1)}$ in which the first interaction takes place from the left. Eqn. 3.9 can be interpreted as follows. $R_1^{(1)}$ contributes to polarization in which the dipole operator interacts with the density matrix from the left. The interaction on the left can take in two ways. One with pulse envelope $A(t)$ and other with pulse envelope $A^*(t)$. The term with pulse envelope $A(t)$ survives and not the term with containing $A^*(t)$. In other words, the interaction coming from wavevector $+\vec{k}$ survives the rotating wave approximation and not the interaction coming from wavevector $-\vec{k}$.

3.4.3 Feynman diagrams for linear response functions

Using the understanding from previous sections we can now start drawing Feynman diagrams to understand how the various components of the response function contribute to spectroscopic signal.

Figure 3.4 shows Feynman diagrams for the two integrals in eqn. 3.37. There are essentially two components to writing Feynman diagrams. First, the evolution of density matrix after each interaction. Second, the direction of arrows at each interaction. Let's first consider the evolution of density matrix. In the Feynman diagram time propagates from the bottom to the top. From section 3.4.1, the system starts off in the ground population state which is shown in both figure 3.4(a)(b) at the bottom as $|g\rangle\langle g|$ population. After the first interaction from the left the system goes into the $|e\rangle\langle g|$ coherence which is shown in both figure 3.4(a)(b). The system evolves for time period t_1 after which the signal emission leaves

the system in the ground state. Both figures 3.4(a)(b) follow the correct evolution of density

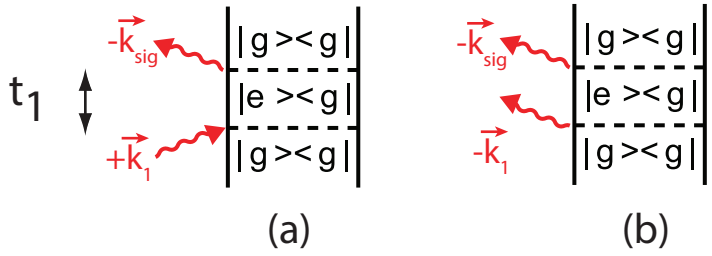

Figure 3.4: (a): Part of the linear response function in which first interaction takes place on the left and survives the rotating wave approximation. (b): Part of the linear response function in which first interaction takes place on the left and does not survive the rotating wave approximation.

matrix elements. From eqn. 3.37 two terms contribute to macroscopic polarization - first involves $A(t)$ and the second involves $A^*(t)$. $A(t)$ is associated with wavevector $+\vec{k}$ and $A^*(t)$ is associated with wavevector $-\vec{k}$. By convention $+\vec{k}$ is taken to point left and $-\vec{k}$ points left. Hence in the two Feynman diagrams in figure 3.4, while both interactions take place on the left, figure 3.4(a) shows arrows pointing right with $+\vec{k}$, and figure 3.4(b) shows arrows pointing right with $-\vec{k}$. However, only figure 3.4(a) shows the term that survives rotating wave approximation. Above I have only shown contribution from $R_1^{(1)}$ and not from its complex conjugate. The Feynman diagram for the complex conjugate will involve first interaction from the right with a $-\vec{k}$ wavevector.

Figure 3.4(a) can be interpreted in the following way. The first pulse interacts with the system in the ground state $|g\rangle$ and transitions the system into the excited state $|e\rangle$, while simultaneously creating the $|e\rangle\langle g|$. Arrow pointing into the Feynman diagram can be interpreted as absorption as in the case of first interaction. The arrow pointing away from the Feynman diagram can be interpreted as emission as in the case of signal. Since the arrow points right, the signal wavevector is annotated $-\vec{k}_{sig}$. The direction in which signal is emitted can be determined from momentum conservation i.e $\sum_i \vec{k}_i = 0$. This implies $-\vec{k}_{sig} + \vec{k}_1 = 0$, or that $\vec{k}_{sig} = \vec{k}_1$. The signal is thus emitted in the same direction as the beam that is responsible for the first matter-field interaction.

3.4.4 Feynman diagrams for 3^{rd} order non-linear response functions

In terms of 3^{rd} order non-linear response functions, 3^{rd} order polarization can be written as[2;3]

$$P^{(3)}(t) = \int_0^\infty dt_3 \int_0^\infty dt_2 \int_0^\infty dt_1 R^{(3)}(t_1, t_2, t_3) \times \\ E_3(t - t_3) E_2(t - t_3 - t_2) E_1(t - t_3 - t_2 - t_1) \tag{3.38}$$

where the 3^{rd} order response function is given as

$$R^{(3)}(t_1, t_2, t_3) = \left(\frac{i}{\hbar}\right)^3 \theta(t_3)\theta(t_2)\theta(t_1) \times \\ \sum_{j=1}^{4} \left[R_j^{(3)}(t_1, t_2, t_3) - R_j^{(3)}(t_1, t_2, t_3)^* \right] \tag{3.39}$$

where θ's are Heaviside step functions that ensure causality, i.e. there is no third order polarization before interaction with the pulses, and

$$R_1^{(3)}(t_1, t_2, t_3) = \left\langle \hat{\mu}(t_1 + t_2 + t_3)\hat{\mu}(t_1 + t_2)\hat{\mu}(t_1)\hat{\mu}(0)\rho_{eq} \right\rangle \tag{3.40}$$

$$R_2^{(3)}(t_1, t_2, t_3) = \left\langle \hat{\mu}(t_1 + t_2 + t_3)\hat{\mu}(0)\rho_{eq}\hat{\mu}(t_1)\hat{\mu}(t_1 + t_2) \right\rangle \tag{3.41}$$

$$R_3^{(3)}(t_1, t_2, t_3) = \left\langle \hat{\mu}(t_1 + t_2 + t_3)\hat{\mu}(t_1)\rho_{eq}\hat{\mu}(0)\hat{\mu}(t_1 + t_2) \right\rangle \tag{3.42}$$

$$R_4^{(3)}(t_1, t_2, t_3) = \left\langle \hat{\mu}(t_1 + t_2 + t_3)\hat{\mu}(t_1 + t_2)\rho_{eq}\hat{\mu}(0)\hat{\mu}(t_1) \right\rangle \tag{3.43}$$

The for each of $R_1^{(3)}$,$R_2^{(3)}$,$R_3^{(3)}$ and $R_4^{(3)}$ there is only one Feynman diagram that survives rotating wave approximation. The corresponding Feynman diagrams are shown in figure 3.6. Signals corresponding to $R_1^{(3)}$ and $R_2^{(3)}$ are emitted in $+\vec{k}_1 - \vec{k}_2 + \vec{k}_3$ direction, and those corresponding to $R_3^{(3)}$ and $R_4^{(3)}$ are emitted in $-\vec{k}_1 + \vec{k}_2 + \vec{k}_3$ direction. $R_1^{(3)}$ and $R_2^{(3)}$ are called 'non-rephasing' pathways, and $R_3^{(3)}$ and $R_4^{(3)}$ are called rephasing pathways. The distinction between the two is not only the direction in which they are emitted but also the

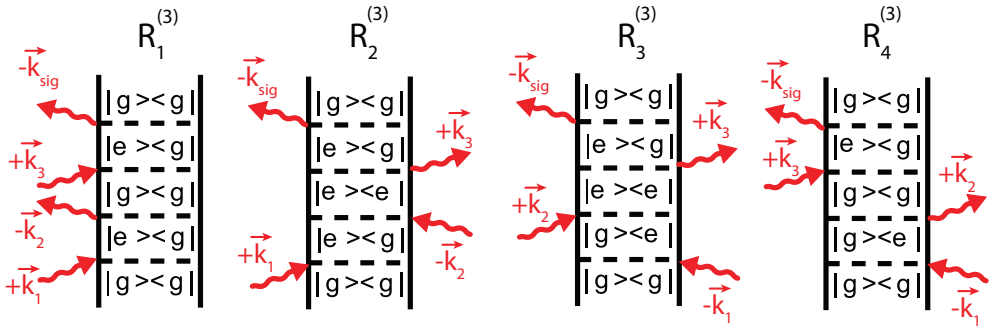

Figure 3.5: $R_1^{(3)}$ and $R_2^{(3)}$ are ground state bleach and excited state emission signals emitted in $+\vec{k}_1 - \vec{k}_2 + \vec{k}_3$. $R_3^{(3)}$ and $R_4^{(3)}$ are excited state emission and ground state bleach signals emitted in $-\vec{k}_1 + \vec{k}_2 + \vec{k}_3$.

manner in which the phase evolves. If we refer to $+i\omega t$ and $-i\omega t$ as two different directions of phase evolution, then non-rephasing signals evolve phase in the same direction during t_1 and t_3 time periods, while rephasing signals evolve phase in different directions. In fact the difference in phase evolution in time domain is tied up phase evolution in spatial domain and shows up as difference in the direction in which the signal is emitted. The dynamics reported by both rephasing and non-rephasing signals is identical.

3.5 2D Electronic Spectroscopy

In the last sections I introduced the background for two-dimensional electronic spectroscopy (2D ES) as understood in terms of non-linear response functions. Below I will briefly present the principles behind the experimental implementation of 2D ES.

I will take the example of $R_3^{(3)}$ but the principles are the same for all 3^{rd} order response functions. The generic time intervals t_1, t_2 and t_3 are usually replaced by τ, T and t, respectively. The time period τ is called coherence time during which the coherence evolves after first interaction. The second time period T is called the waiting time and it is the time period during which the dynamics of excited state takes place. The third time period t is called the rephasing time and the phase during this time period evolves in the opposite direction compared to that during coherence time. During coherence time phase evolves as

$\exp(+i\omega t)$ and during the rephasing time coherence evolves as $\exp(-i\omega t)$. During coherence

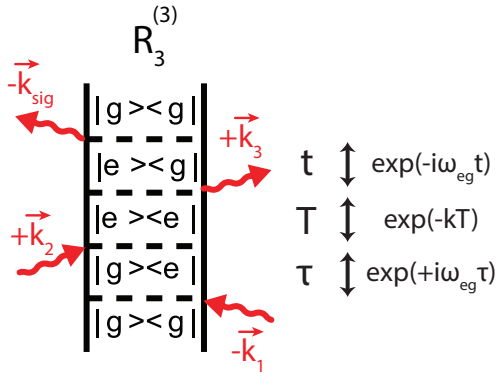

Figure 3.6: Phase evolution as a function of τ, T and t time intervals for the rephasing response function $R_3^{(3)}$.

and rephasing times, phase evolves at optical frequency. During waiting time phase evolves much slowly. The dominant time dependence is exponential dynamics with life-times of picoseconds. The difference in time dependence during coherence/rephasing time and waiting time drives experimental design. The goal is to successfully scan the time delays and thereafter perform data analysis.

3.5.1 Design of a two-dimensional electronic spectrometer

The figure 3.7 shows an overview of the laser table with all the essential components required for molecular systems that I have studied. I will briefly discuss each of these components.

- *Oscillator:* The oscillator essentially has three components. First, the pump beam at 532 nm, second Ti:Sapphire gain medium and third the laser cavity. The gain medium is a Ti:Sapphire crystal that is placed in the laser cavity. The laser cavity has a few essential components but the most important ones are the end mirrors that form the boundary of the cavity. The pump beam excites the Ti:Sapphire crystal. The excited states relax to the ground state by fluorescing at 808 nm. The fluorescence is captured by the end mirrors and the distance between the end mirrors limits the wavelengths

that survive in the cavity. A combination of passive mode-locking, Kerr lens mode-locking and stimulated emission from the Ti:Sapphire crystal result in the formation of ultrafast laser pulse. The pulse makes one round trip of the cavity and a part of the pulse gets transmitted through one of the end mirrors. The rate at which the pulse is emitted depends on the length of the cavity. The output of the oscillator in use is 80 MHz, centered at 805 nm with 50 nm of FWHM.

- *Regenarative amplifier:* The output of the oscillator does not have enough power to perform experiments with. The pulse has to be amplified to achieve sufficient laser power. This is achieved using the regenerative amplifier. The principle of amplification is same as the principle of generating laser pulse. In the amplifier a pump beam at 532 nm creates excited states and the seed form the oscillator stimulates emission from the excited states. The power of the laser pulse depends on the power of the pump beam. In our case it is usually 16 W. The process of amplifying and dumping the pulse out of the cavity is done by carefully timing the Pockels cells. The output of the amplifier is 3 W, and it is high enough to burn the Ti:Sapphire crystal if the peak power of the seed if high. In order to avoid this problem, the seed first goes through the stretcher and then to the amplifier. The stretcher is a combination of gratings and mirrors that apply temporal chirp to the seed beam and render the seed beam uncompressed. Consequently the peak power of the seed beam is not high and hence of the amplifier output. Thus the Ti:Sapphire crystal in the amplifier does not burn. The output of the amplifier has the temporal chirp of the seed beam. The chirped output pulse of the amplifier is then compressed using a combination of gratings and mirrors in the compressor. The output of the compressor is a 35 fs laser pulse with 1.5 W at 5 kHz repetition rate.

- *White light generation and MIIPS:* The bandwidth achieved form the regenerative amplifier, 30 nm fwhm centered at 805 nm is not sufficient to study a variety of

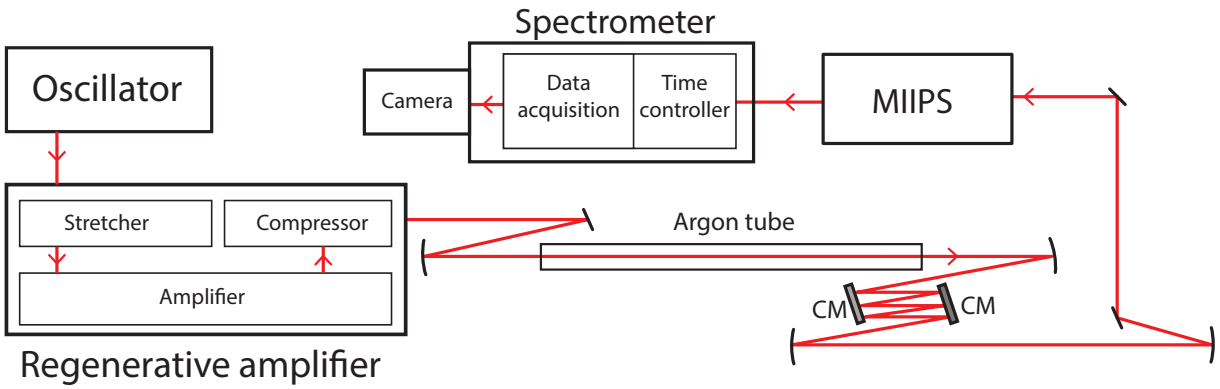

Figure 3.7: The oscillator produces laser pulses centered at 805 nm with 50 nm of FWHM at 80 MHz repetition rate. The regenerative amplifier first temporally stretches the pulse using a stretcher, then amplifies the power using an amplifier and then finally compresses the pulse. The output of regenerative amplifier is a 2W, 5 kHz pulse train centered at 800 nm with 30 nm FWHM. The output of the regenerative amplifier is focused into the argon tube to broaden the bandwidth. The pulse then bounces off a couple of chirp mirrors and is focused again in air to extend the bandwidth to include longer wavelengths. MIIPS is used to compress the pulse. A translation stage is used to control the relative timing between pulses 1-2 and 3-4. The pulses are focused into a homogeneous sample and the emitted signal is acquired using a camera.

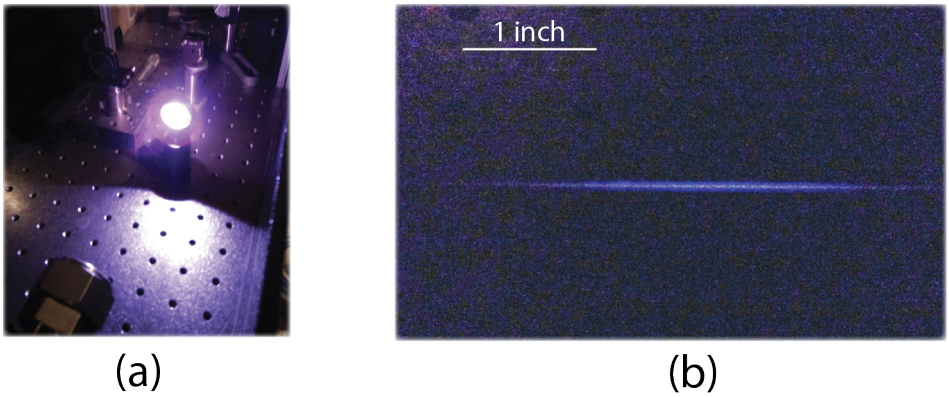

Figure 3.8: (a) The output of the regenerative amplifier is focused into the argon tube that expands the bandwidth and gives white light containing wavelengths from 650 nm to 870 nm as shown here. (b) The output of the argon gas tube bounces off chirp mirrors and is focused in air that results in formation of a filament as shown above. Focusing in air pushes the bandwidth to 890 nm.

photosynthetic antenna complexes. To overcome the bandwidth problem we focus the pulse in an argon tube. Focusing into the argon tube results in multi-photon processes that broadens the bandwidth from 650 nm to 870 nm. The output from the argon then bounces off chirped mirrors (CM). The chirped mirrors apply temporal chirp to the pulse which is then focused in air using curved mirrors. Focusing in the air further broadens the pulse, specially at even longer wavelengths, to generate pulse that spans from 650 nm to 890 nm (3.8). The generated pulse is then directed into the MIIPS (multiphoton intrapulse interference phase scan method). MIIPS frequency resolves the pulse and uses a spatial filter to select colors from 730 nm to 890 nm. After the frequency selection, MIIPS uses non-linear processes to remove temporal chirp from the pulse.

- *Timing controller and phase stability:* One of the important considerations for successful for performing 2D ES experiments is carefully controlled timing and phase stability. This specially matters a lot for sampling coherence time τ and rephasing time t. The signal during the coherence time and rephasing time oscillates at optical frequencies. The signal acquired during the coherence time and rephasing time is then Fourier transformed to obtain absorption frequencies and emission frequencies. Accurate measurement of absorption and emission frequencies requires accurate control over timing between the pulses. Figure 3.9 shows a schematic of the time controller for each of the beams in a typical 2D ES experiment. The incoming beam bounces off of a beam splitter (BS) and splits into two beams. The transmitted beam is used to further make beams 1 and 2, and the reflected beam is used to make beams 3 and 4. The reflected beam bounces off of a retro reflector mounted on a translation stage that provides waiting time domain T. The beams 1-2 and 3-4 go through the transmissive optic and the first order diffraction is used to give beams 1 and 2 from beam 1-2, and beams 3 and 4 form beam 3-4. The beams are collimated and each beam travels through a pair of wedge optic. The wedge optic can move in and out of the path of the beams

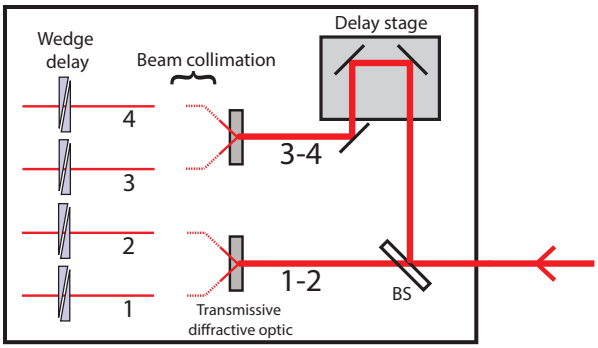

Figure 3.9: A schematic of time controller for each beam. A beam splitter (BS) is used to make a copy of the incoming beam. The transmitted beam goes through a transmissive, diffractive optic to give beam 1 and 2. The beam reflected from the BS is bounces off of a retro-reflector mounted on a translation stage. The translation stage provides the waiting time domain T and the beam goes through the transmissive, diffractive optic to give beams 3 and 4. Each of the beams, 1,2,3 and 4, go through a pair of wedge optic that controls the timing of each of the pulses by changing the amount of glass in each beam's path.

and there by changing the amount of glass in the beam path control the timing of the pulses.

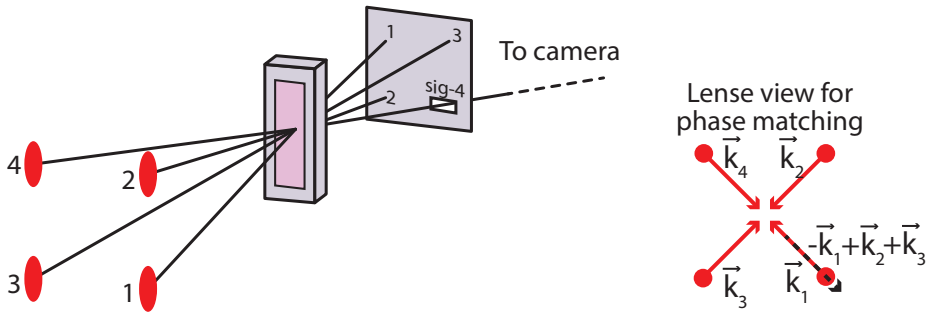

Figure 3.10: The four beams, beam 1,2,3 and 4, with wavevectors $\vec{k}_1$,$\vec{k}_2$,$\vec{k}_3$ and $\vec{k}_4$, respectively, are focused at the sample and the signal is emitted in the $-\vec{k}_1 + \vec{k}_2 + \vec{k}_3$ direction.

- *Sample position:* After the machinery for controlling the timing between the pulses is set, the beams are focused at the sample in a non-colinear geometry. Figure 3.10 shows a typical beam alignment in a 2D ES experiment. The wavevectors of the four beams 1,2,3 and 4, are $\vec{k}_1$,$\vec{k}_2$,$\vec{k}_3$ and $\vec{k}_4$, respectively. The rephasing signal is emitted in the direction of beam 4 which is the same as $-\vec{k}_1 + \vec{k}_2 + \vec{k}_3$. The emitted signal is then directed into the camera where the signal is first frequency resolved and then images

onto the detector. Because the signal is frequency resolved, the emission frequency is automatically achieved and there is no need to scan the rephasing domain t.

3.5.2 GRAPES

The previous section described basic elements for implementing two-dimentional electronic spectroscopy. Gradient assisted photon echo spectroscopy is one particular realization of two-dimensional electronic spectroscopy. It differs from conventional 2DES spectrometer designs in how it encodes timing between pulses. Conventional spectrometers focus the pulses to a point and vary the timing between them by using translation stages. In GRAPES, pulses are focused to a line and timing between them is encoded by creating a spatial gradient between them as shown in figure 3.11.[5–7] This method of encoding timing makes GRAPES

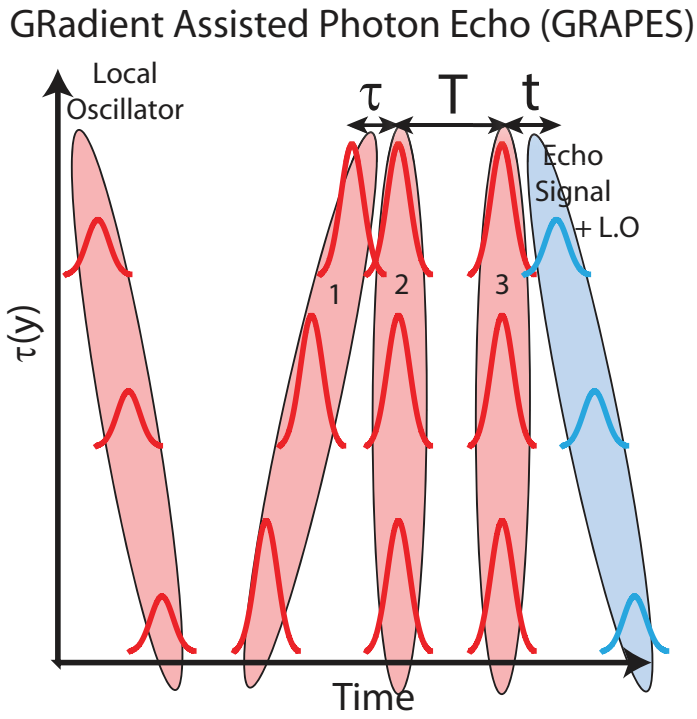

Figure 3.11: Instead of focusing the pulses to a point, in GRAPES pulses are focused to a line and timing is encoded between them by creating a spatial gradient.

a single shot technique, and has provided tremendous improvement in signal to noise ratio. GRAPES enables acquisition of a 2D map in a single shot and this capability has been

recently achieved.

3.6 References

[1] Hamm, P., and Zanni, M. *Concepts and Methods of 2D Infrared Spectroscopy*; Cambridge University Press, 2011.

[2] Mukamel, S. *Principles of Nonlinear Optical Spectroscopy*; Oxford University Press: New York, 1995.

[3] Cho, M. *Two-Dimensional Optical Spectroscopy*; Taylor & Francis, 2010.

[4] Jonas, D. M. (2003) TWO-DIMENSIONAL FEMTOSECOND SPECTROSCOPY. *Annual Review of Physical Chemistry 54*, 425–463.

[5] Harel, E., Fidler, A. F., and Engel, G. S. (2010) Real-time mapping of electronic structure with single-shot two-dimensional electronic spectroscopy. *Proceedings of the National Academy of Sciences of the United States of America 107*, 16444–16447.

[6] Harel, E., Fidler, A. F., and Engel, G. S. (2010) Single-Shot Gradient-Assisted Photon Echo Electronic Spectroscopy. *The Journal of Physical Chemistry A 115*, 3787–3796.

[7] Dahlberg, P. D., Fidler, A. F., Caram, J. R., Long, P. D., and Engel, G. S. (2013) Energy Transfer Observed in Live Cells Using Two-Dimensional Electronic Spectroscopy (vol 4, pg 3636, 2013). *Journal of Physical Chemistry Letters 4*, 3977–3977, 259WS Times Cited:0 Cited References Count:1.

CHAPTER 4

GRAPES AND INDEPENDENT PHASING OF REPHASING AND NON-REPHASING SPECTROSCOPIC SIGNALS

4.1 Introduction

Two-dimensional (2D) spectroscopy, a coherent third-order nonlinear spectroscopy, probes coherence and population dynamics on the pico- and femtosecond timescales. Two-dimensional electronic spectroscopy (2DES) has provided new and important information in a variety of systems, including correlations between electrons and holes in bi-exciton states of gallium-arsenide quantum wells,[1] the effects of nanoparticle shape on electronic structure and ultrafast dynamics,[2] excitation transfer in carbon nanotubes,[3] and coherent dynamics in photosynthetic light-harvesting complexes.[4–6] Detailed reviews of the theory, experimental implementation, and data interpretation of two-dimensional spectroscopies have been published previously.[7–12] Briefly, interactions between the sample and three excitation pulses result in an oscillating dipolar response, which generates signals in phase-matched directions. By systematically varying the timing between excitation pulses, we can acquire the entire third-order, nonlinear signal.[8]

The recent development of Gradient Assisted Photon Echo Spectroscopy (GRAPES)[13;14] extends the utility of 2DES by considerably shortening acquisition times, but it poses some unique experimental challenges. For clarity, we refer to conventional experimental approaches for acquiring 2D electronic spectra as "2DES, and distinguish these from GRAPES.

Both GRAPES and 2DES involve a series of three excitation pulses (pulses $1-3$), following a fourth local oscillator (LO) pulse in time using a boxcars geometry. In 2DES, the pulses are focused to a point and the time delay between pulses 1 and 2 (coherence time, τ) and 2 and 3 (population or waiting time, T) are both scanned using linear delay stages. GRAPES obtains the same information, however it only scans one linear delay stage corresponding to the waiting time. The coherence time delay is resolved by focusing the beams to a line

and spatially encoding the timing between pulses 1 and 2 across the sample.[13;14] Pulse 1 is tilted such that the time delay between pulses 1 and 2 varies. Beams 2 and 3 are parallel, yielding a constant waiting time T at all spatial positions within the sample. This configuration acquires all relevant coherence times simultaneously for each waiting time. The emitted signal is frequency-resolved and imaged onto a charge-coupled device (CCD). The horizontal direction across the CCD detector surface encodes the signal-LO timing in an interferogram along the wavelength dimension, while the vertical dimension on the CCD detector encodes the coherence times.

For perfectly time-ordered system-field interactions, interactions with pulses 1 and 3 generate oscillating dipoles with phase propagating either in common or with opposite sign, resulting in non-rephasing or rephasing signals, respectively. These non-rephasing and rephasing signals are emitted in different phase-matched directions known as the non-rephasing and rephasing directions, respectively. These directions are determined by vector addition of the wavevectors for pulses $1-3$. However, the geometry of 2DES experiments permits the acquisition of both of these signals in the same direction by swapping the order of first two pulses. In contrast, GRAPES cannot use this method because the angle between pulses 1 and 3 results in sampling different waiting times along the length of the beam, when beam 2 precedes beam 1 (see Figure 4.6 in the appendix). As designed, GRAPES acquires signal in the rephasing phase-matched direction.

Canonical phasing procedure, or determining the absolute phase of the 2D spectra, requires acquiring both the rephasing and non-rephasing spectra and comparing their sum to pump-probe spectra. Based on the projection-slice theorem, we prove in Sec. II that rephasing and non-rephasing signals can be phased independently by comparing each to the spectrally resolved pump-probe spectra. This proof operates both inside and outside the impulsive limit. We additionally corroborate our phasing procedure with simulation. To further demonstrate the understanding developed in Sec. 4.2, we present in Sec. 4.3 a modified GRAPES geometry that acquires signals in both the rephasing and the non-rephasing

phase matched directions. The rephasing and the non-rephasing signals acquired in different phase matched directions cannot be simply added and phased in the usual way. However, the signals can be phased independently as demonstrated for laser dye IR 144, and these phased spectra can be scaled and combined to yield the purely absorptive 2D spectrum.

4.2 Theory

A frequency-dependent relative phase shift can arise from uncertainties in laser pulse timings and from dispersive components of the experimental apparatus. Because pump-probe signal is unaffected by such effects, it can be used to phase,[8;10] or correct for, the frequency-dependent phase shift the 2D spectra have acquired. Conventionally, the rephasing and non-rephasing signals are summed, and this sum is phased to acquire corrected rephasing and non-rephasing spectra. The objective of this section is to deduce the ability for signals measured in the rephasing and non-rephasing directions to be phased independently from one another using pump-probe data, rather than in sum. This advance is crucial for GRAPES, in which rephasing and non-rephasing spectra cannot be added together in a straightforward manner, due to the different experimental geometries required to acquire each signal.

The theory and experimental implementation of optical nonlinear spectroscopy have been discussed previously in great detail.[7–12] In this work, we use the definition of the third-order, nonlinear polarization,$P^{(3)}(\vec{\mu}_s, \tau, T, t)$, in the time domain defined by Jonas[15] because it includes explicit integration over arbitrary pulse envelopes rather than interaction times in the impulsive limit. Here, coherence time τ and waiting time T are defined to be the time delays between the first and second, and between the second and third pulses, respectively. These definitions, which depend only on the time delays between the centers of the pulses, are important to ensure generality of our proof for pulses of finite duration. The center of the third pulse is set as the origin of time t, and $\vec{\mu}_s$ is the direction of signal propagation. The 2D spectrum, $S^{(3)}(\omega_\tau, T, \omega_t)$, is obtained by Fourier transforming the spectrally resolved signal field over coherence time τ. Thus, ω_τ and ω_t are conjugate variables of τ and t, respectively,

related through the Fourier transform.

The spectrally resolved pump-probe spectra, $PP(T, \omega_t)$, and the properly phased 2D spectra, $S^{(3)}(\omega_\tau, T, \omega_t)$, are related by the projection-slice theorem given by[15]

$$PP(T, \omega_t) \propto Re\left(\omega_t E_{pr}(\omega_t) \int_{-\infty}^{+\infty} d\omega_\tau S^{(3)}\left(\omega_\tau, T, \omega_t\right)\right) \tag{4.1}$$

where $E_{pr}(\omega_t)$ is the electric field of the probe pulse. Following the projection-slice theorem,[16] we rewrite $S^{(3)}(\omega_\tau, T, \omega_t)$ in Eq. 4.1 as the Fourier transform of $S^{(3)}(\omega_\tau, T, \omega_t)$, then rearrange to yield

$$PP(T, \omega_t) \propto Re\left(\omega_t E_{pr}(\omega_t) S^{(3)}\left(\tau = 0, T, \omega_t\right)\right) \tag{4.2}$$

To extend this result to the rephasing spectrum we consider the time-apodized, third-order, nonlinear signal, $\theta(\tau)S^{(3)}(\tau, T, \omega_t)$, where $\theta(\tau)$ is a Heaviside function. After applying the projection-slice theorem to the 2D spectrum of the rephasing signal, we arrive at

$$\theta(0) Re\left(\omega_t E_{pr}(\omega_t) S^{(3)}\left(\tau = 0, T, \omega_t\right)\right) \tag{4.3}$$

Because $\theta(0) = 1$, expression 4.3 reduces to the $PP(T, \omega_t)$ signal, from Eq. 4.2. The projection of the signal in the rephasing direction, therefore, equals the spectrally resolved pump-probe signal and can be individually phased. A similar argument can be made for signal in the non-rephasing direction $\tau \leqslant 0$ simply by apodizing with $\theta(-\tau)$.

This proof holds in both the impulsive and non-impulsive regimes. For perfectly time-ordered interactions in the impulsive limit, the signal in the rephasing direction has contributions only from rephasing Liouville pathways, except for $\tau = 0$ when the rephasing signal has equal contributions from rephasing and non-rephasing Liouville pathways. Application of the projection-slice theorem to the two-dimensional rephasing signal yields the rephasing slice for $\tau = 0$, which is the same as the pump-probe signal.

In the non-impulsive regime, the signal in the rephasing direction has contributions from

non-rephasing Liouville pathways when pulses overlap (see Figure 4.6 in the appendix). The pump-probe signal acquired using the same pulse bandwidth similarly has contributions from rephasing and non-rephasing Liouville pathways. Thus, it is not intuitive in the non-impulsive limit that the projection of the rephasing signal on the $\omega_\tau = 0$ axis will equal the pump-probe signal. We therefore employ a simulation using pulses of finite duration to demonstrate that signals in the rephasing and non-rephasing directions can indeed be phased independently.

Theoretical calculations of third-order, nonlinear signal, as outlined by Brixner et al.,[10] were performed to simulate IR-144 with 30 fs transform-limited pulses centered at 802 nm. System parameters for diffusive dynamics were taken from Joo et al.[17] For inertial dynamics, a time constant and coupling strength of 200 fs and 200 cm1, respectively, were chosen. The signal for zero coherence time was used as the pump-probe signal. In Figure 4.1, we compare

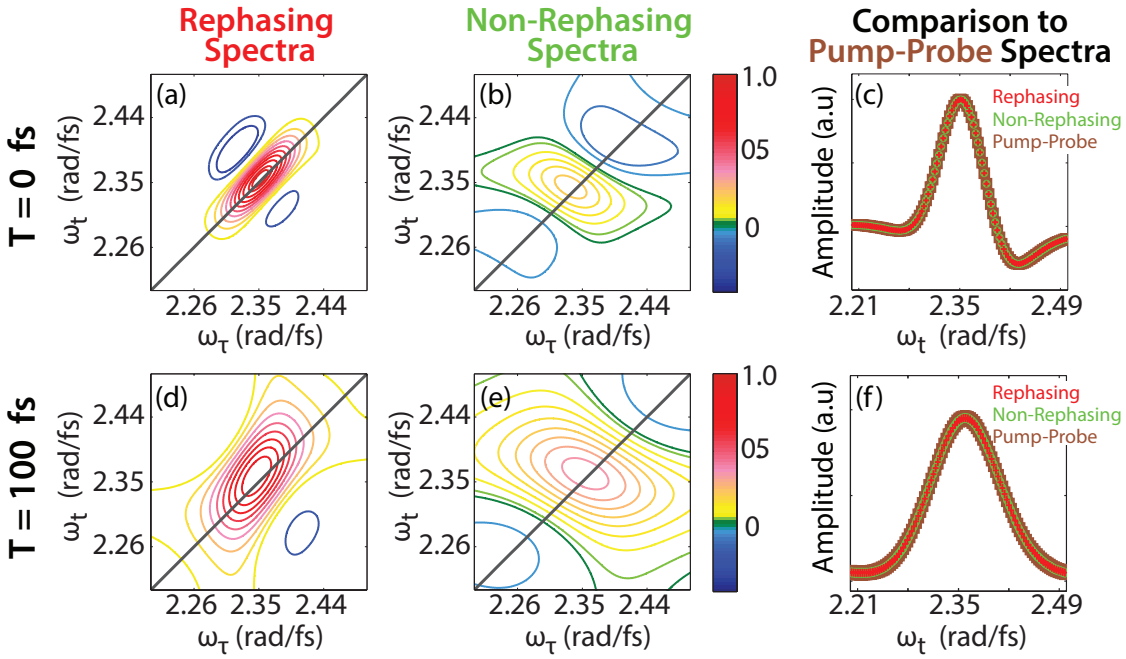

Figure 4.1: Comparison of simulated 2D data to pump probe spectra. Top row: (a) rephasing, (b) non-rephasing, and (c) comparison of projections of rephasing (red +) and non-rephasing (green circles) signals to pump-probe signal (brown square) for T = 0 fs. Bottom row: (d) rephasing, (e) non-rephasing, and (f) comparison of projections of rephasing (red +) and non-rephasing (green circles) signals to pump-probe signal (brown squares) for T = 100 fs.

the projections of a priori phased signals in the rephasing and non-rephasing directions and find that they are equal to pump-probe signal and to each other, as implied by the proof above. The top row of Figure 4.1 shows, in order, rephasing, non-rephasing, and comparison of projections of the rephasing and the non-rephasing spectra to pump-probe signal for T = 0 fs. The bottom row shows the corresponding spectra for T = 100 fs. The projections of rephasing and non-rephasing spectra are shown in red + and green circles, respectively, and are found to be equal to pump-probe spectrum (brown squares) as expected.

The purpose of phasing 2D spectra using spectrally resolved pump-probe signals is to correctly identify the absorptive and dispersive components of the susceptibility tensor in the frequency domain. Correct identification of absorptive and dispersive components can also be achieved in time domain by time-resolved heterodyne detection of transient grating (TG) signal.[18] In this method, the time dependence of absorptive and dispersive components can be obtained by systematically varying the phase between the TG signal and the LO, resulting in complete characterization of absorptive and dispersive components. A variant of this approach has recently been applied to phasing of 2D electronic spectra by Hauer and co-workers.[19]

4.3 Experimental Methods

GRAPES has been employed to acquire rephasing signal in the $-\vec{k}_1+\vec{k}_2+\vec{k}_3$ direction, where $\vec{k}_1$, $\vec{k}_2$ and $\vec{k}_3$ are the wave vectors of the three excitation pulses $1-3$, respectively.[13;14] The geometry for acquiring rephasing signal has been discussed in detail previously.[13;14] Briefly, a Coherent Micra Ti:sapphire oscillator seeds a Coherent Legend Elite USP-HE regenerative amplifier to generate 30 fs, transform-limited pulses centered at 805 nm (30 nm FWHM) with a 5 kHz repetition rate. A 50:50 beam splitter splits the output of the regenerative amplifier. One of the beams is incident on a retroreflector mounted to a motorized translational stage to generate the waiting time T. The other beam is incident on a stationary retroreflector, appropriately adjusted to compensate for distance. Both beams then reflect off the front

and back surfaces of a coated 3 mm, 3° wedged optic ($R1 = 40\%, R2 = 60\%$). The first four reflections generate excitation pulses 13 and the LO 4 in the rephasing direction as shown in Figure 4.2(a). We additionally use another internal reflection to create beam $4'$ for the non-rephasing local oscillator (Figure 4.2(a)). Beams 2 and 3 travel through 6 mm of glass in the wedged optic, which is taken into account by compensating beam 1 with 6 mm fused silica placed in its path. The coatings ensure that the three excitation pulses have similar power. The beams are directed toward the sample by the GRAPES mirror assembly (Figures 4.2(c) and 4.2(d)) in boxcars and distorted boxcars geometries to acquire signals in the non-rephasing and rephasing directions, respectively (Figure 4.2(b)). The beams are focused to a 6 mm line at the sample using a 250 mm focal length cylindrical lens. The emitted signal is focused into a $15\mu m$ slit using a pair of 25 cm and 50 cm focal length concave mirrors. The signal is spectrally resolved using a 600 lines/mm diffraction grating and imaged onto a $2048x2048$ thermally cooled CCD array (Andor). The rephasing and non-rephasing signals were acquired separately. Figures 4.3(a) and 4.3(b) compare the raw, heterodyned rephasing and non-rephasing signal imaged on the camera for zero waiting time. The colorbar indicates the counts generated on the CCD camera. As expected, the rephasing and non-rephasing signals are of similar intensity for zero waiting time. The fringe contrast of the signal-LO interferogram was optimized by varying the power of LO using a variable metallic neutral density filter introduced in the path of the LO. Timing between pulses was determined using spectral interferometry as described by Lepetit.[20] The precise location of $T = 0$ is important for our phasing approach. A detailed description of how pulse timings are determined in GRAPES has been given by Harel.[14]

Data processing of nonlinear, third-order 2D optical signals has been described in detail by Brixner et al.[10] An adaptation of the analysis for rephasing signals acquired using GRAPES has been described by Harel.[14] Non-rephasing spectra were processed by the same procedure.

With a pulse energy of 60 nJ/pulse, we achieve a fluence of 14 J/cm2, which is comparable to the fluence used in conventional 2D experiments.[21] Only a small fraction of the beam,

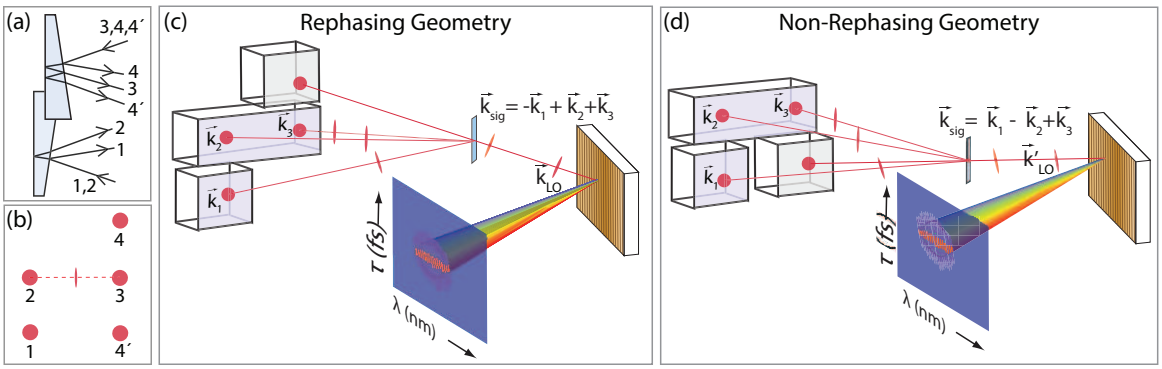

Figure 4.2: Optical apparatus to acquire rephasing and non-rephasing signals from GRAPES. (a) The wedged optic arrangement to produce all the required beams 1, 2, 3, 4, and 4. (b) Beams 1, 2, 3, and 4 form parallelogram boxcar geometry, while beams 1, 2, 3, and 4 form a boxcar geometry. The beams are focused at the center of the line joining 2 and 3. (c) GRAPES mirror assembly for acquiring rephasing signal. (d) Modified GRAPES mirror assembly for acquiring non-rephasing signal.

less than 1 mm, is required for data acquisition (see appendix for explanation). We assume constant power over 1 mm near the center of the Gaussian beam.

Pump-probe data, for phasing, was acquired using GRAPES apparatus as well. To acquire the pump-probe signal, beam 2 was used as pump and beam 3 was used as probe while other beams were blocked.[13;14] For all experiments, the sample consisted of a flowing solution of 0.3 M IR144 (O.D. = 0.22) in methanol in 200 μm thick fused silica flow cell (Starna).

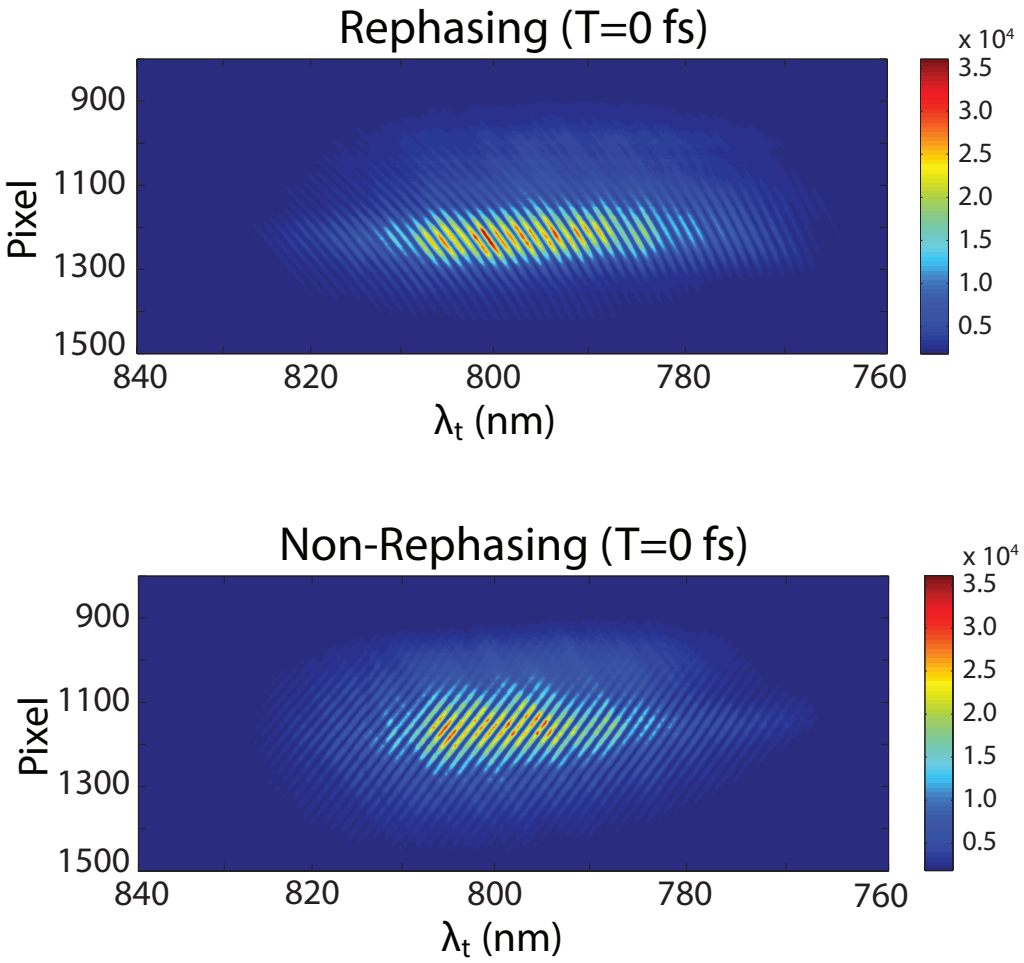

Figure 4.3: Raw heterodyned rephasing (a) and non-rephasing (b) signals for zero waiting time. The colorbar indicates the counts generated on the CCD camera.

4.4 Results and discussion

The complex 2D spectra acquired in the rephasing and non-rephasing directions was phased as shown

$$PP(T,\omega_t) \propto A \cdot Re\left[\int_{-\infty}^{+\infty} d\omega_\tau S^{(3)}(\omega_\tau, T, \omega_t) \times exp\left(i\phi_c + i(\omega_t - \omega_0)t_c + i(\omega_t - \omega_0)^2 t_d^2\right)\right]$$

where A is a normalization constant, ϕ_c is the constant phase, and $(\omega_t - \omega_0)$ is the rephasing frequency in the rotating frame of the field which oscillates at ω_0 center frequency. The term t_c corrects for uncertainty in the timing between the pulses 3 and LO, and the term t_d is a fitting parameter that corrects for the phase distortions in the LO resulting from variable metallic neutral density introduced in the path of LO to optimize fringe contrast of the signal-LO interferogram on the camera.[22] Independently phased signals in the rephasing and non-rephasing directions, $-\vec{k}_1+\vec{k}_2+\vec{k}_3$ and $+\vec{k}_1-\vec{k}_2+\vec{k}_3$, respectively, are presented in Figure 4.4. In order, the top row of Figure 4.4 shows phased rephasing, non-rephasing, and comparison of the projections of both to pump-probe signal for $T = 0$ fs. The bottom row shows these same spectra for $T = 100$ fs. For early waiting times ($T = 0$ fs) absorption and emission frequencies are correlated, resulting in diagonally elongated peaks (Figures 4.4(a) and 4.4(b)). After the waiting time increases to $T = 100$ fs, absorption and emission frequencies lose correlation due to solvent dynamics, resulting in more rounded peaks (Figures 4.4(d) and 4.4(e)).

The diagonal, positive feature in Figure 4.4 results from stimulated emission and ground state bleach. In these rephasing and non-rephasing spectra, the negative, off-diagonal features result primarily from dispersive contributions and are a concomitant outcome of Fourier transforming the signal over two time domains.[23;24] The frequency-resolved pump-probe signal is superimposed with probe-scatter interference. The interference is more prominent at shorter waiting times than longer waiting times. Due to these additional effects at early times, the signals fit better to their corresponding pump-probe spectra for $T = 100$ fs than for $T = 0$ fs, as shown in Figures 4.4(c) and 4.4(f). The projections of the signals compare

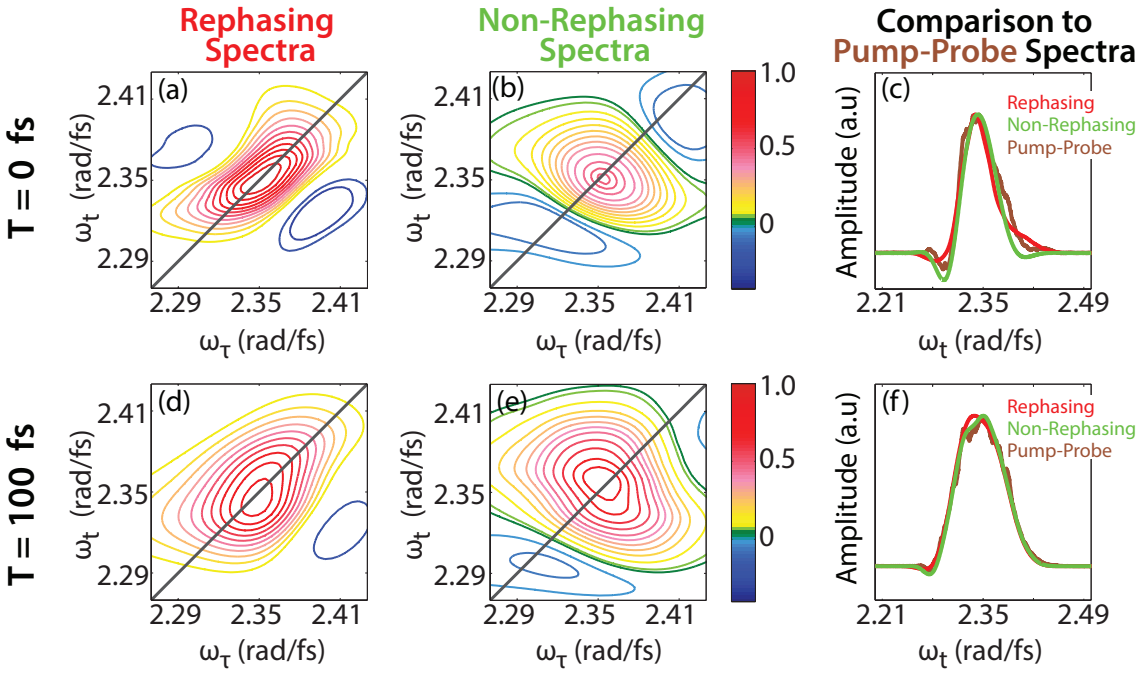

Figure 4.4: Comparison of experimental 2D rephasing and non-rephasing spectra to pump probe data. Top row: (a) rephasing signal, (b) non-rephasing signal, and (c) projection of rephasing signal (red) and non-rephasing signal (green) to pump-probe signal (brown) for T = 0 fs. Bottom row: (d) rephasing signal, (e) non-rephasing signal, and (f) projection of rephasing signal (red) and non-rephasing signal (green) to pump-probe signal (brown) for T = 100 fs.

better for $T = 100$ fs than for $T = 0$ fs.

The scaling factor and the phase parameters from Eq. 4.4, obtained after individually phasing the signals in the rephasing and non-rephasing directions to the pump-probe signal, ensure that the signals are equal for zero coherence time, hence suitably normalizing the two signals for comparison. The purely absorptive spectrum (Figures 4.5(a) and 4.5(c)) is obtained by adding the phased rephasing and non-rephasing spectra. However, because the signals in the rephasing and the non-rephasing directions were phased individually to the pump-probe signal, the projection of the purely absorptive spectrum is twice the pump-probe signal. The purely absorptive spectrum was therefore divided by 2 to obtain the absorptive 2D spectra presented in Figures 4.5(a) and 4.5(c).

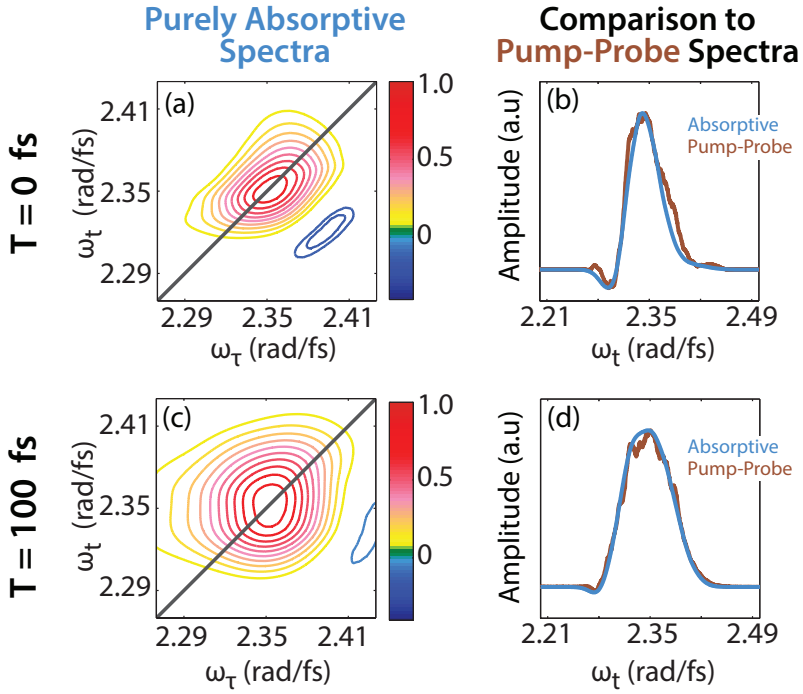

Figure 4.5: Comparison of purely absorptive GRAPES spectra to pump-probe data. Top row (T = 0 fs): (a) purely absorptive spectra and (b) comparison of the projection of the purely absorptive spectrum (blue) with pump-probe spectrum (brown). Bottom row (T = 100 fs): (c) purely absorptive spectra and (d) comparison of the projection of the purely absorptive spectrum (blue) with pump-probe spectrum (brown).

The projections of the purely absorptive spectrum (blue) to the pump-probe signal (brown) are compared in Figures 4.5(b) and 4.5(d). The diagonal feature on the purely

absorptive spectrum is elongated for early waiting times ($T = 0$ fs, Figure 4.5(a)) stemming from correlated absorption and signal emission frequencies. For longer waiting times, solvent dynamics cause the system to lose correlation between absorption and emission frequencies. This loss of memory results in a rounder diagonal feature for $T = 100$ fs (Figure 4.5(c)). The purely absorptive feature is free from phase twist, and the residual off diagonal negative features can be attributed to vibrational wave packet motion on the ground or excited electronic state as described by Gallagher Faeder and Jonas.[25]

4.5 Conclusion

We show that the signals in the rephasing and non-rephasing directions can be phased independently using frequency-resolved pump-probe spectra. Furthermore, GRAPES has been demonstrated to acquire signal in the non-rephasing direction. The signals in the rephasing and the non-rephasing directions, acquired using GRAPES, were phased independently resulting in the reconstruction of purely absorptive 2D spectra. Our results were found to be in good agreement with previous studies. This advance opens the possibility of mapping real time evolution of the Hamiltonian of systems that evolve during data acquisition.

4.6 Appendix

4.6.1 Pulse ordering in GRAPES

The figure below shows the pulse ordering in GRAPES. Figure 4.6(a) illustrates the time trace of pulses as they arrive at the sample. In contrast, figure 4.6(b) shows the time trace when the ordering of pulses 1 and 2 is swapped. Swapping the order of pulses 1 and 2 results in variable waiting time for a set of coherence time, as described by the time delay between pulse 3 and its immediately preceding pulse.

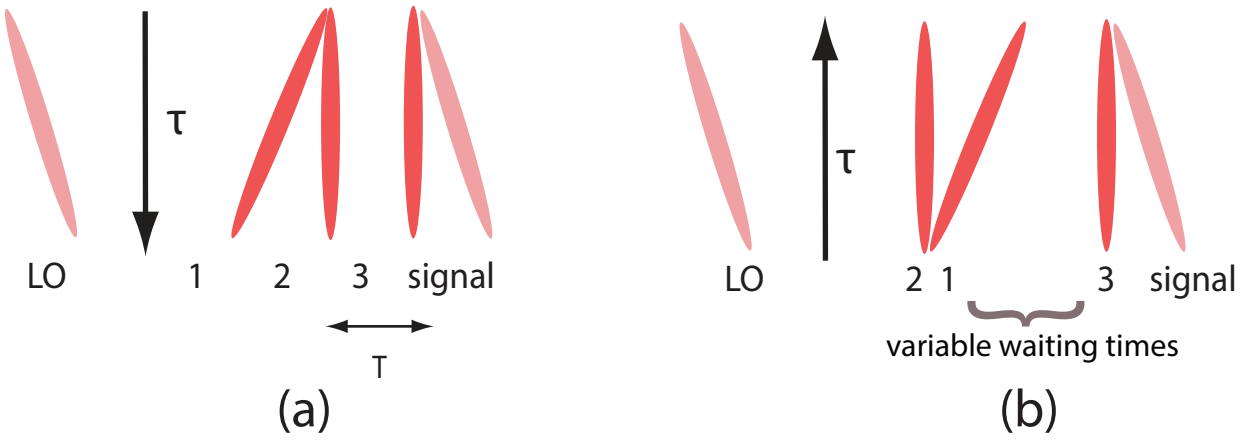

Figure 4.6: (a) Proper time ordering in GRAPES that samples all relevant coherence times for a given waiting time T. (b) Variable waiting time for a given set of coherence time generated upon swapping the order of pulses 1 and 2.

4.6.2 Contributions to rephasing signal for finite duration pulses

The rephasing signal has contributions from rephasing pathways for most coherence and waiting times. However for small coherence and waiting times non-rephasing pathways contribute to the rephasing signal as well, as shown below in figure 4.7. R_2 and R_3 are rephasing pathways, and R_1 and R_4 are non-rephasing pathways. The centers of the pulses are marked by dotted lines and labeled t_x (where x=1,2,3 for the three pulses) following Jonas convention. The interaction times are marked by bold lines and labeled τ_1, τ_2 and τ_3 for the first, second and third interactions, respectively. The pulse envelope is denoted by A_x. A product of A_x's shows the order in which the pulses interact. For example, $A_2A_1^*A_3$ means that the system interacts, in order, with pulses 2,1 and 3 characterized by directions $\vec{k}_2$, $-\vec{k}_1$ and $\vec{k}_3$, respectively, resulting in signal emission in the $-\vec{k}_1 + \vec{k}_2 + \vec{k}_3$ direction. For perfectly time-ordered interactions as shown in figure 4.7(a), only the rephasing pathways contribute to the rephasing signal through the interaction $A_1^*A_2A_3$. When pulses overlap, other possible interaction orderings can contribute to the rephasing signal through rephasing and non-rephasing pathways. For example, $A_1^*A_3A_2$ contributes through rephasing pathways as displayed in figure 4.7(c), while $A_2A_1^*A_3$ and $A_3A_1^*A_2$ contribute through non-rephasing pathways as shown in figure 4.7(b),(d).

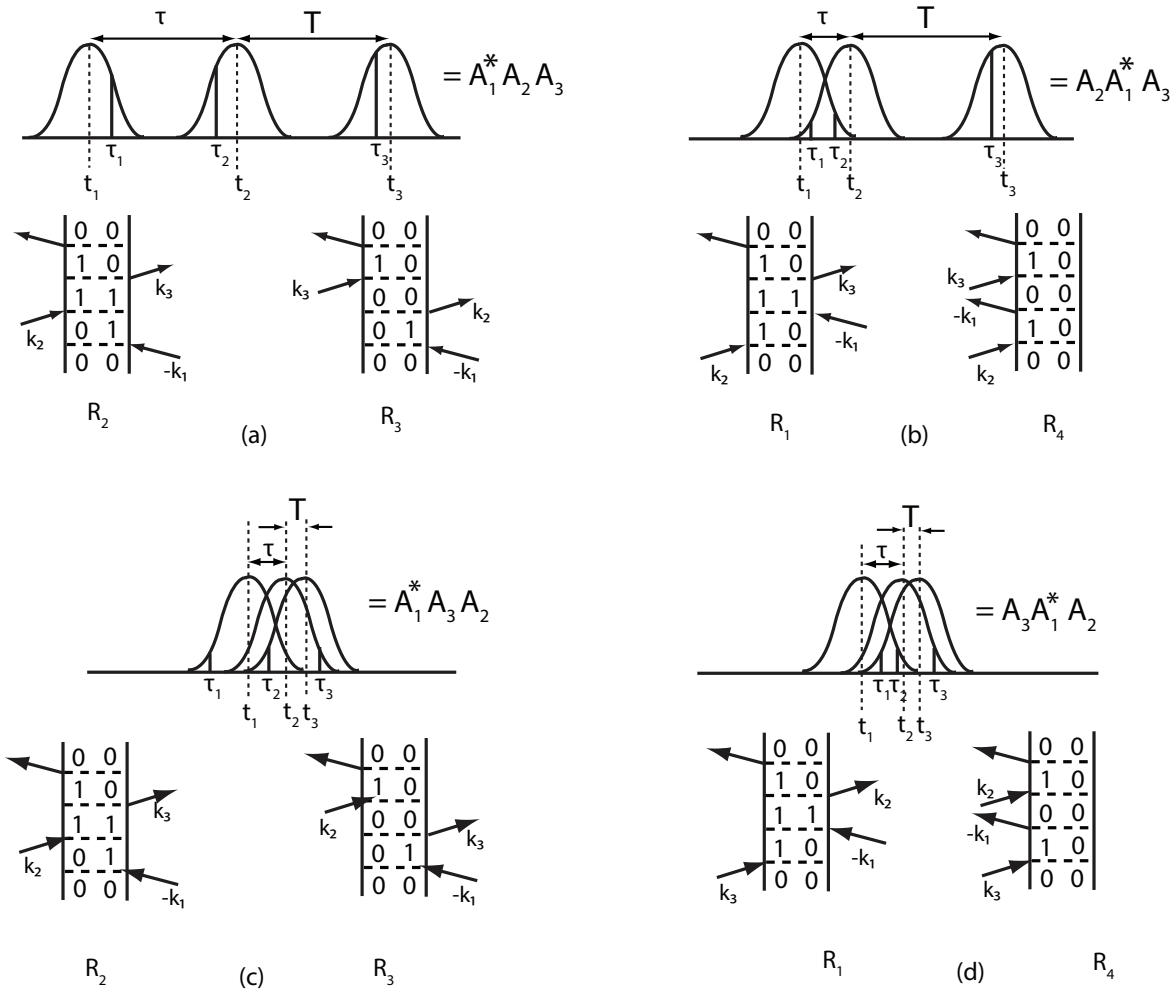

Figure 4.7: Contributions to rephasing signal in the $-\vec{k}_1 + \vec{k}_2 + \vec{k}_3$ direction for positive coherence time. Only R_2 and R_3 contribute from perfectly time ordered interactions as shown in (a). In addition to (a), when pulses overlap, non-rephasing pathways, R_1 and R_4 , contribute when pulse 2 interacts first followed by 1 and 3 (b), or when pulse 3 interacts first followed by 1 and 2 (d). Rephasing pathways can also contribute when interactions are not perfectly time ordered as in (c), where 1 interacts first followed by 3 and 2.

4.6.3 Power variations along the length of the beam

The emitted signal is spatially magnified by a factor of two by the use of 50 cm and 25 cm concave mirrors, and then focused into the camera. The gradient between beams 1 and 2 allows us to sample every 0.55 fs of coherence time, τ, per pixel in the vertical domain. Because most electronic coherences persist above the noise floor for not more than 70 fs during the coherence time, the signal can be imaged in less than 130 pixels on the camera. With a pixel size of 13.5 μm this corresponds to 1.8 mm on the camera or 0.9 mm on the sample. The power of beams is approximately constant over a length of 0.9 mm within the 6 mm beam.

4.6.4 Expanded Derivation of Equations in Theory section

Spectrally resolved pump-probe signal $PP(T, \omega_t)$ is related to the third order non-linear signal, $S^{(3)}(\omega_\tau, T, \omega_t)$, by the projection slice theorem

$$PP(T, \omega_t) \propto Re\left(\omega_t E_{pr}(\omega_t) \int_{-\infty}^{+\infty} d\omega_\tau S^{(3)}(\omega_\tau, T, \omega_t)\right) \tag{4.4}$$

Where $E_{pr}(\omega_t)$ is the probe field. $S^{(3)}(\omega_\tau, T, \omega_t)$ is acquired in the direction $-\vec{k}_1+\vec{k}_2+\vec{k}_3$ for positive and negative coherence times. Rewriting $S^{(3)}(\omega_\tau, T, \omega_t)$ as the Fourier transform over the τ domain yields equation 4.5

$$
\begin{aligned}
PP(T,\omega_t) &\propto Re\left(\omega_t E_{pr}(\omega_t)\int_{-\infty}^{+\infty} d\omega_\tau S^{(3)}\left(\omega_\tau,T,\omega_t\right)\right)\\
&= Re\left(\omega_t E_{pr}(\omega_t)\int_{-\infty}^{+\infty} d\omega_\tau \int_{-\infty}^{+\infty} d\tau S^{(3)}\left(\tau,T,\omega_t\right)e^{-i\omega_\tau\tau}\right)\\
&= Re\left(\omega_t E_{pr}(\omega_t)\int_{-\infty}^{+\infty} d\tau S^{(3)}\left(\tau,T,\omega_t\right)\underbrace{\int_{-\infty}^{+\infty} d\omega_\tau e^{-i\omega_\tau\tau}}_{\delta(\tau)}\right)\\
&= Re\left(\omega_t E_{pr}(\omega_t)\int_{-\infty}^{+\infty} d\tau S^{(3)}\left(\tau,T,\omega_t\right)\delta(\tau)\right)\\
&= Re\left(\omega_t E_{pr}(\omega_t)S^{(3)}\left(\tau=0,T,\omega_t\right)\right) \qquad (4.5)
\end{aligned}
$$

Applying projection slice theorem to the 2D spectrum of a time-apodized function, $\theta(\tau)S^{(3)}(\tau,T,\omega_t)$, where $\theta(\tau)$ is Heaviside function, and performing similar operations, yields equation 4.6

$$
\begin{aligned}
PP(T,\omega_t) &\propto Re\left(\omega_t E_{pr}(\omega_t)\int_{-\infty}^{+\infty} d\omega_\tau \int_{-\infty}^{+\infty} d\tau\theta(\tau) S^{(3)}\left(\tau,T,\omega_t\right)e^{-i\omega_\tau\tau}\right)\\
&= Re\left(\omega_t E_{pr}(\omega_t)\int_{-\infty}^{+\infty} d\tau\theta(\tau) S^{(3)}\left(\tau,T,\omega_t\right)\underbrace{\int_{-\infty}^{+\infty} d\omega_\tau e^{-i\omega_\tau\tau}}_{\delta(\tau)}\right)\\
&= Re\left(\omega_t E_{pr}(\omega_t)\int_{-\infty}^{+\infty} d\tau\theta(\tau) S^{(3)}\left(\tau,T,\omega_t\right)\delta(\tau)\right)\\
&= \theta(0)Re\left(\omega_t E_{pr}(\omega_t)S^{(3)}\left(\tau=0,T,\omega_t\right)\right) \qquad (4.6)
\end{aligned}
$$

Because $\theta(\tau)$ is a Heaviside function, i.e. $\theta(\tau)=1$ for $\tau\geq 1$ and $\theta(\tau)=0$ for $\tau<1$, from equation 4.5 the equation 4.6 above reduces to pump-probe signal. Also, $\theta(\tau)S^{(3)}(\tau,T,\omega_t)$ can be interpreted as the rephasing signal from the point by point data acquisition technique. Hence, rephasing signal can be individually phased to the pump-probe signal. This argument

can be equivalently extended for non-rephasing signal.

4.7 References

[1] Stone, K. W., Gundogdu, K., Turner, D. B., Li, X., Cundiff, S. T., and Nelson, K. A. (2009) Two-Quantum 2D FT Electronic Spectroscopy of Biexcitons in GaAs Quantum Wells. *Science 324*, 1169–1173.

[2] Griffin, G. B., Ithurria, S., Dolzhnikov, D. S., Linkin, A., Talapin, D. V., and Engel, G. S. (2013) Two-dimensional electronic spectroscopy of CdSe nanoparticles at very low pulse power. *The Journal of Chemical Physics 138*, 014705–11.

[3] Nemeth, A., Milota, F., Sperling, J., Abramavicius, D., Mukamel, S., and Kauffmann, H. F. (2009) Tracing exciton dynamics in molecular nanotubes with 2D electronic spectroscopy. *Chemical Physics Letters 469*, 130–134.

[4] Brixner, T., Stenger, J., Vaswani, H. M., Cho, M., Blankenship, R. E., and Fleming, G. R. (2005) Two-dimensional spectroscopy of electronic couplings in photosynthesis. *Nature 434*, 625–628.

[5] Engel, G. S., Calhoun, T. R., Read, E. L., Ahn, T. K., Mancal, T., Cheng, Y. C., Blankenship, R. E., and Fleming, G. R. (2007) Evidence for wavelike energy transfer through quantum coherence in photosynthetic systems. *Nature 446*, 782–786.

[6] Wong, C. Y., Alvey, R. M., Turner, D. B., Wilk, K. E., Bryant, D. A., Curmi, P. M. G., Silbey, R. J., and Scholes, G. D. (2012) Electronic coherence lineshapes reveal hidden excitonic correlations in photosynthetic light harvesting. *Nat Chem 4*, 396–404.

[7] Mukamel, S. *Principles of Nonlinear Optical Spectroscopy*; Oxford University Press: New York, 1995.

[8] Hybl, J. D., Ferro, A. A., and Jonas, D. M. (2001) Two-dimensional Fourier transform electronic spectroscopy. *The Journal of Chemical Physics 115*, 6606–6622.

[9] Cowan, M. L., Ogilvie, J. P., and Miller, R. J. D. (2004) Two-dimensional spectroscopy using diffractive optics based phased-locked photon echoes. *Chemical Physics Letters 386*, 184–189.

[10] Brixner, T., Mancal, T., Stiopkin, I. V., and Fleming, G. R. (2004) Phase-stabilized two-dimensional electronic spectroscopy. *The Journal of Chemical Physics 121*, 4221–4236.

[11] Cho, M., Vaswani, H. M., Brixner, T., Stenger, J., and Fleming, G. R. (2005) Exciton Analysis in 2D Electronic Spectroscopy. *The Journal of Physical Chemistry B 109*, 10542–10556.

[12] Hochstrasser, R. M. (2007) Two-dimensional spectroscopy at infrared and optical frequencies. *Proceedings of the National Academy of Sciences 104*, 14190–14196.

[13] Harel, E., Fidler, A. F., and Engel, G. S. (2010) Real-time mapping of electronic structure with single-shot two-dimensional electronic spectroscopy. *Proceedings of the National Academy of Sciences of the United States of America 107*, 16444–16447.

[14] Harel, E., Fidler, A. F., and Engel, G. S. (2010) Single-Shot Gradient-Assisted Photon Echo Electronic Spectroscopy. *The Journal of Physical Chemistry A 115*, 3787–3796.

[15] Jonas, D. M. (2003) TWO-DIMENSIONAL FEMTOSECOND SPECTROSCOPY. *Annual Review of Physical Chemistry 54*, 425–463.

[16] Bracewell, R. *The Fourier Transform and Its Applications*; McGraw-Hill Higher Education, 2000.

[17] Joo, T., Jia, Y., Yu, J.-Y., Lang, M. J., and Fleming, G. R. (1996) Third-order nonlinear

time domain probes of solvation dynamics. *The Journal of Chemical Physics 104*, 6089–6108.

[18] Goodno, G. D., Dadusc, G., and Miller, R. J. D. (1998) Ultrafast heterodyne-detected transient-grating spectroscopy using diffractive optics. *J. Opt. Soc. Am. B 15*, 1791–1794.

[19] Milota, F., Lincoln, C. N., and Hauer, J. (2013) Precise phasing of 2D-electronic spectra in a fully non-collinear phase-matching geometry. *Opt. Express 21*, 15904–15911.

[20] Lepetit, L., Chériaux, G., and Joffre, M. (1995) Linear techniques of phase measurement by femtosecond spectral interferometry for applications in spectroscopy. *J. Opt. Soc. Am. B 12*, 2467–2474.

[21] Panitchayangkoon, G., Hayes, D., Fransted, K. A., Caram, J. R., Harel, E., Wen, J., Blankenship, R. E., and Engel, G. S. (2010) Long-lived quantum coherence in photosynthetic complexes at physiological temperature. *Proceedings of the National Academy of Sciences 107*, 12766–12770.

[22] Albrecht, A. W., Hybl, J. D., Faeder, S. M. G., and Jonas, D. M. (1999) Experimental distinction between phase shifts and time delays: Implications for femtosecond spectroscopy and coherent control of chemical reactions. *The Journal of Chemical Physics 111*, 10934–10956.

[23] Ernst, R. R., Bodenhausen, G., and Wokaun, A. *Principles of Nuclear Magnetic Resonance in One and Two Dimensions*; Oxford University Press: Oxford, 1987.

[24] Khalil, M., Demirdven, N., and Tokmakoff, A. (2003) Obtaining Absorptive Line Shapes in Two-Dimensional Infrared Vibrational Correlation Spectra. *Physical Review Letters 90*, 047401.

[25] Gallagher Faeder, S. M., and Jonas, D. M. (1999) Two-Dimensional Electronic Correlation and Relaxation Spectra: Theory and Model Calculations. *The Journal of Physical Chemistry A 103*, 10489–10505.

CHAPTER 5

QUANTIFYING COHERENCE IN PHOTOSYNTHETIC ANTENNA COMPLEXES

5.1 Introduction

The remarkable quantum efficiency of energy transfer from light harvesting antenna complex to the reaction center (RC) has attracted immense experimental and theoretical studies.[1–4] While incoherent (or hopping) dynamics has been found to be the dominant mechanism of energy transfer, it is not the only mechanism.[5] Coherent dynamics involves ballistic energy flow between sites. It has been suggested that energy transfer is characterized by interplay of the two regimes.[5;6] The microscopic distinction between the regimes arises from how the bath interacts with the electronic states. While four-wave mixing experiments had been employed to understand coherent and incoherent nuclear motion and energy transfer dynamics in biological systems,[7;8] the development of two-dimensional electronic spectroscopy (2DES) has facilitated detailed analysis of four-wave mixing signals by resolving absorption and emission frequencies.[9–17] Recent observations of long lived coherences in FMO and reaction center were attributed to electronic states,[8;15] and it was hypothesized that the protein scaffold of the antenna complex protects coherences, through correlated bath fluctuation, to enhance the quantum efficiency in energy transfer.[16] Theoretical works by Aspuru-Guzik et al.[18] and Plenio and Huelga[19] support the claim that electronic coherences can indeed enhance quantum efficiency in energy transfer. These theories involve electronic states coupled weakly to a vibrational bath. However, alternative interpretations, that coherences induced by laser excitation are vibronic in nature, comply with experimental findings as well.[20–22] These theories take some vibrational modes out of the bath and allow them to mix explicitly with the electronic states.[23] In this vibronic model, electronic coherences borrow coherence lifetime from vibrational coherences by mixing electronic and vibrational states of the chromophores that make up the photosynthetic complex. These models are palatable because

the vibronic model considers Franck-Condon allowed vibrational states of the chromophores and does away with the hypothesis of correlated bath fluctuations, invoked to explain long-lived electronic coherences. In this manuscript, we present experimental results that directly characterize the nature of coherences in a mutant of LH2 (R26.1 LH2) from Rhodobacter (Rb.) sphaeriodes, which does not have B800 chromophores.[24] We also present a minimal theoretical model to estimate the extent of vibronic coupling and characterize the coherences between the two limiting cases of vibrational coherence and electronic coherence. We find the coherences to have some vibronic character, but a rather small mixing angle of about $13° - 17°$.

5.2 Experiment

The strength of the signal in a 2DES experiment depends on the strength of the four system-field interactions, each given by $-\vec{\mu}\cdot\vec{E}$ where $\vec{\mu}$ is the transition dipole moment of the system under study and $\vec{E}$ is the electric field strength of the excitation pulse. The direction of $\vec{E}$ is determined by the polarization of the excitation pulse. Because the pulses polarizations are experimentally controlled, the relative angle between the four transition dipoles directly governs the signal amplitude.[25] The signals amplitude dependence on the polarization of the electric fields has been used to determine peptide structure in proteins by determining the angle between transition dipoles, resolve 2D spectra, and study coherent dynamics in LH2.[26–30] In this experiment, we select a pulse polarization scheme to distinguish between electronic and vibrational coherence which are characterized by different angles between the transition dipoles that give rise to the coherence signal.

5.2.1 Optical apparatus

The details of our GRAPES optical apparatus are described elsewhere.[31;32] Briefly, a Coherent Micra Ti:sapphire oscillator seeds a Coherent Legend Elite USP-HE regenerative

amplifier to generate 30 fs, transform-limited pulses centered at 805 nm (30 nm FWHM) with a 5 kHz repetition rate. Additional bandwidth is achieved by focusing the pulse in argon gas (2 psi) to generate 90 nm FWHM pulse with 0.5% power stability (10 Hz measurement, 15 min duration). A 50:50 beam splitter and two wedged optics are used to create four pulses that are focused to a line in a homogeneous, flowing sample. The pulse is compressed at the sample using the multiphoton intrapulse interference phase scan method (Biophotonics Solution, Inc.) to get 15 fs pulses.[33] The resulting fluence is 14 $\mu J/cm^2$ per pulse. The optical density (OD) of R26.1 measured in a 1 mm Starna cell is 1.4 at 850 nm (see supplementary material). The R26.1 LH2 sample is placed in a 200 m Starna cell, and 2DES experiments are performed with canonical 2D and coherence-specific polarization sequences. The planes of pulse-polarizations are altered using half wave plates (ThorLabs), and calibrated using a Glan-Thompson polarizer (attenuation factor 10^5). First, the plane of polarization of beam 4 was determined using a Glan-Thompson polarizer. To calibrate the polarization to beam 1, the polarizer was turned by $45^\circ \pm 0.5^\circ$ (the error set by the least count on the dial of the polarizers mount) and the half-wave plate in the path of beam 1 was turned to achieve an attenuation of 10^5, thus, effectively calibrating beam 1 to $45^\circ \pm 0.5^\circ$ with respect to beam 4. Similar procedures were followed to characterize pulses 2 and 3, thus, enabling us to achieve the polarization states $45^\circ \pm 0.5^\circ$, $-45^\circ \pm 0.5^\circ$, $90^\circ \pm 0.5^\circ$, and 0° for beams 1, 2, 3, and 4. To verify polarizations and check for any ellipticity, we confirm the absence of a measurable interferogram from perpendicularly polarized pulses (e.g., beam 3-4 pair) in a thermally cooled CCD camera (Andor Instruments).

5.2.2 Sample Preparation

The sample preparation was, as far as practically possible, carried out in the dark. Approximately 5 g of pelleted R26.1 cells were suspended in 30 ml of 20 mM Tris.Cl pH 8.0 and a few grains of $MgCl_2$ and DNase were added to degrade the released DNA during cellular disruption. The sample was homogenised and passed three times through a French Press cell

(at 15000 psi) to ensure complete disruption. The resulting suspension was centrifuged at low-speed (Sorvall SS-34 rotor) at 3000 x g for 10 min at $4°C$. The pellet was discarded and the supernatant further centrifuged (Beckman Ti70 rotor) at 180000 x g for 2 h at $4°C$. The chromatophore pellet was resuspended in 20 mM Tris.Cl pH 8.0 at the NIR maximum to an OD of 50 cm^{-1}. The membranes were then solubilised by adding 4% decylmaltoside (DM) (w/v) and the sample stirred for 60 min at room temperature in the dark. The sample was then centrifuged for 30 min at 27000 x g (Sorvall SS-34 rotor) to remove denatured protein and any non-solubilised material. The supernatant was then loaded onto a discontinuous sucrose gradient using 0.2 M steps from 1.8 to 1.0 M sucrose, 0.15% DM, 20 mM Tris.Cl pH 8.0 and centrifuged (Beckman Ti70 rotor) 150000 x g for 14 h at $4°C$. This gradient effectively separates the LH2 complex from the LH1-RC. The sucrose solution band containing the LH2 complex was carefully removed from each tube and pooled. The LH2 complex was then purified further by anion exchange chromatography using DE52 resin (Whatman Scientific) and then by size exclusion chromatography on a Superdex-200 (GE Healthcare) column. LH2 fractions were collected, assayed, the best fractions pooled. The LH2 was concentrated and flash-frozen in suitable aliquots until required.

5.3 Results

We present results from 2DES studies of a mutant of LH2 (R26.1 LH2) from Rb. sphaeriodes, that does not have B800 chromophores, using two pulse polarization schemes. The first is the canonical polarization sequence routinely used in 2DES experiments. In this pulse polarization sequence, all the pulses have the same (parallel) linear polarization. The second pulse polarization sequence is the coherence-specific polarization sequence in which the first, second, and third pulse make $+45°$, $-45°$, and $+90°$ with respect to the local oscillator (LO). Here, "+" and "-" refer to clockwise and anti-clockwise direction when looking in the direction of pulse propagation.

5.3.1 Incoherent dynamics

Figure 5.1 (top row) shows the 2D spectra of rephasing signal from R26.1 LH2 acquired at room temperature using the canonical 2D polarization sequence. The spectra are for T = 50, 150, 250, 350, 450, and 550 fs. The coherence frequency, λ_τ, can be interpreted as absorption frequency and the rephasing frequency, λ_t, can be interpreted as emission frequency. The intensity of the diagonal peaks represents populations. In Figure 5.2(a), the diagonal peak centered at $\lambda_\tau = 780$ nm and $\lambda_t = 780$ nm, marked in the white box, represents the population of B850* states. In Figure 5.2(b), we show the B850* peak on a different colormap. Off-diagonal peaks arise from energy transfer between the two bands. The intensity of the lower off-diagonal peak increases with waiting time due to energy transfer from B850* states to B850 states. However, the intensity of the lower off-diagonal starts to decrease after 150 fs. The decrease in strength of the lower off-diagonal feature can be attributed to out of band relaxation of B850 states to its fluorescence state, and localization of exciton in the B850 ring (see supplementary material for more details). The exciton dynamics of B850* states is obtained by observing the trace of the diagonal feature at 780 nm as it evolves in waiting time T. In Figure 5.2(c), we show the trace of B850* states (grey) averaged over λ_τ = [775, 785] and λ_t = [775, 785]. The trace was fit to a single exponential decay (black) and gave population relaxation time constant of about 160$\pm$30 fs for the B850* states. The fast B850* to B850 energy transfer time scale is consistent with the prediction made by Novoderezhkin et al. for Rhodospirillum molischianum, which has exciton structure similar to LH2 of Rb. sphaeriodes.[34]

5.3.2 Coherent dynamics

Coherent dynamics of the R26.1 LH2 is studied by employing canonical and coherence-specific pulse polarization sequences. The 2D spectrum of the rephasing signal of R26.1 LH2 acquired with coherence-specific sequence is shown in the bottom row of Figure 5.1 for waiting times T = 50, 150, 250, 350, 450, and 550 fs. Results, concerning coherence signals, are

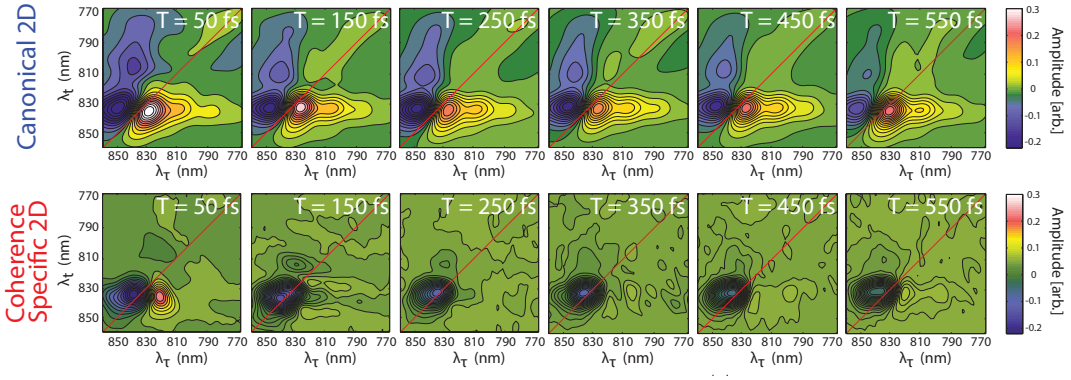

Figure 5.1: Two-dimensional spectra of rephasing signals acquired with the canonical 2D (top row) and coherence-specific (bottom row) polarization scheme for waiting times, T = 50, 150, 250, 350, 450, and 550 fs.

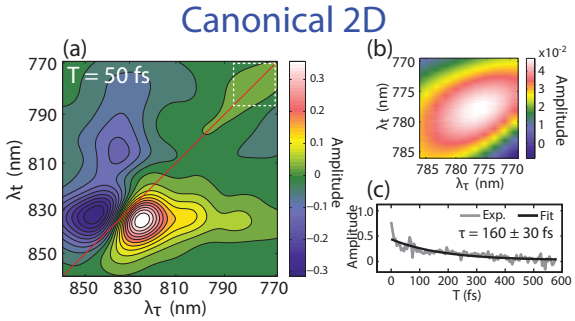

Figure 5.2: (a) 2D spectrum of rephasing signal acquired with canonical 2D polarization scheme at T = 50 fs. The B850* states appear in the section marked by white box. (b) The B850* diagonal peak, shown on a different color scheme. (c) The average trace of B850* population dynamics in the region $\lambda_\tau = [775, 785]$ and $\lambda_t = [775, 785]$ is shown in grey. The black trace is a mono-exponential fit the B850* population dynamics with a time constant of 160 fs.

summarized in Figures 5.3(a)(d). The top left panel (Figure 5.3(a)) shows the 2D spectrum of rephasing signal acquired at $T = 70$ fs using canonical 2D polarization sequence. We look at the evolution of points in the upper cross peak marked by the white box. The trace obtained by observing the evolution, in the waiting time T, of a particular point was fitted to a sum of a Gaussian (representing inertial terms) and an exponential (representing relaxation) decay. The fit was subtracted from the trace and the residue was fit to an exponentially decaying sinusoidal function to estimate coherence lifetime and coherence frequency. The average lifetime and frequency of coherences observed with canonical 2D polarization sequence is found to be 137±35 fs and 687±16cm^{-1}, respectively. Six representative coherence signals for points marked in yellow are shown alongside in Figure 5.3(b) in blue with the corresponding fits in black.

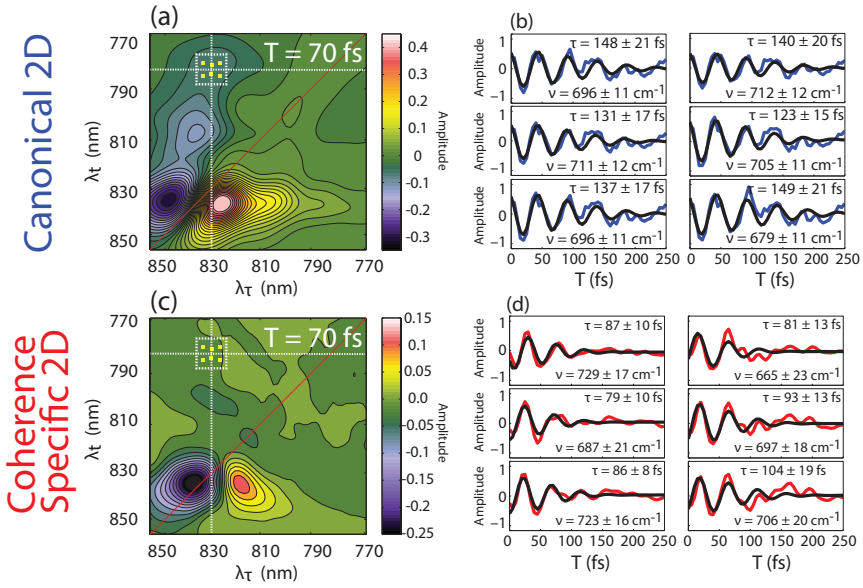

Figure 5.3: (a) 2D spectra of rephasing signal acquired with canonical 2D sequence at T = 70 fs. (b) Oscillatory features (blue) present in the traces of points marked in yellow in the upper cross peak of the 2D plot in (a). The fits to the oscillatory features are in black. (c) 2D spectra of rephasing signal acquired with coherence-specific sequence at T = 70 fs. (d) Oscillatory features (red) present in the traces of points marked in yellow in the upper cross peak of the 2D plot in (c). The fits to the oscillatory features are in black.

To investigate the nature of coherences, we employ the coherence-specific pulse polarization sequence. Results are summarized in Figures 5.3(c) and 5.3(d). The bottom left

panel (Figure 5.3(c)) shows the 2D spectrum of rephasing signal acquired at $T = 70$ fs using coherence-specific polarization sequence. The data acquired using the coherence-specific sequence are analyzed and interpreted in the same fashion as for the canonical 2D sequence. On the 2D spectrum, the diagonal feature corresponding to stimulated emission from B850* states does not show up, as expected for signals with parallel transition dipoles in coherence-specific experiments. The diagonal feature for B850 state at early waiting times corresponds to decoherence of $|k = +1\rangle \langle k = -1|$ state during positive waiting times. See supplementary material for more details on the nature of signals for positive and negative waiting times in the coherence-specific experiment. A coherence signal, visible in this dataset, is shown in red and the corresponding fits are shown in black. The average lifetime and oscillation frequency of the coherence signal is found to be 88 ± 8 fs and 695 ± 30 cm^{-1}. The frequency of this oscillation is similar to the average coherence frequency observed in the canonical 2D polarization, but the decay time differs markedly.

Within the Condon approximation, the angle between the transition dipoles, giving rise to vibrational coherence during the waiting time, is zero. Calculations have shown that a coherence signal with parallel transition dipoles will not survive the coherence-specific pulse polarization sequence.[25;28] In the case of purely vibrational coherence, no coherences should be observed with coherence-specific sequence. In the case of purely electronic coherence involving non-parallel transition dipoles, the observed coherence lifetime should be the same with both the pulse polarization sequences. The difference in lifetime of coherences observed with the two pulse polarization sequences excludes the possibility of the two limiting cases of purely electronic or purely vibrational coherence. Our data are consistent with a simple model of weak non-adiabatic coupling between dark vibrational states and higher excitonic states. This intermediate regime suggests coherences arise from mixed vibrational and electronic, or vibronic states. In Sec. 5.4, we present a simplified vibronic model to corroborate the hypothesis of vibronic coherence giving rise to different lifetimes when probed by canonical and coherence-specific pulse polarization sequence in a 2DES experiment. Alternatively,

the quantum beating observed in the canonical experiment could conceivably arise from a sum of purely vibrational and purely electronic coherence with nearly identical frequency, similar dephasing rate, and similar strength. We discount this hypothesis because it requires a vibrational coherence to dephase on a time scale much faster than population transfer or typical vibrational dephasing times.

5.4 Theoretical Model

A standard vibronic model is often adopted to study mixing of vibrational and electronic states to understand the nature of coherences in photosynthetic systems.[21–23;35;36] In the vibronic model, vibrational states are attributed to electronic potential energy surfaces of the individual BChlas solved within the Born-Oppenheimer (BO) approximation. Franck-Condon factor weighted Coulombic interactions between the electronic and vibrational states of the chromophores generate vibronic states of the entire photosynthetic complex.[35] Consequently, the exciton states of the photosynthetic complex in the vibronic model have mixed vibrational and electronic properties and are neither purely electronic nor purely vibrational in character. Such vibronic mixing frustrates examination of the two limiting cases: purely electronic coherence and purely vibrational coherence.

Here, we adopt an alternative, phenomenological approach to LH2 exciton structure to analyze coherences in the two limiting cases of purely electronic coherence and purely vibrational coherence. This formalism is similar in concept to that derived by Spano for excitons in molecular aggregates.[37] Contrasting with the approach pursued in vibronic model where vibrational states are attributed to electronic states of individual chromophores, we envisage the exciton structure where first the electronic potential energy surface of the entire photosynthetic complex is solved within the BO approximation and then decorated by vibrational (phonon) states. We refer to these states as BO exciton-states. The BO exciton-states do not couple to each other but rather couple to the bath which is responsible for system relaxation from one BO exciton-state to the other. However, accidental degeneracy or near degeneracy

between the BO exciton-states can lead to non-zero, non-adiabatic coupling between BO exciton states. We refer to the states resulting from non-adiabatic coupling between BO exciton-states as non-Born-Oppenheimer (NBO) exciton states. This coupling is identical in nature to a Fermi resonance between a combination band (exciton plus phonon) and a fundamental mode (exciton).[38]

The energy levels in our simplified model of R26.1 LH2 are shown in Figure 5.4(a). The yellow and the cyan potential energy surfaces are the B850 and B850* exciton states, respectively. Resonance Raman and surface enhanced resonance Raman studies of LH2 from Rb. sphaeriodes reveal vibrational modes with frequency similar to the gap between B850 and B850* states.[39] We posit that such a vibrational mode on the B850 state can interact with B850* states though non-adiabatic coupling and give rise to NBO exciton-states shown in green, though the resonance Raman data do not directly measure this quantity. The extent of non-adiabatic coupling governs coherence properties and, as we will show, gives accessible explanation to the difference in the coherence lifetime observed with canonical 2D and coherence-specific polarization sequence.

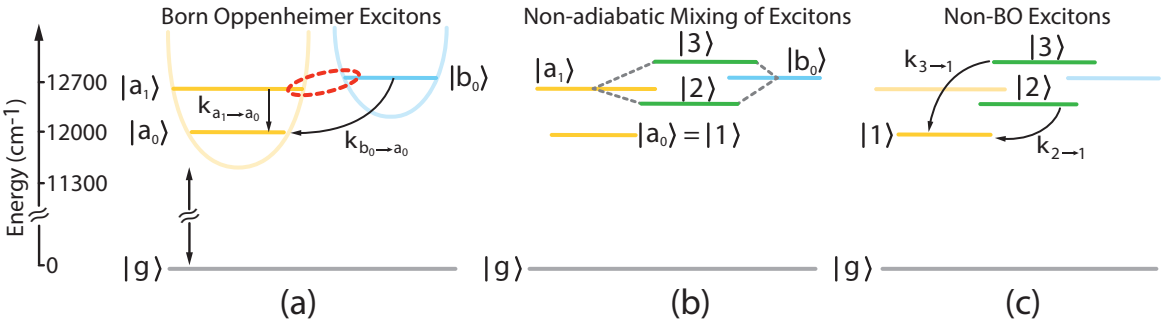

Figure 5.4: (a) The two different potential energy surfaces for B850 (yellow) and B850* (cyan) exciton states resulting from Born-Oppenheimer (BO) approximation. $|a_0\rangle$ and $|a_1\rangle$ are first harmonic and second harmonic of a vibrational mode on B850 states. $|b_0\rangle$ are the ground vibrational states on B850* states. Near degeneracy between $|a_1\rangle$ and $|b_0\rangle$ can result in non-adiabatic coupling of $|a_1\rangle$ and $|b_0\rangle$ (shown as red). (b) Non-adiabatic coupling mixes BO states $|a_1\rangle$ and $|b_0\rangle$ to give NBO states $|2\rangle$ and $|3\rangle$. (c) Non-adiabatic coupling alters transition rates $k_{a_1 \to a_0}$ and $k_{a_1 \to a_0}$ between BO states to give new transition rates $k_{2 \to 1}$ and $k_{3 \to 1}$ between NBO states.

We describe the effect of non-adiabatic coupling on BO states to give NBO states in

Figures 5.4(a)(c). BO exciton-states are represented by alphabets such as $|a_0\rangle$, and NBO exciton states are represented by numbers such as $|1\rangle$. For our purposes, B850 states are considered as one state; the lower potential energy surface shown in Figure 5.4(a) (yellow). $|a_0\rangle$ and $|a_1\rangle$ represent zero and one quanta of vibrational excitation on the B850 exciton state of R26.1 LH2. Similarly, B850* states are considered as one state; the higher energy exciton state shown in cyan (Figure 5.4(a)). $|b_0\rangle$ represents the ground vibrational state on B850* exciton state of R26.1 LH2. Given our laser bandwidth, we consider only the ground vibrational state on B850* state. The adiabatic approximation breaks when the energy states are close to each other as in the case of $|a_1\rangle$ and $|b_0\rangle$ (shown in red in Figure 5.4(a)).[40] The resulting non-adiabatic coupling mixes $|a_1\rangle$ and $|b_0\rangle$ to give $|2\rangle$ and $|3\rangle$, shown in green in Figure 5.4(b). The state $|a_0\rangle$ is unaffected by non-adiabatic coupling but, in the context of NBO states, $|a_0\rangle$ is referred to as $|1\rangle$.

The introduction of non-adiabatic coupling between BO states alters relaxation time scales within the system. Below, we present a method to calculate relaxation rates between NBO states that arise from non-adiabatic coupling induced mixing of BO states. The unitary transformation U mixes BO states $|a_1\rangle$ and $|b_0\rangle$ to give NBO states $|2\rangle$ and $|3\rangle$ as

$$|2\rangle = U_{a_1 2}\,|a_1\rangle + U_{b_0 2}\,|b_0\rangle \tag{5.1}$$

$$|3\rangle = U_{a_1 2}\,|a_1\rangle + U_{b_0 2}\,|b_0\rangle \tag{5.2}$$

In the absence of non-adiabatic coupling, transitions from $|a_1\rangle$ to $|a_0\rangle$ and from $|b_0\rangle$ to $|a_0\rangle$ take place at the rate $k_{a_1\to a_0}$ and $k_{b_0\to a_0}$, respectively (Figure 5.4(a)). The transition rate $k_{2\to 1}$ from state $|2\rangle$ to $|1\rangle$, and $k_{3\to 1}$ from state $|3\rangle$ to $|1\rangle$ after introducing the non-adiabatic coupling can be calculated as (see supplementary material for detailed derivation)

$$k_{2\to 1} = \left(U_{a_1 2}\right)^2 k_{a_1\to a_0}\left(1 - \frac{(\omega_{21}-\omega_{a_1 a_0})}{\omega_{a_1 a_0}}\right) + \left(U_{b_0 2}\right)^2 k_{b_0\to a_0}\left(1 - \frac{(\omega_{21}-\omega_{b_0 a_0})}{\omega_{b_0 a_0}}\right) \tag{5.3}$$

$$k_{3\to 1} = \left(U_{a_1 3}\right)^2 k_{a_1\to a_0}\left(1 - \frac{(\omega_{31}-\omega_{a_1 a_0})}{\omega_{a_1 a_0}}\right) + \left(U_{b_0 3}\right)^2 k_{b_0\to a_0}\left(1 - \frac{(\omega_{31}-\omega_{b_0 a_0})}{\omega_{b_0 a_0}}\right) \tag{5.4}$$

where $\omega_{a_1 a_0} = \omega_{a_1} - \omega_{a_0}$, etc. Similarly, the pure dephasing rates $k^{pd}_{a_1 a_0}$ and $k^{pd}_{b_0 a_0}$ between pairs of states $|a_1\rangle$ and $|a_0\rangle$, and between $|b_0\rangle$ and $|a_0\rangle$, respectively, can be calculated within the secular approximation to obtain the pure dephasing rates k^{pd}_{21} and k^{pd}_{31} between pairs of states $|2\rangle$ and $|1\rangle$, and between $|3\rangle$ and $|1\rangle$, respectively, as (see supplementary material)34

$$k^{pd}_{21} = \left(U_{a_1 2}\right)^2 k^{pd}_{a_1 a_0} + \left(U_{a_1 2}\right)^2 k^{pd}_{b_0 a_0} \tag{5.5}$$

$$k^{pd}_{31} = \left(U_{a_1 3}\right)^2 k^{pd}_{a_1 a_0} + \left(U_{a_1 3}\right)^2 k^{pd}_{b_0 a_0} \tag{5.6}$$

This reductionist approach has a number of advantages. First, for a system with many chromophores, such as R26.1 LH2, the complexity of exciton structure in the vibronic model compounds if vibrational states on the chromophores are included to study mixing of vibrational and electronic states. The approach presented above greatly simplifies calculations and makes the picture clearer. Second, the approach presented above has the advantage of incorporating non-adiabatic coupling in a simplified manner and distinguishes clearly between limits of purely vibrational coherence and purely electronic coherences.

Compared to the standard vibronic model, our model takes a fundamentally different approach to describe excitonic properties. The standard vibronic model takes a bottom-up approach to describe the coherence properties of photosynthetic complexes, while the approach of our model can be described as a top-down approach. In the standard vibronic model, properties of individual components of photosynthetic complexes, i.e., chromophores, are described in great detail. These properties include site energy, chromophore-bath coupling (Huang-Rhys factor), and vibrational frequencies with associated Franck-Condon factors. Starting with such a description, Coulombic interaction between chromophores results in the exciton structure. Our model does not elucidate such microscopic details, but rather considers phonons atop Born-Oppenheimer excitonic states.

In our model, vibrational mode $|a_1\rangle$ is added, not to the chromophores, but to the complexs exciton state $|a_0\rangle$, and made to interact with the $|b_0\rangle$ exciton state in a non-

adiabatic fashion. Such an addition to the electronic state can be justified on the basis of resonance Raman spectrum. The treatment of coherences in the model is analogous to the approach adopted to explain Fermi resonance where a vibrational overtone is taken into consideration only to explain the doublet.[41]

5.5 Discussion

Calculation of rate constants between NBO states from Eqs. 5.3,5.4,5.5,5.6 requires as input energies, detuning (Δ_1), non-adiabatic coupling (V_{NAC}), and relaxation rates among BO states. In addition, the orientation of transition dipoles of BO states is required for ultimately calculating the coherence signals. Given our bandwidth (see supplementary material) we can only excite the blue side of the B850 band. We therefore assign states $|a_0\rangle$ and $|b_0\rangle$ within our model to have energies of 12000 cm^{-1} and 12700 cm^{-1}, respectively. $k_{a_1 \to a_0}$ and $k_{a_1 \to a_0}$ being vibrational and electronic transition rates between BO exciton-states are assumed to be 1/2 ps^{-1} and 1/100 fs^{-1}, respectively. The pure dephasing rates $k^{pd}_{a_1 a_0}$ and $k^{pd}_{b_0 a_0}$ for the vibrational and electronic coherences are assumed to be 1/2 ps^{-1} and 1/100 fs^{-1}, respectively. In analogy to the observed difference in the average coherence frequencies between the canonical and coherence-specific 2D experiments, we set the energy difference between states $|2\rangle$ and $|3\rangle$, ΔE_{23}, to be 10 cm^{-1} in our model. The energy gap between states $|2\rangle$ and $|3\rangle$ results from mixing of the BO exciton-states $|a_1\rangle$ and $|b_0\rangle$ (see supplementary material). However, this gap alone is insufficient to describe the mixing because the mixing angle depends on two parameters: the detuning (Δ) and coupling (V_{NAC}) between $|a_1\rangle$ and $|b_0\rangle$. Here, we use the measurable difference in experimentally measured coherence lifetimes to constrain the mixing angle between the states. Ultimately, it is this difference in coherence lifetimes rather than the small difference in the experimentally observed coherence frequency that confirms mixing between vibrational and electronic states. The dipole strength $|\vec{\mu}_{a_0}|^2$ of state $|a_0\rangle$ is taken as the reference and set to one, i.e., $|\vec{\mu}_{a_0}|^2$=1. We estimate the dipole strength $|\vec{\mu}_{a_1}|^2$, of state $|a_1\rangle$, and $|\vec{\mu}_{b_0}|^2$, of state $|b_0\rangle$, to be 0.04 and 0.09, respectively.[39;42]

The pair of transition dipoles, $\vec{\mu}_{a_0}$ and $\vec{\mu}_{a_1}$, belong to the same potential energy surface and are parallel to each other within the Condon approximation. For simplicity, the direction of $\vec{\mu}_{b_0}$ is set at 45° with respect to $\vec{\mu}_{a_0}$ and $\vec{\mu}_{a_1}$ based on a symmetry of the ring-like structure of R26.1 LH2 (see supplementary material for explanation).

Using the input parameters specified above, we calculate the amplitude of the coherence signal with canonical 2D and coherence-specific pulse polarization sequence as described by Hochstrasser.[25] The calculated signal was analyzed in the same way as experimentally obtained coherence signals. In Figure 5.5(a), we show the coherence lifetime from the calculated coherence signals using canonical 2D (blue) and coherence-specific (red) pulse polarization sequence as a function of the mixing angle between the BO exciton states $|a_1\rangle$ and $|b_0\rangle$. The blue and the red stripes in Figure 5.5(a) are experimentally observed coherence lifetimes in the canonical and coherence-specific experiments, respectively. In Figures 5.5(b) and 5.5(c), we show the mixing between BO exciton states $|a_1\rangle$ and $|b_0\rangle$, and the calculated coherence signals with canonical and coherence-specific sequence for a particular case of mixing angle, $\theta_{mix} = 12.5°$. In Figure 5.5(b), the transition dipole vectors $\vec{\mu}_{a_0}$, $\vec{\mu}_{a_1}$, and $\vec{\mu}_{b_0}$ of BO states $|a_0\rangle$, $|a_1\rangle$, and $|b_0\rangle$ are shown in dashed yellow, solid yellow, and cyan, respectively. While $\vec{\mu}_{a_1}$ is parallel to $\vec{\mu}_{a_0}$, $\vec{\mu}_{b_0}$ makes a 45° angle with $\vec{\mu}_{a_0}$ as mentioned above. The non-adiabatic coupling between BO states mixes $\vec{\mu}_{a_1}$ and $\vec{\mu}_{b_0}$ to give $\vec{\mu}_2$ and $\vec{\mu}_3$, both of which are shown in green. $\vec{\mu}_{a_0}$ is unaffected by non-adiabatic coupling but, in the context of NBO states, is referred to as $\vec{\mu}_1$. The mixed states, $\vec{\mu}_2$ and $\vec{\mu}_3$, make an angle θ_{12} and θ_{13}, respectively, with respect to $\vec{\mu}_1$.

In our data and in our model, we observe different coherence lifetimes in the canonical and coherence-specific pulse polarization 2DES experiment. The observed oscillatory signal is a sum of two coherences: one from each pair ($|1\rangle$,$|2\rangle$) and ($|1\rangle$,$|3\rangle$). The lifetime of the observed signal is determined by the relative amplitudes, A_{12} and A_{13}, of the underlying coherences. To explain the relative contributions and lifetimes of these two coherences in each experiment, we start from a limit of zero non-adiabatic coupling and then introduce

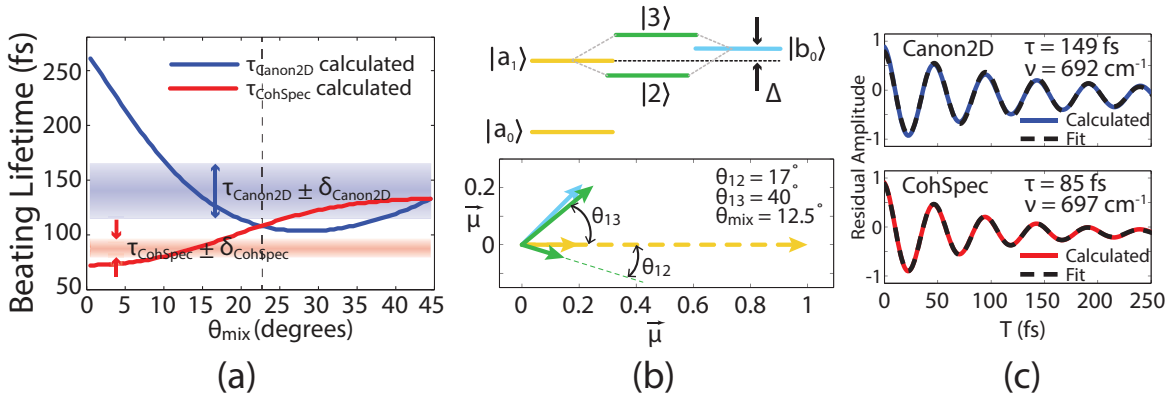

Figure 5.5: (a) The two different potential energy surfaces for B850 (yellow) and B850* (cyan) exciton states resulting from Born-Oppenheimer (BO) approximation. $|a_0\rangle$ and $|a_1\rangle$ are first harmonic and second harmonic of a vibrational mode on B850 states. $|b_0\rangle$ are the ground vibrational states on B850* states. Near degeneracy between $|a_1\rangle$ and $|b_0\rangle$ can result in non-adiabatic coupling of $|a_1\rangle$ and $|b_0\rangle$ (shown as red). (b) Non-adiabatic coupling mixes BO states $|a_1\rangle$ and $|b_0\rangle$ to give NBO states $|2\rangle$ and $|3\rangle$. (c) Non-adiabatic coupling alters transition rates $k_{a_1 \to a_0}$ and $k_{b_0 \to a_0}$ between BO states to give new transition rates $k_{2 \to 1}$ and $k_{3 \to 1}$ between NBO states.

non-adiabatic coupling to determine the window in which our model is consistent with our data. In the limiting case of no coupling, coherence from the pair ($(|1\rangle,|2\rangle)$) is purely vibrational and coherence from the pair ($(|1\rangle,|3\rangle)$) is purely electronic. We expect that the lifetime τ_{12} of the vibrational coherence is greater than the lifetime τ_{13} of the electronic coherence. Experimentally, we observe that coherence lifetime $\tau_{Canon2D}$ in the canonical 2D experiment is greater than the coherence lifetime $\tau_{CohSpec}$ in the coherence-specific experiment. Therefore, we argue that the amplitude of coherence from the pair ($(|1\rangle,|2\rangle)$), which in the limit of weak coupling represents a transition of primarily vibrational character, contributes more to the signal in the canonical 2D experiment than in the coherence-specific 2D experiment.

The relative strength of the contribution of a coherence signal to the coherence-specific experiment compared to the canonical 2D experiment is determined entirely by the angle between the transition dipole moments of the states involved in the coherence. The orientational prefactors vary between the different polarization-sequences depending on the angle between the transition dipoles in the molecular frame. From these orientation factors, we infer that the angle θ_{12} between the transition dipoles in the pair ($|1\rangle,|2\rangle$) is smaller than

the angle θ_{13} between the dipoles in the pair ($|1\rangle$,$|3\rangle$), i.e., $\theta_{12} < \theta_{13}$ (see supplementary material for further explanation). The inference $\theta_{12} < \theta_{13}$ helps us to deduce the extent of non-adiabatic coupling between the BO states $|a_1\rangle$ and $|b_0\rangle$. In the limiting case of absence of non-adiabatic coupling, the transition dipoles are identical to those of $|a_1\rangle$ and $|b_0\rangle$, namely, $\theta_{12} = 0^\circ(\theta_{a_0a_1})$ and $\theta_{13} = 45^\circ(\theta_{a_0b_0})$. As the non-adiabatic coupling increases, transition dipoles $\vec{\mu}_{a_0}$ and $\vec{\mu}_{a_1}$ mix to redistribute dipole strengths and give new transition dipoles $\vec{\mu}_2$ and $\vec{\mu}_3$. While $\vec{\mu}_2$ points away from $\vec{\mu}_1$ to make an angle $\theta_{12}(> 0^\circ)$ with respect to $\vec{\mu}_1$, $\vec{\mu}_3$ points in a direction closer to $\vec{\mu}_1$, to make an angle $\theta_{12}(< 45^\circ)$ with respect to $\vec{\mu}_1$. As an example, see Figure 5.5(b). As the strength of non-adiabatic coupling increases, θ_{12} increases while θ_{13} decreases. However, as deduced above, $\theta_{12} < \theta_{13}$ and this condition sets the upper bound to the strength of non-adiabatic coupling at θ_{mix} 22.5° (shown by the dotted vertical line in Figure 5.5(a)). Our model additionally provides the opportunity to directly compare extracted coherence lifetimes with experiment. We find that our data are consistent with our model only within the narrow range of mixing angles between 13° and 17° (Figure 5.5(a)).

5.6 Conclusion

We have directly observed the B850* to B850 transfer rate of 160 fs by employing the canonical 2D sequence on the LH2 mutant of the Rb. sphaeriodes, R26.1 LH2. The fast dynamics is consistent with the prediction by Novoderezhkin.[34] With the canonical 2D sequence, we observe coherences between B850* and B850 states that persist for 137 ± 35 fs. To understand the origin of coherences, we employed the coherence-specific pulse polarization sequence to suppress signals from states with parallel transition dipoles. With the coherence-specific sequence, we observe coherences with an average lifetime of 88 ± 8 fs; a noticeable reduction in lifetime. From these data, we deduce that the states involved in the coherence are vibronic states. We present a simplified theoretical approach to calculate relaxation rates between NBO states in terms of non-adiabatic coupling and relaxation between BO states.

Our calculations suggest weak to mild coupling between vibrational and electronic states and extract a mixing angle θ_{mix} fs between 13° and 17° between the vibrational and excitonic states within this model.

5.7 Appendix

5.7.1 Linear absorption spectrum of R26.1 LH2 and excitation laser spectrum

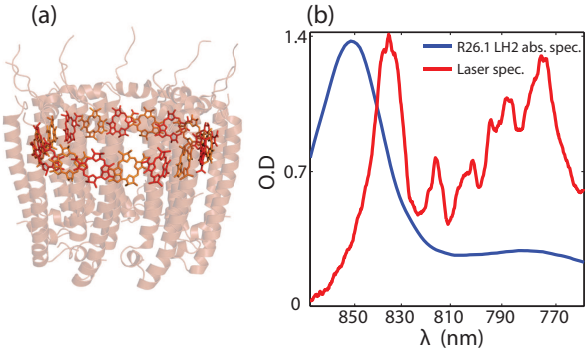

Figure 5.6: (a)Cartoon representation of just the B850 chromophores from LH2 of Rhodopseudomonas acidophila (PDB file 2FKW). The α and the β chromophores are shown in red and orange respectively.(b) Absorption spectrum of R26.1 LH2 at room temperature (blue) and the normalized spectrum of the excitation laser pulse (red).

5.7.2 Derivation of rate constants for NBO states

We first derive the relaxation rates of NBO excitons. The unitary transformation u mixes states $|a_1\rangle$ and $|b_0\rangle$ to give $|2\rangle$ and $|3\rangle$ as (figure 5.7)

$$u = \begin{bmatrix} U_{a_1 2} & U_{b_0 2} \\ U_{a_1 3} & U_{b_0 3} \end{bmatrix}$$

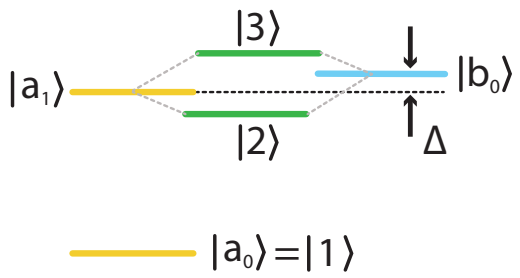

Figure 5.7: $|a_0\rangle$, $|a_1\rangle$ and $|b_0\rangle$ are Born-Oppenheimer (BO) states. $|a_1\rangle$ and $|b_0\rangle$ mix to give non-Born-Oppenheimer (NBO) states $|2\rangle$ and $|3\rangle$ shown in green.

Therefor the matrix U that transforms the of BO states $\{|a_0\rangle, |a_1\rangle, |b_0\rangle\}$ into the set of NBO states $\{|1\rangle, |2\rangle, |3\rangle\}$ is

$$U = \begin{bmatrix} 1 & 0 & 0 \\ 0 & U_{a_1 2} & U_{b_0 2} \\ 0 & U_{a_1 3} & U_{b_0 3} \end{bmatrix}$$

The states $|2\rangle$ and $|3\rangle$ can be written as

$$|2\rangle = U_{a_1 2}\,|a_1\rangle + U_{b_0 2}\,|b_0\rangle \tag{5.7}$$

$$|3\rangle = U_{a_1 2}\,|a_1\rangle + U_{b_0 2}\,|b_0\rangle \tag{5.8}$$

Rate of transition $k_{3\to 1}$ from the state $|3\rangle$ to the state $|1\rangle$ is given by

$$k_{3\to 1} = 2Re\left(\int_0^\infty dt H_{13}^{SB}(t) H_{13}^{SB}(0) exp(-i\omega_{31}t)\right) \tag{5.9}$$

where $\omega_{31} = \omega_3 - \omega_1$ and $H_{13}^{SB}(t)$ is the system bath coupling between the NBO excitons $|1\rangle$ and $|3\rangle$ at time t, etc. Using the unitary matrix U, the coupling element between NBO states $|1\rangle$ and $|3\rangle$ can be written in terms of coupling between BO excitons $|a_0\rangle, |a_1\rangle$ and

$|b_0\rangle$ as

$$\begin{aligned} H_{13}^{SB}(t)H_{13}^{SB}(0) &= (U_{a_13})^2 H_{a_0a_1}^{SB}(t)H_{a_1a_0}^{SB}(0) + (U_{b_03})^2 H_{a_0b_0}^{SB}(t)H_{b_0a_0}^{SB}(0) \\ & U_{a_13}U_{b_03}H_{a_0b_0}^{SB}(t)H_{a_1a_0}^{SB}(0) + U_{a_13}U_{b_03}H_{a_0a_1}^{SB}(t)H_{b_0a_0}^{SB}(0) \end{aligned} \quad (5.10)$$

From equation 5.9 and 5.10, we get

$$\begin{aligned} k_{3\to1} &= (U_{a_13})^2 \cdot 2Re\left(\int_0^\infty dt H_{a_0a_1}^{SB}(t)H_{a_1a_0}^{SB}(0)exp(-i\omega_{31}t)\right) \\ &+ (U_{b_03})^2 \cdot 2Re\left(\int_0^\infty dt H_{a_0b_0}^{SB}(t)H_{b_0a_0}^{SB}(0)exp(-i\omega_{31}t)\right) \\ &+ U_{a_13}U_{b_03} \cdot 2Re\left(\int_0^\infty dt H_{a_0b_0}^{SB}(t)H_{a_1a_0}^{SB}(0)exp(-i\omega_{31}t)\right) \\ &+ U_{a_13}U_{b_03} \cdot 2Re\left(\int_0^\infty dt H_{a_0a_1}^{SB}(t)H_{b_0a_0}^{SB}(0)exp(-i\omega_{31}t)\right) \end{aligned} \quad (5.11)$$

The last two terms on the right hand side of equation 5.11 above involve correlation in coupling between different pairs of BO states, e.g. $H_{a_0b_0}^{SB}(t)H_{a_1a_0}^{SB}(0)$ is the correlation in coupling between the pair of states $(|a_0\rangle, |b_0\rangle)$ and $(|a_0\rangle, |a_1\rangle)$. For simplicity we assume absence of correlation in coupling between different pair of excitons. This is equivalent to assume absence of correlation in energy fluctuation between two pair of excitons. This reduces relaxation rate to

$$\begin{aligned} k_{3\to1} &= (U_{a_13})^2 \cdot \underbrace{2Re\left(\int_0^\infty dt H_{a_0a_1}^{SB}(t)H_{a_1a_0}^{SB}(0)exp(-i\omega_{31}t)\right)}_{T_1} \\ &+ (U_{b_03})^2 \cdot \underbrace{2Re\left(\int_0^\infty dt H_{a_0b_0}^{SB}(t)H_{b_0a_0}^{SB}(0)exp(-i\omega_{31}t)\right)}_{T_2} \end{aligned} \quad (5.12)$$

Equation 5.12 above contains terms T_1 and T_2,each involving the Fourier transform with respect to the energy gap between states $|1\rangle$ and $|3\rangle$. We re-write, for example T_1, as follows

$$\begin{aligned} T_1 &= 2Re\left(\int_0^\infty dt H^{SB}_{a_0a_1}(t)H^{SB}_{a_1a_0}(0)exp(-i\omega_{31}t)\right) \\ &= 2Re\left(\int_0^\infty dt H^{SB}_{a_0a_1}(t)H^{SB}_{a_1a_0}(0)exp(-i\omega_{a_1a_0}t)exp(-i(\omega_{31}-\omega_{a_1a_0})t)\right) \end{aligned} \quad (5.13)$$

where $\omega_{a_1a_0} = \omega_{a_1} - \omega_{a_0}$. In the case of small detuning between BO states $|a_1\rangle$ and $|b_0\rangle$, the frequency difference $\omega_{31} - \omega_{a_1a_0}$ is small. Consequently we series expand $exp(-i(\omega_{31} - \omega_{a_1a_0})t)$, in equation 5.13 above, and retain only the linear term in $\omega_{31} - \omega_{a_1a_0}$, i.e.

$$exp(-i(\omega_{31} - \omega_{a_1a_0})t) \approx 1 - i(\omega_{31} - \omega_{a_1a_0})t$$

By definition of rate constants and properties of complex correlation functions,

$$\begin{aligned} k_{a_1\to a_0} &= 2Re\left(\int_0^\infty dt H^{SB}_{a_0a_1}(t)H^{SB}_{a_1a_0}(0)exp(-i\omega_{a_1a_0}t)\right) \\ &= (p.r)\cdot 2Re\left(\int_0^\infty dt C(t)exp(-i\omega_{a_1a_0}t)\right) \end{aligned} \quad (5.14)$$

where $p.r$ is the participation ratio and $C(t)$ is the system bath coupling given as

$$C(t) = \sum_j \omega_j^2 S_j[(n_j+1)exp(-i\omega_j t) + n_j exp(i\omega_j t)] \quad (5.15)$$

Here ω_j, S_j and n_j are the frequencies, Huang-Rhys factor and thermal occupation number for the j^{th} mode the system is coupled to. From the series expansion of $exp(-i(\omega_{31}-\omega_{a_1a_0})t)$

and the definition of $k_{a_1 \to a_0}$ we get from equation 5.13

$$\begin{aligned} T_1 &= 2Re\left(\int_0^\infty dt H^{SB}_{a_0 a_1}(t) H^{SB}_{a_1 a_0}(0) exp(-i\omega_{a_1 a_0} t)\right) \\ &\quad -i\omega_{31,a_1 a_0} 2Re\left(\int_0^\infty dt H^{SB}_{a_0 a_1}(t) H^{SB}_{a_1 a_0}(0) \cdot t \cdot exp(-i\omega_{a_1 a_0} t)\right) \qquad (5.16) \\ &= k_{a_1 \to a_0} - i\omega_{31,a_1 a_0} 2Re\left(\int_0^\infty dt H^{SB}_{a_0 a_1}(t) H^{SB}_{a_1 a_0}(0) \cdot t \cdot exp(-i\omega_{a_1 a_0} t)\right) \qquad (5.17) \end{aligned}$$

Using the property of complex correlation functions, the integral on the right hand-side of equation 5.17 transforms as

$$\begin{aligned} 2Re \cdot \left(\int_0^\infty dt H^{SB}_{a_0 a_1}(t) H^{SB}_{a_1 a_0}(0) \cdot t \cdot exp(-i\omega_{a_1 a_0} t)\right) \\ = (p.r) \cdot \left(\int_0^\infty dt C(t) \cdot t \cdot exp(-i\omega_{a_1 a_0} t)\right) \qquad (5.18) \end{aligned}$$

At room temperature the thermal occupation number for concerned frequencies is very small i.e. $n_j \ll 1$. Therefore from equations 5.15 and 5.18

$$\begin{aligned} \int_0^\infty dt H^{SB}_{a_0 a_1}(t) H^{SB}_{a_1 a_0}(0) \cdot t \cdot exp(-i\omega_{a_1 a_0} t) &\approx \sum_j \omega_j^2 S_j \underbrace{\int_{-\infty}^{+\infty} dt exp(-i\omega_j t) \cdot t \cdot exp(-i\omega_{a_1 a_0} t)}_{i\partial_{\omega_j}\delta(\omega_j + \omega_{a_1 a_0})} \\ &= i \sum_j \omega_j^2 S_j \delta'(\omega_j + \omega_{a_1 a_0}) \\ &= i \int_{-\infty}^{+\infty} d\omega \omega^2 J(\omega) \delta'(\omega_j + \omega_{a_1 a_0}) \qquad (5.19) \end{aligned}$$

Coupling strength weighted density of states $J(\omega)$ was introduced in the last line above for a continuous distribution of bath modes, and the limits of integration are set from $-\infty$ to $+\infty$. The negative frequencies in the integration can be introduced by forcing Heaviside function in the density of states, $J(\omega)$. The limits of integration let us use the following property of

Dirac delta function

$$\int_{-\infty}^{+\infty} d\omega \delta'(\omega - \omega_x) f(\omega) = -[f'(\omega)]_{\omega=\omega_x}$$

Using the above identify in equation 5.19 we get

$$= -i \frac{d}{d\omega} \left[J(\omega)\omega^2 \right]_{\omega=\omega_{a_1 a_0}}$$

We use the Debye spectral density that gives

$$J(\omega)\omega^2 = \frac{\lambda \omega \omega_0}{\omega^2 + \omega_0^2}$$

Using the Debye spectral density, property of Dirac delta function mentioned above, equation 5.18 and the definition of $k_{a_1 \to a_0}$ we get

$$2Re \cdot \left(\int_0^\infty dt H^{SB}_{a_0 a_1}(t) H^{SB}_{a_1 a_0}(0) \cdot t \cdot exp(-i\omega_{a_1 a_0} t) \right) = -i \frac{k_{a_1 \to a_0}}{\omega_{a_1 a_0}} \tag{5.20}$$

The quadratic term in $k_{a_1 \to a_0}$ is left out. From equations 5.17 and 5.20 we get

$$T_1 = k_{a_1 \to a_0} \left[1 - \frac{\omega_{31} - \omega_{a_1 a_0}}{\omega_{a_1 a_0}} \right] \tag{5.21}$$

A similar procedure for T_2, that was defined in equation 5.12, gives

$$T_2 = k_{b_0 \to a_0} \left[1 - \frac{\omega_{31} - \omega_{b_0 a_0}}{\omega_{b_0 a_0}} \right] \tag{5.22}$$

From equations 5.12, 5.21 and 5.22 we get

$$\begin{aligned} k_{3 \to 1} &= \left(U_{a_1 3} \right)^2 k_{a_1 \to a_0} \left(1 - \frac{(\omega_{31} - \omega_{a_1 a_0})}{\omega_{a_1 a_0}} \right) \\ &+ \left(U_{b_0 3} \right)^2 k_{b_0 \to a_0} \left(1 - \frac{(\omega_{31} - \omega_{b_0 a_0})}{\omega_{b_0 a_0}} \right) \end{aligned} \tag{5.23}$$

Similarly the rate of transition $k_{2\to1}$ from NBO state $|2\rangle$ to state $|1\rangle$ comes out to be

$$\begin{aligned} k_{2\to1} &= \left(U_{a_12}\right)^2 k_{a_1\to a_0}\left(1-\frac{(\omega_{21}-\omega_{a_1a_0})}{\omega_{a_1a_0}}\right) \\ &+ \left(U_{b_02}\right)^2 k_{b_0\to a_0}\left(1-\frac{(\omega_{21}-\omega_{b_0a_0})}{\omega_{b_0a_0}}\right) \end{aligned} \tag{5.24}$$

After deriving incoherent relaxation rates, we can now focus on coherent dynamics that are quantified using pure dephasing rates. The diagonal elements in the system-bath coupling are responsible for pure dephasing of coherences. By definition, the rate of pure dephasing is given by the Fourier transform at zero frequency of the correlation function of the diagonal elements of the system bath coupling

$$k_{21}^{pd} = 2Re\left(\int_0^\infty dt H_{11}^{SB}(t)H_{22}^{SB}(0)exp(-i\cdot 0\cdot t)\right) \tag{5.25}$$

Following the line of arguments mentioned above we get

$$\begin{aligned} k_{21}^{pd} &= (U_{a_12})^2 2Re\left(\int_0^\infty dt H_{a_0a_0}^{SB}(t)H_{a_1a_1}^{SB}(0)exp(-i\cdot 0\cdot t)\right) \\ &\quad +(U_{b_02})^2 2Re\left(\int_0^\infty dt H_{a_0a_0}^{SB}(t)H_{b_0b_0}^{SB}(0)exp(-i\cdot 0\cdot t)\right) \\ &= (U_{a_12})^2\cdot k_{a_1a_0}^{pd} + (U_{b_02})^2\cdot k_{b_0a_0}^{pd} \end{aligned} \tag{5.26}$$

5.7.3 Orientation of transition dipoles of R26.1 LH2

The two absorbing states in R26.1 LH2 are B850 and B850*. A simple approximation to the exciton structure is to assume that the oscillator strength resides in the pair of states $k = \pm1$ to $k = \pm4$ in accordance with a particle on a ring model. There is more than one state in B850 (see Novoderezkin et al. for details) and the above mentioned assumption is for illustrative purposes only. Including more states in the B850 does not change the model in the main manuscript. Each pair of states (e.g. $k = \pm1$) carry different angular momentum. A suitable linear combination of these degenerate states will give perpendicular transition

dipoles without affecting the energy eigenstates. For example, the transition dipoles of linear combinations of the degenerate states $k = \pm 1$ (figure 5.8(a)) can be perpendicular to each other (figure 5.8(b)). A similar treatment can be applied to all pairs of states. Furthermore, the states constructed of higher k states can be rotated and aligned to make an angle of either 45° or $180^\circ - 45^\circ$ with respect to the transition dipoles of the $k = \pm 1$ state manifold (figure 5.8(c)). The coherence response from a pair of transition dipoles is identical in the two cases when the angle between them is 45° and $180^\circ - 45^\circ$. Hence, for the purposes of studying coherences, only two states can be considered where the angle between their transition dipoles is 45°.

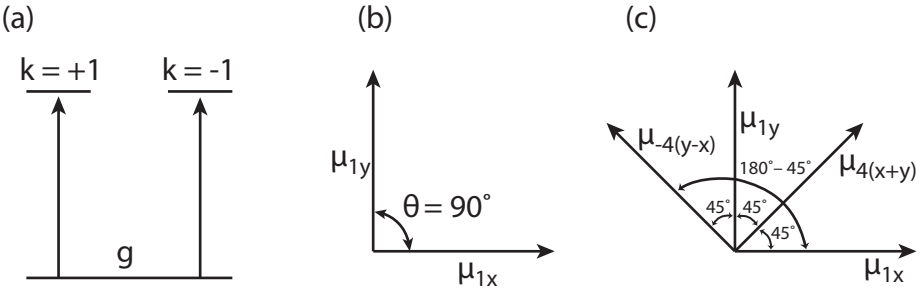

Figure 5.8: (a) The transition dipoles μ_{+1} and μ_{-1} of degenerate states $k = \pm 1$. (b) Linear combinations of the $k = \pm 1$ states can yield perpendicular transition dipoles shown here in the x and y directions. (c) Similarly, linear combinations of the $k = \pm 4$ states can be chosen to have perpendicular transition dipoles such that the angle between the transition dipoles of $k = \pm 1$ manifold states and $k = \pm 4$ manifold states is either 45° or $180^\circ - 45^\circ$. This scheme permits a simple reduction to a three state model without loss of accuracy.

5.7.4 Estimating mixing of vibrational and electronic states

In figure 5.9(a), the transition dipoles $\vec{\mu}_{a_0}$, $\vec{\mu}_{a_1}$ and $\vec{\mu}_{b_0}$ of BO states $|a_0\rangle$, $|a_1\rangle$ and $|b_0\rangle$ are shown in dashed yellow, solid yellow and cyan, respectively. The non-adiabatic coupling V_{NAC} between Born-Oppenheimer (BO) states $|a_1\rangle$ and $|b_0\rangle$ gives rise to non-Born-Oppenheimer (NBO) states $|2\rangle$ and $|3\rangle$. Although $|a_0\rangle$ is unaffected by non-adiabatic coupling, in the context of NBO states, $|a_0\rangle$ will be referred to as $|1\rangle$. V_{NAC} mixes transition dipoles $\vec{\mu}_{a_1}$ and $\vec{\mu}_{b_0}$ to give transition dipoles $\vec{\mu}_2$ and $\vec{\mu}_3$ of non-Born-Oppenheimer (NBO)

states $|2\rangle$ and $|3\rangle$, respectively. Both $\vec{\mu}_2$ and $\vec{\mu}_3$ are shown in green in figure 5.9(a). Here again, $\vec{\mu}_{a_0}$ is unaltered by non-adiabatic coupling. However, in the context of NBO state transition dipole $\vec{\mu}_{a_0}$ will be referred to as $\vec{\mu}_1$ (the dotted yellow vector in figure 5.9(a)). The vectors $\vec{\mu}_2$ and $\vec{\mu}_3$ make angles θ_{12} and θ_{13} with the vector $\vec{\mu}_1$, respectively. Figure 5.9(b) describes variation in coherence amplitude as a function of angle between the transition dipoles for the canonical polarization sequence (blue) and the coherence specific polarization sequence (red).

The energy difference between the NBO states $|2\rangle$ and $|3\rangle$, i.e. ΔE_{23} is estimated from the difference in the average of measured coherence frequencies in coherence-specific and canonical experiments. For a given value of ΔE_{23}, we can calculated the non-adiabatic coupling, V_{NAC}, and detuning, Δ, consistent with any mixing angle using the equations:

$$\Delta E_{23} = \sqrt{4V_{NAC}^2 + \Delta^2} \tag{5.27}$$

$$\theta_{mix} = \frac{1}{2}\tan^{-1}\left(\frac{2V_{NAC}}{\Delta}\right) \tag{5.28}$$

In the limiting case of absence of non-adiabatic coupling ($\theta_{mix} = 0^\circ$), transition dipole $\vec{\mu}_2$ is the same as transition dipole $\vec{\mu}_{a_1}$ and $\theta_{12} = 0^\circ$ as shown by the vertical dotted line on the left in figure 5.9 (b). Similarly, in the limiting case of absence of non-adiabatic coupling, $\vec{\mu}_3$ is the same as $\vec{\mu}_{b_0}$ and $\theta_{13} = 45^\circ$ (the vertical dotted line on the right in figure 5.9(b). The angle θ_{12} increases as the strength of non-adiabatic coupling increases i.e. $\theta_{12} > 0^\circ$ because $V_{NAC} > 0$ (and $\theta_{mix} > 0^\circ$). On the other hand, θ_{13} decreases as V_{NAC} increases i.e. $\theta_{13} < 45^\circ$ when $V_{NAC} > 0$ (or $\theta_{mix} > 0^\circ$).

The observed coherence is a sum of two coherences; one from each pair $(|1\rangle, |2\rangle)$ and $(|1\rangle, |3\rangle)$, with coherence lifetimes τ_{12} and τ_{13}, respectively. The state $|2\rangle$ which results from the mixing of $|a_1\rangle$ and $|b_0\rangle$, is predominantly a vibrational state. The predominant vibrational nature of state $|2\rangle$ makes τ_{12} typical of vibrational coherence lifetimes. Similarly the state $|3\rangle$, which results from the mixing of $|a_1\rangle$ and $|b_0\rangle$, is predominantly an electronic

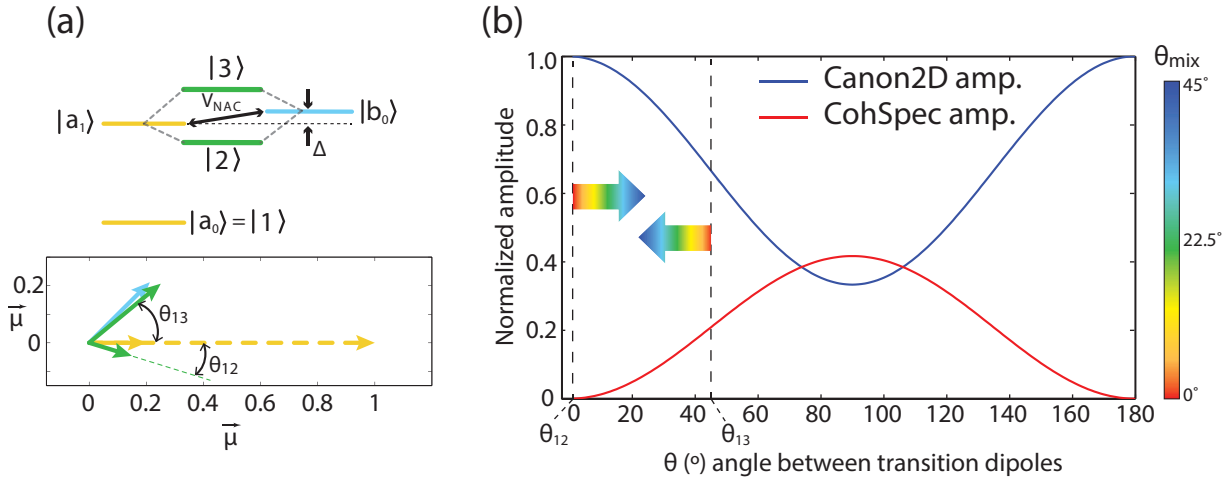

Figure 5.9: (a) The non-adiabatic coupling V_{NAC} and detuning Δ results in the mixing of BO states $|a_1\rangle$ (yellow) and $|b_0\rangle$ (cyan), giving NBO states $|2\rangle$ and $|3\rangle$ (both shown in green). The transition dipoles $\vec{\mu}_{a_0}$, $\vec{\mu}_{a_1}$ and $\vec{\mu}_{b_0}$ of states $|1\rangle$, $|2\rangle$ and $|3\rangle$ are shown in dotted yellow, solid yellow and cyan, respectively. The transition dipoles $\vec{\mu}_{a_1}$ and $\vec{\mu}_{b_0}$ mix to give $\vec{\mu}_2$ and $\vec{\mu}_3$. The state $|a_0\rangle$ and its transition dipole $\vec{\mu}_{a_0}$ (dotted yellow) remain unaltered but are referred to as $|1\rangle$ and $\vec{\mu}_1$ in the context of NBO states, respectively. The transition dipoles $\vec{\mu}_2$ and $\vec{\mu}_3$ make an angle θ_{12} and θ_{13} with respect to $\vec{\mu}_1$, respectively. (b) The amplitude of coherence signal as a function of angle between the transition dipole is plotted for the canonical 2D polarization sequence (blue) and coherence specific polarization sequence (red). $\theta_{12} = 0°$ (vertical dotted line on the left) and $\theta_{13} = 45°$ (vertical dotted line on the right) when non-adiabatic coupling is zero i.e. $\theta_{mix} = 0°$. The arrows on the two vertical dotted lines show the direction in which the lines and the corresponding angles move as the coupling (mixing angle θ_{mix}) increases.

state. The predominant electronic nature of state $|3\rangle$ makes τ_{13} typical of electronic coherence lifetimes. Consequently we have $\tau_{12} > \tau_{13}$. The lifetime of observed coherence is dependent not only on the lifetimes of individual coherences τ_{12} and τ_{13} from the pairs $(|1\rangle, |2\rangle)$ and $(|1\rangle, |3\rangle)$, but also on their amplitudes A_{12} and A_{13}, respectively. If $A_{12} > A_{13}$, the observed coherence lifetime τ_{obs} will be dominated by τ_{12}. If $A_{13} > A_{12}$, the observed coherence lifetime τ_{obs} will be dominated by τ_{13}. The amplitude of coherence is dependent on the pulse polarization sequence and the angle between the transition dipoles of the states involved in the coherence (figure 5.9(b)). From the experimental data we observe that the coherence lifetime $\tau_{Canon2D}$ in the canonical 2D experiment is greater than the coherence lifetime $\tau_{CohSpec}$ in the coherence specific experiment, i.e. $\tau_{Canon2D} > \tau_{CohSpec}$. Therefore we conclude that $A_{12}^{Canon2D} > A_{13}^{Canon2D}$, while $A_{13}^{CohSpec} > A_{12}^{CohSpec}$, where $A_{12}^{Canon2D}$ is the amplitude of coherence from the pair $(|1\rangle, |2\rangle)$ in canonical 2D experiment etc. This condition on the amplitudes limits the angles θ_{12} and θ_{12} as $0^\circ < \theta_{12} < \theta_{13} < 45^\circ$, thus setting the upper bound to non-adiabatic coupling or mixing angle $\theta_{mix} < 22.5^\circ$.

5.7.5 Comparison of signals stemming from different transition dipoles

The strength of diagonal and off-diagonal features appearing on the 2D plot depends on the orientation of transition dipoles and the polarization of the electric field that the transition dipoles interact with. Below we compare strength of diagonal and off-diagonal peaks in coherence specific experiment. These experiments show suppression of population transfer pathways, when compared to negative waiting times, indicating how well pulse polarization is controlled. This population transfer peak arises from mis-ordering of the pulses (interaction order from 1324 and 3124), and is quite strong compared to later signals; yet, the population transfer time is longer (¿100fs) than the dephasing during the coherence time (¡80fs) indicating strong suppression of unwanted signals with our polarization scheme. On the left is the dynamics from the $B850^*$ diagonal (red trace) and $B850^* - B850$ off-diagonal peak (blue trace). The diagonal peak (red) trace is flat showing no population dynamics as

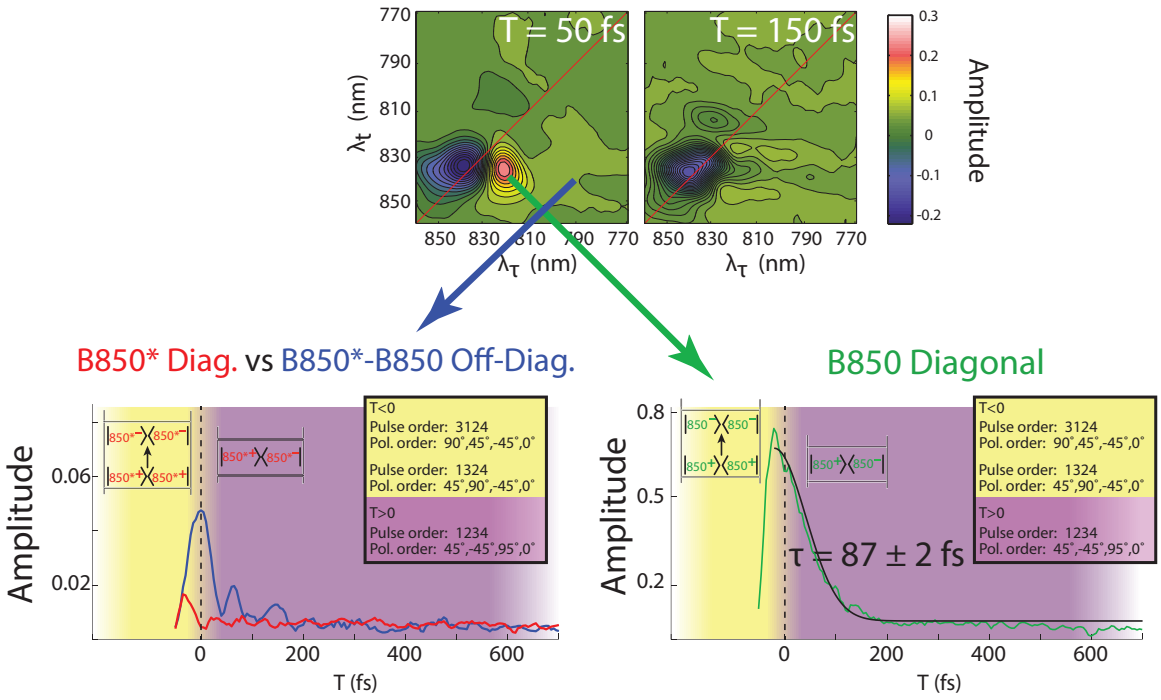

Figure 5.10: Left $B850^*$ diagonal trace (red) and $B850^* - B850$ lower off-diagonal trace (blue). The inset shows part of the Feynman pathways that can contribute to $B850^*$ diagonal peak for negative (shaded yellow) and positive (shaded pink) population times. Right $B850$ diagonal trace (green). The inset shows part of the Feynman pathways that can contribute to B850 diagonal peak for negative (shaded yellow) and positive (shaded pink) times when there is pulse overlap. The green trace ($B850$ diagonal trace) is fitted to a Gaussian function, shown in black along with its life time $\tau = 87 \pm 2$ fs.

should be the case with signals with parallel transition dipoles in coherence specific experiment. There is a short lived, small signal that shows up at the $B850^*$ diagonal for negative waiting times. Such a signal can be attributed to the depolarization of $B850^*$ excitons. For example, if we represent $k = +4$ and $k = -4$ states, that contribute to the $B850^*$ band, as 850^{*+} and 850^* respectively, then depolarization dynamics such as conversion of $|8500^{*+}\rangle\langle 850^{*+}|$ population to $|8500^{*-}\rangle\langle 850^{*-}|$ will show up at the $B850^*$ diagonal for negative times. For positive waiting times we expect to see signals corresponding to decoherence of $|8500^{*+}\rangle\langle 850^{*-}|$ coherences that should show up as a Gaussian trace. We do not observe such a Gaussian trace. We think it is because of the very small dipole strength of the $B850^*$ states that the signal gets buried in the noise floor. For the $B850$ states, we expect to see a similar trend. The conversion of $|8500^{+}\rangle\langle 850^{+}|$ to $|8500^{-}\rangle\langle 850^{-}|$ will appear for negative waiting times. For positive waiting times we expect the extinction of $|8500^{+}\rangle\langle 850^{-}|$. Both the dynamics contribute for negative and positive waiting times. We observe a 87 ± 2 fs life time of the above mentioned dynamics which is commensurate with earlier reports.

5.7.6 Incoherent dynamics from $B850^*$ states to $B850$ states

In figure 5.2(c) in the main text we had shown the trace of $B850^*$ state in waiting time T and extracted the dynamics of $B850^*$ states. Here we show the trace of lower off diagonal peak and expound the signatures of energy transfer. On the left is the Feynman diagram that represents energy transfer from $B850^*$ states to $B850$ states. Interaction with first two pulses creates population of $B850^*$ state. The system evolves for waiting time T during which the system incoherently hops into $B850$ states. Interaction with pulse 3 results in the emission of signal. The strength of the lower off-diagonal peak depends on the populations transferred to $B850$ states and scales as $|\mu_{B850^*}|^2 \cdot |\mu_{B850}|^2$ where μ_{B850^*} and μ_{B850} are dipole strengths of $B850^*$ and $B850$ states. We take a trace of the off-diagonal peak at $[\lambda_\tau, \lambda_t] = [790\text{nm}, 840\text{nm}]$. The peak first grows for first ~ 150 fs due to population transfer from state $B850^*$ to $B850$. It subsequently decays and the decay can be explained in a

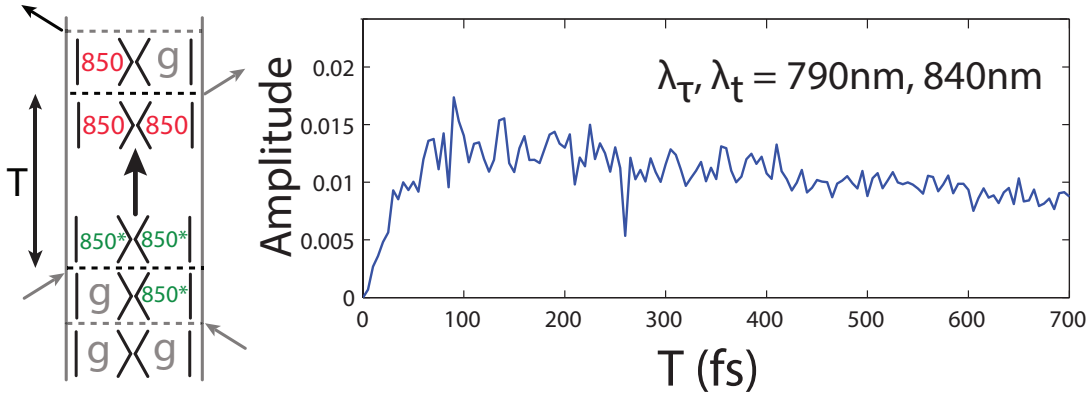

Figure 5.11: Left: The Feynman diagram representing energy transfer from $B850^*$ states to $B850$ states. Right: Lower off-diagonal peak the shows energy transfer.

couple of ways. First, the exciton is delocalized when it reaches $B850$ ring and then localizes at 100 fs time scale. The process of localization results in decrease of dipole strength of $B850$ state. Since the strength of the off-diagonal peak depends on the dipole strength of $B850$ states, the process of exciton localization will result in decrease if lower off-diagonal peaks intensity. Second, the $B850$ state relaxes out of band to its fluorescence state that results in the loss of detectable $B850$ populations, hence a decrease in intensity of lower off-diagonal peak.

5.7.7 Non-linear regression of coherence signals confidence in fit parameters

The accuracy of our retrieved parameters from our regression depends on the signal-to-noise ratio of the experiment. Use of an explicit model with limited degrees of freedom affords us the ability to resolve frequency differences smaller than the nominal Fourier resolution of the experiment. For example, in main text figure 5.3(b),(c) we show fits to coherence signals and retrieved parameters. The data is from 0 fs to 250 fs in steps of 5 fs. The data range and the sampling rate sets a 130 cm^{-1} Fourier resolution in the frequency domain. The error in the fits for frequency of coherence signals shown in figure 5.3(b),(c) is around ~ 20 cm^{-1}; below the Fourier resolution in the frequency domain.

Explaining this "anomalous resolution really comes down to comparing the FFT Fourier resolution in the presence of a Null Hypothesis vs nonlinear regression to a model function i.e. to say that if the frequency is analyzed in the absence of a model then frequency domain resolution sets the error bar. However, if the frequency is analyzed with a model for the frequency the resolution is not set by frequency domain resolution. Using a model with fewer degrees of freedom leads to overdetermined parameters and permits finer resolution.

Here, we show a simple statistical demonstration that we can extract the parameters of interest with more accuracy than set by the frequency domain resolution. We calculate a damped sinusoidal signal with known time constant (150 fs) and oscillation frequency (700 cm^{-1}), and retrieve the parameters. For this simulation, we sample points from 0 to 250 fs in steps of 5 fs and we fit the same five-parameter fit as described in the manuscript. Further, we have added noise equal to 20% of the amplitude of the sine wave. We show one iteration with error bars from the regression, but we then repeat the simulation and regression 1000 times and show that the error bar is correct. Consider the following figure. In blue is the

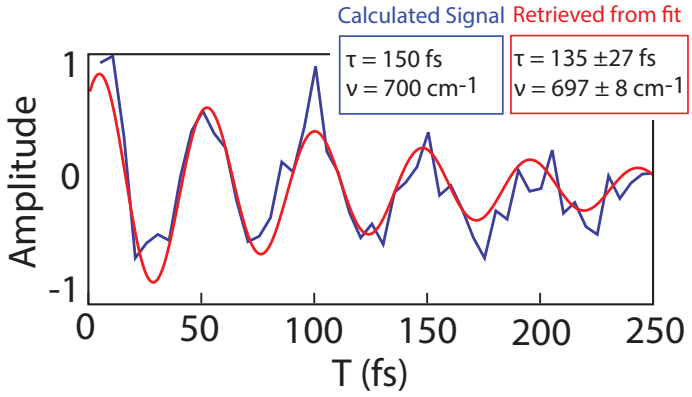

Figure 5.12: The calculated coherence signal with 20% noise is shown in blue, and the fit is shown in red.

calculated signal ($\tau = 150$fs, $\nu = 700$ cm^{-1} , 20% white noise) for waiting time 0 to 250 fs in steps of 5fs. The parameters that characterize the blue trace are then retrieved by using the fitting model we use in our data analysis (red trace is the fit). For the above shown trace, the retrieved life time is $\tau = 135 \pm 27$ fs, and the oscillation frequency is 697 ± 8 cm^{-1}. For

1000 iterations of the simulation, the average frequency was obtained to be 700 ± 7 cm^{-1}; that is, the average of the retrieved frequencies shows that there is no bias in the fit and that the error bar retrieved from a single fit is reliable.

5.8 References

[1] van Amerongen, H., Valkunas, L., and van Grondelle, R. *Photosynthetic Excitons*; World Scientific: Singapore, 2000.

[2] Hu, X. C., Ritz, T., Damjanovic, A., and Schulten, K. (1997) Pigment organization and transfer of electronic excitation in the photosynthetic unit of purple bacteria. *Journal of Physical Chemistry B 101*, 3854–3871.

[3] Sundstrom, V., Pullerits, T., and van Grondelle, R. (1999) Photosynthetic light-harvesting: Reconciling dynamics and structure of purple bacterial LH2 reveals function of photosynthetic unit. *Journal of Physical Chemistry B 103*, 2327–2346.

[4] Cho, M., Vaswani, H. M., Brixner, T., Stenger, J., and Fleming, G. R. (2005) Exciton Analysis in 2D Electronic Spectroscopy. *The Journal of Physical Chemistry B 109*, 10542–10556.

[5] Knox, R. S. (1996) Electronic excitation transfer in the photosynthetic unit: Reflections on work of William Arnold. *Photosynthesis Research 48*, 35–39.

[6] Leegwater, J. A. (1996) Coherent versus incoherent energy transfer and trapping in photosynthetic antenna complexes. *Journal of Physical Chemistry 100*, 14403–14409.

[7] Vos, M. H., Rappaport, F., Lambry, J. C., Breton, J., and Martin, J. L. (1993) Visualization of Coherent Nuclear Motion in a Membrane-Protein by Femtosecond Spectroscopy. *Nature 363*, 320–325, Ld917 Times Cited:413 Cited References Count:39.

[8] Savikhin, S., Buck, D. R., and Struve, W. S. (1997) Oscillating anisotropies in a bacteriochlorophyll protein: Evidence for quantum beating between exciton levels. *Chemical Physics 223*, 303–312, Ym199 Times Cited:63 Cited References Count:37.

[9] Romero, E., Augulis, R., Novoderezhkin, V. I., Ferretti, M., Thieme, J., Zigmantas, D., and van Grondelle, R. (2014) Quantum coherence in photosynthesis for efficient solar-energy conversion. *Nat Phys 10*, 676–682.

[10] Schlau-Cohen, G. S., Ishizaki, A., Calhoun, T. R., Ginsberg, N. S., Ballottari, M., Bassi, R., and Fleming, G. R. (2012) Elucidation of the timescales and origins of quantum electronic coherence in LHCII. *Nat Chem 4*, 389–395, 10.1038/nchem.1303.

[11] Panitchayangkoon, G., Hayes, D., Fransted, K. A., Caram, J. R., Harel, E., Wen, J., Blankenship, R. E., and Engel, G. S. (2010) Long-lived quantum coherence in photosynthetic complexes at physiological temperature. *Proceedings of the National Academy of Sciences 107*, 12766–12770.

[12] Hybl, J. D., Albrecht, A. W., Faeder, S. M. G., and Jonas, D. M. (1998) Two-Dimensional Electronic Spectroscopy. *Chemical Physics Letters 297*, 307–313.

[13] Cowan, M. L., Ogilvie, J. P., and Miller, R. J. D. (2004) Two-dimensional spectroscopy using diffractive optics based phased-locked photon echoes. *Chemical Physics Letters 386*, 184–189.

[14] Brixner, T., Mancal, T., Stiopkin, I. V., and Fleming, G. R. (2004) Phase-stabilized two-dimensional electronic spectroscopy. *The Journal of Chemical Physics 121*, 4221–4236.

[15] Engel, G. S., Calhoun, T. R., Read, E. L., Ahn, T. K., Mancal, T., Cheng, Y. C., Blankenship, R. E., and Fleming, G. R. (2007) Evidence for wavelike energy transfer through quantum coherence in photosynthetic systems. *Nature 446*, 782–786.

[16] Lee, H., Cheng, Y. C., and Fleming, G. R. (2007) Coherence dynamics in photosynthesis: Protein protection of excitonic coherence. *Science 316*, 1462–1465.

[17] Collini, E., Wong, C. Y., Wilk, K. E., Curmi, P. M. G., Brumer, P., and Scholes, G. D. (2010) Coherently wired light-harvesting in photosynthetic marine algae at ambient temperature. *Nature 463*, 644–647, 10.1038/nature08811.

[18] Mohseni, M., Rebentrost, P., Lloyd, S., and Aspuru-Guzik, A. (2008) Environment-assisted quantum walks in photosynthetic energy transfer. *Journal of Chemical Physics 129*.

[19] Plenio, M. B., and Huelga, S. F. (2008) Dephasing-assisted transport: quantum networks and biomolecules. *New Journal of Physics 10*.

[20] Christensson, N., Kauffmann, H. F., Pullerits, T., and Mancal, T. (2012) Origin of Long-Lived Coherences in Light-Harvesting Complexes. *Journal of Physical Chemistry B 116*, 7449–7454.

[21] Tiwari, V., Peters, W. K., and Jonas, D. M. (2013) Electronic resonance with anticorrelated pigment vibrations drives photosynthetic energy transfer outside the adiabatic framework. *Proceedings of the National Academy of Sciences of the United States of America 110*, 1203–1208.

[22] Chenu, A., Christensson, N., Kauffmann, H. F., and Mancal, T. (2013) Enhancement of Vibronic and Ground-State Vibrational Coherences in 2D Spectra of Photosynthetic Complexes. *Scientific Reports 3*.

[23] Womick, J. M., and Moran, A. M. (2011) Vibronic Enhancement of Exciton Sizes and Energy Transport in Photosynthetic Complexes. *Journal of Physical Chemistry B 115*, 1347–1356.

[24] Davidson, E., and Cogdell, R. J. (1981) The Polypeptide Composition of the B850 Light-Harvesting Pigment-Protein Complex from Rhodopseudomonas-Sphaeroides, R26.1. *Febs Letters 132*, 81–84, Mj603 Times Cited:39 Cited References Count:22.

[25] Hochstrasser, R. M. (2001) Two-dimensional IR-spectroscopy: polarization anisotropy effects. *Chemical Physics 266*, 273–284.

[26] Woutersen, S., and Hamm, P. (2000) Structure determination of trialanine in water using polarization sensitive two-dimensional vibrational spectroscopy. *Journal of Physical Chemistry B 104*, 11316–11320.

[27] Dreyer, J., Moran, A. M., and Mukamel, S. (2003) Coherent three-pulse spectroscopy of coupled vibrations in a rigid dipeptide: Density functional theory simulations. *Journal of Physical Chemistry B 107*, 5967–5985, 691EN Times Cited:18 Cited References Count:75.

[28] Zanni, M. T., Ge, N. H., Kim, Y. S., and Hochstrasser, R. M. (2001) Two-dimensional IR spectroscopy can be designed to eliminate the diagonal peaks and expose only the crosspeaks needed for structure determination. *Proceedings of the National Academy of Sciences of the United States of America 98*, 11265–11270.

[29] Read, E. L., Engel, G. S., Calhoun, T. R., Mancal, T., Ahn, T. K., Blankenship, R. E., and Fleming, G. R. (2007) Cross-peak-specific two-dimensional electronic spectroscopy. *Proceedings of the National Academy of Sciences of the United States of America 104*, 14203–14208, 208QF Times Cited:69 Cited References Count:24.

[30] Fidler, A. F., Singh, V. P., Long, P. D., Dahlberg, P. D., and Engel, G. S. (2013) Time Scales of Coherent Dynamics in the Light-Harvesting Complex 2 (LH2) of Rhodobacter sphaeroides. *Journal of Physical Chemistry Letters 4*, 1404–1409.

[31] Harel, E., Fidler, A. F., and Engel, G. S. (2010) Real-time mapping of electronic struc-

ture with single-shot two-dimensional electronic spectroscopy. *Proceedings of the National Academy of Sciences of the United States of America 107*, 16444–16447.

[32] Singh, V. P., Fidler, A. F., Rolczynski, B. S., and Engel, G. S. (2013) Independent phasing of rephasing and non-rephasing 2D electronic spectra. *Journal of Chemical Physics 139*, 211RO Times Cited:4 Cited References Count:25.

[33] Lozovoy, V. V., Pastirk, I., and Dantus, M. (2004) Multiphoton intrapulse interference. IV. Ultrashort laser pulse spectral phase characterization and compensation. *Optics Letters 29*, 775–777, 805JN Times Cited:153 Cited References Count:16.

[34] Novoderezhkin, V., Wendling, M., and van Grondelle, R. (2003) Intra- and interband transfers in the B800-B850 antenna of Rhodospirillum molischianum: Redfield theory modeling of polarized pump-probe kinetics. *Journal of Physical Chemistry B 107*, 11534–11548.

[35] Polyutov, S., Kuhn, O., and Pullerits, T. (2012) Exciton-vibrational coupling in molecular aggregates: Electronic versus vibronic dimer. *Chemical Physics 394*, 21–28.

[36] Butkus, V., Valkunas, L., and Abramavicius, D. (2014) Vibronic phenomena and exciton-vibrational interference in two-dimensional spectra of molecular aggregates. *Journal of Chemical Physics 140*, 302OM Times Cited:3 Cited References Count:68.

[37] Spano, F. C. (2006) Excitons in conjugated oligomer aggregates, films, and crystals. *Annual Review of Physical Chemistry 57*, 217–243, 044JO Times Cited:118 Cited References Count:133 Annual Review of Physical Chemistry.

[38] Herzberg, G. *Electronic Spectra and Electronic Structure of Polyatomic Molecules*; Krieger Publishing Company, 1991.

[39] Chumanov, G., Picorel, R., de Zarate, I. O., Cotton, T. M., and Seibert, M. (2000) Resonance raman and surface-enhanced resonance raman spectra of LH2 antenna complex

from Rhodobacter sphaeroides and Ectothiorhodospira sp excited in the Q(x) and Q(y) transitions. *Photochemistry and Photobiology 71*, 589–595, 313FM Times Cited:8 Cited References Count:34.

[40] Fischer, G. *Vibronic coupling: the interaction between the electronic and nuclear motions*; Academic Press, 1984.

[41] Harris, D., and Bertolucci, M. *Symmetry and Spectroscopy: An Introduction to Vibrational and Electronic Spectroscopy*; Dover Publications, 1978.

[42] Zazubovich, V., Tibe, I., and Small, G. J. (2001) Bacteriochlorophyll a Franck-Condon factors for the S-0 -¿ S-1(Q(y)) transition. *Journal of Physical Chemistry B 105*, 12410–12417, 502CY Times Cited:27 Cited References Count:48.

CHAPTER 6

OBSERVATION OF ENHANCED CIRCULAR DICHROISM AND CHIRAL DYNAMICS IN LH2

6.1 Introduction

Light-harvesting antenna complexes harvests energy for photosynthetic organisms by using sunlight to create excited states called excitons. Upon creation the exciton is transported to the reaction center (RC) where more stable form of energy storage ensues. The remarkable quantum efficiency of exciton transported to the RC has attracted immense experimental and theoretical studies.[1–4] These studies have advanced our understanding of how different structural properties affect energy transfer. However, chirality of light harvesting complexes, a ubiquitous property across different photosynthetic species, has not been sufficiently investigated for its effect on energy transfer dynamics. Consequently, our understanding of chiralitys effect on energy transfer dynamics is skimpy. In the account below we present results of chiral two-dimensional electronic spectroscopy (C2DES) performed on light-harvesting complex 2 (LH2) of *Rhodobacter (Rb.) sphaeroides*. The experimental results reveal that chirality significantly affects energy transfer dynamics through two mechanisms that were previously unknown. First, chirality enhances circular dichroism in a densely packed system of chromophores, such as LH2. Second, chirality affects dynamics of states with opposite angular momentum.

Light harvesting complex 2 (LH2) from *Rb. sphaeroides* has two rings of chromophores called B800 and B850 rings that absorb at 800 nm and 850 nm, respectively. Owing to LH2s ring like structure, the exciton states of LH2 can be conceived as eigenstates of a particle on a ring. The eigenstates are assigned quantum numbers 'k'. For B850 ring, the eigenstates have quantum numbers $k = 0, \pm 1, \pm 2, \pm 8, 9$ resulting from the Q_y transition of the 18 chromophores of the B850 ring. Similarly the B800 ring has eigenstates with quantum numbers

$k = 0, \pm 1, \pm 4$ resulting from the Q_y transition on the 9 chromophores of the B800 ring. The states with opposite signs have either clockwise or anti-clockwise angular momentum. For our purposes we allocate +ve k quantum number states clockwise angular momentum and -ve k quantum numbers states anti-clockwise angular momentum. We collectively denote bright states on B800 ring with clockwise angular momentum as $B800^+$ and with anticlockwise angular momentum as $B800^-$. Similarly, we collectively denote bright states on B850 ring with clockwise angular momentum as $B850^+$ and with anticlockwise angular momentum as $B850^-$. Angular momentum conservation dictates that energy transfer takes place from $B800^+$ to $B850^+$, and from $B800^-$ to $B850^-$. In the absence of chirality states with clockwise and anticlockwise angular momentum will absorb left circularly polarized light (LCPL) and right circularly polarized light (RCPL) in the same amount. However the chiral arrangement of chromophores lets clockwise angular momentum states absorb LCPL more than RCPL. Conversely, chirality lets anticlockwise angular momentum states absorb RCPL more than LCPL.

While the effect of chirality on absorption is known, its effect on ultrafast dynamics is unknown. In order to investigate the effect of chirality on dynamics we employ two dimensional electronic spectroscopy (2DES). We employ 2DES because it allows us to control timing between all light-matter interactions. This control enables us to measure absorption frequencies ω_τ by systematically changing the timing τ between first and second light matter interaction. The first two interaction result in an excited system that is allowed to evolve for a time period T, called the waiting time. A third pulse then probes the system by stimulating emission form the states. The stimulated emission signal is then frequency resolved to give emission frequencies ω_t, and imaged on the camera. A fourth pulse called the local oscillator (LO) is used as a reference to measure the phase and amplitude of the emitted signal.

In order to study the effect of chirality on dynamics we excite states with opposite chiral-

ity i.e clockwise and anticlockwise angular momentum states, and observe their dynamics. The excited states with opposite chirality are created using left (L) and right (R) circularly polarized first pulse. LCPL excites clockwise angular momentum states and RCPL excites anticlockwise angular momentum states on both the B800 and B850 ring. Excitation by the first pulse results in the creation of coherence between ground and excited state. Creation of ground-excited state coherence results in helical charge motion owing to LH2s chirality. The helical charge motion results in differential absorption of LCPL and RCPL. A systematically delayed second pulse encodes the effect of chirality into the absorption axis, ω_τ. The clockwise and anticlockwise angular momentum states resulting from left and right circularly polarized light of laser pulse 1 are allowed to relax after interaction with laser pulse 2. The third pulse stimulates emission from the states and informs on the effect of chirality, if any, on energy transfer dynamics. The LO eventually measures the strength of the signal. While the first pulse is LCP or RCP to create clockwise and anticlockwise states, the second, third and fourth pulse are linearly polarized, and with respect to the laboratory frame of reference are referred to as polarized along the 'Y' axis. Therefore the pulse polarization schemes employed are LYYY and RYYY, where L(R) and Y denote the state of polarization of pulses 1, 2, 3 and 4, going from left to right in the scheme.[5;6]

6.2 Results and discussion

Figure 6.1 shows the 2DES plots form LYYY and RYYY pulse polarization sequence experiments. Top panel (blue) shows 2DES plots from LYYY polarization sequence experiment for $T = 0$ fs and $T = 600$ fs. Bottom panel (red) shows 2DES plots from RYYY polarization sequence experiment for $T = 0$ and $T = 600$ fs. The red line on the 2DES map defines the diagonal, and features that lie on the diagonal result from absorption and emission of B800 and B850 states. The intensity of the diagonal feature at $(\lambda_\tau, \lambda_t)$=(800,800) nm correspond to the energy content of $B800^+$ (top row, blue panel) and $B800^-$ (bottom row, red panel)

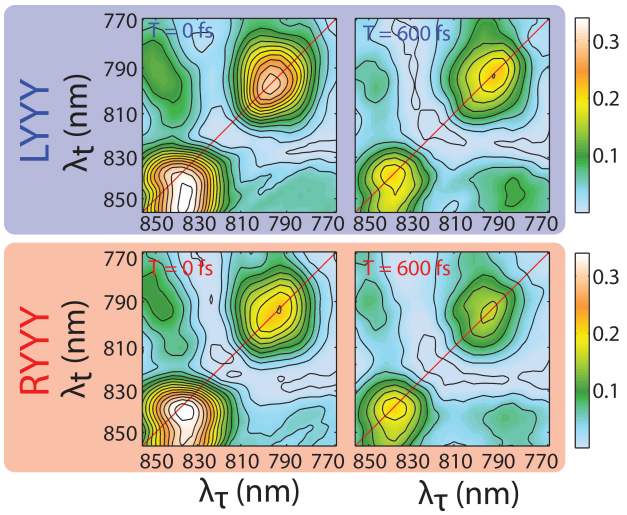

Figure 6.1: Top and bottom row show 2D maps at $T = 0$ fs and $T = 600$ fs, acquired with LYYY and RYYY polarization scheme.

states. Therefore to study the dynamics of energy transfer from $B800^+$ states to $B850^+$ states we look at the time evolution of the $B800^+$ peak from LYYY sequence. Similarly, to study the dynamics of energy transfer from $B800^-$ states to $B850^-$ states we look at the time evolution of the $B800^-$ peak from RYYY sequence. In figure 6.2 we show the trace from the diagonal $B800^+$ and $B800^-$ peak in blue and red, respectively. The amplitude of

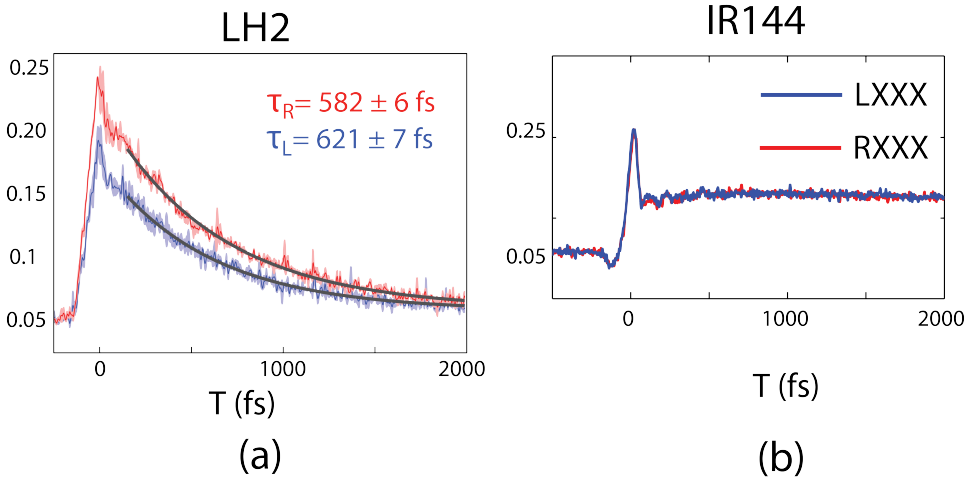

Figure 6.2: (a) and (b)show the dynamics of LH2 and IR144, respectively, with LYYY and RYYY polarization scheme.

the trace at $T = 0$ fs gives information about the relative amount of energy absorbed by

$B800^+$ and $B800^-$ states, and the decay of the trace corresponds to the rate at which energy is transferred from $B800^+$ to $B850^+$ and from $B800^-$ to $B850^-$ states. We observe that the difference in amount of energy absorbed by $B800^+$ and $B800^-$ is larger than what might be predicted by linear circular dichroism. From the amplitude of the two traces at around $T = 0$ fs we find that $B800^-$ states absorb 10% more than $B800^+$ states. By fitting the traces to a mono-exponential we find the rate of energy transfer from $B800^+$ to $B850^+$ and from $B800^-$ to $B850^-$ states. We observe that find that $B800^-$ states not only absorb more, but also shuttle out energy faster compared to $B800^+$ states. While $B800^+$ states transfer energy to $B850^+$ states in $\tau_L = 627 \pm 7$ fs, $B800^-$ states transfer energy to $B850^-$ states in $\tau_R = 582 \pm 6$ fs. We attribute the difference in absorption and dynamics of $B800^+$ and $B800^-$ states to chirality of LH2 because when identical experiments were performed on an achiral molecule, IR144, no difference in the absorption and dynamics was observed after excitation by LCPL and RCPL. (Methods section describes how identical experimental conditions were achieved for experiments on LH2 and IR144). Figure 2(b) shows the dynamics of IR144 resulting from excitation by LCPL and RCPL in blue and red, respectively. We first address the point of enhanced circular dichroism and then the difference in dynamics of states with opposite chirality.

The large difference in absorption of LCPL by B800+ and RCPL by B800- can be explained by evoking coherent mechanism that involves simultaneous excitation of both B800 and B850 rings. The differential absorption of LCPL and RCPL by a chiral molecule, or circular dichroism, is quantified using the Rosenfeld equation

$$R_i = Im(m_i \cdot \mu_i) \tag{6.1}$$

where R_i is the rotational strength, μ_i the transition dipole and m_i the magnetic dipole associated with the absorbing state 'i'. The transition dipole and the magnetic dipole together account for the helical charge motion in chiral molecules, which is responsible for differential

absorption of LCPL and RCPL. In the case of $B800^+$ and $B800^-$ states, in addition to their individual magnetic transition dipole, they also develop induced magnetic transition dipole from $B850^+$ and $B850^-$ states during the coherence time. During coherence time, the circular motion of charges from $B800^+$ and $B800^-$ states is analogous to ring current. The ring current results in magnetic transition dipole that adds to that of states $B800^+$ and $B800^-$. This argument is equivalent to saying that divergence of displacement field is zero. The above-mentioned mechanism operates only when both B800 and B850 are simultaneously excited in a coherent fashion using a broad band pulse. In order to test this hypothesis we do experiments with limited bandwidth pulse where only the B800 ring is excited and not the B850 ring. In figure 6.3 we show the trace from B800 for both LCPL and RCPL. The traces do not differ in absorption of LCPL and RCPL, or in the ensuing dynamics.

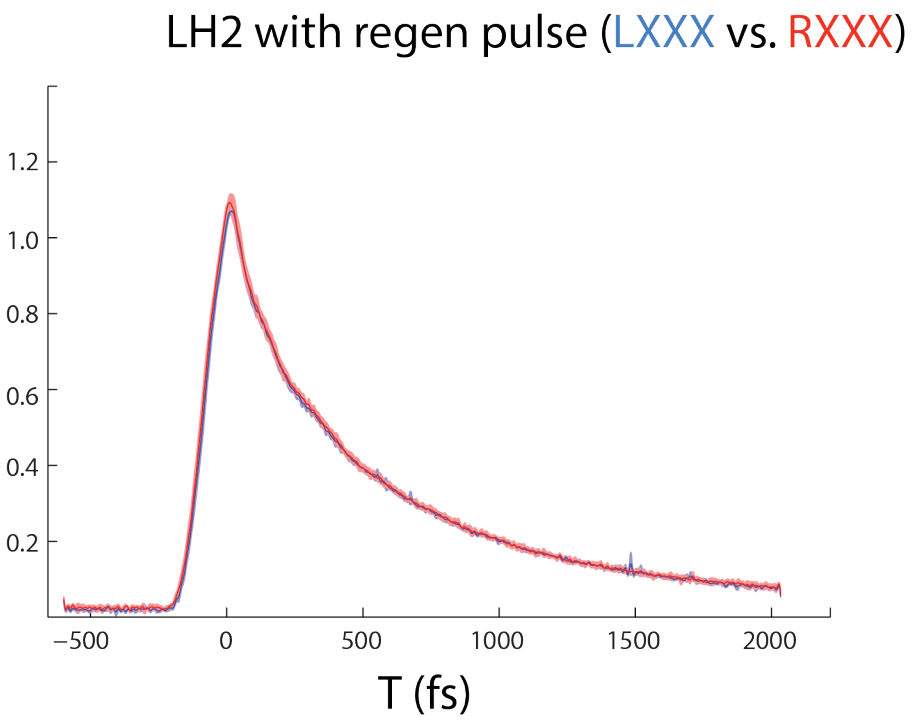

Figure 6.3: Dynamics of B800 states of LH2 with LYYY and RYYY polarization scheme, acquired with regen pulse

The hypothesis, of B850 ring current enhances difference in absorption of LCPL and RCPL, is tested by performing power dependent measurements as well. In the power de-

pendent studies we systematically decrease the power from initial value to 95%, 90%, 85% and 75%. As the power decreases the probability of simultaneously exciting B800 and B850 decreases. As a consequence, we expect a decrease in difference in the absorption of LCPL and RCPL by the B800 ring. In figure 6.4 we show the measured difference between the absorption of LCPL and RCPL by the B800 ring as a function of power. The x-axis is relative power and y-axis is measured difference.

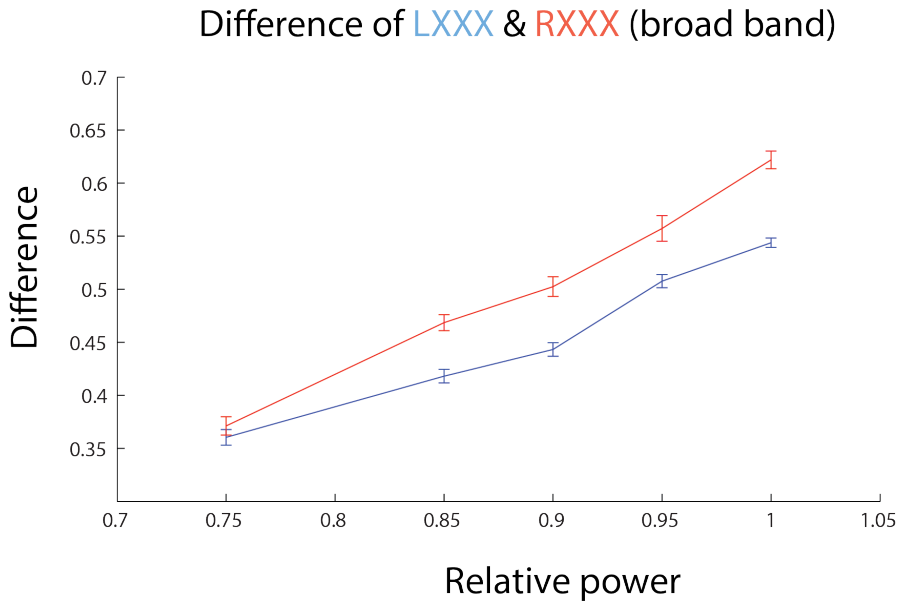

Figure 6.4: Difference in amplitude between signals acquired with LYYY (blue) and RYYY (red) polarization scheme.

Not only enhanced circular dichroism in LH2 has not been observed before, but also the difference in dynamics of states with opposite angular; B800+ to B850+ transfer takes place in 621 fs (τ_L) and B800- to B850- transfer takes place in 582 fs τ_R. This difference in dynamics can be explained by invoking Förster mechanism of energy transfer along with Redfield mechanism. The red tail of B800 band overlaps with the blue tail of the B850 band. The coupling between the two bands come from the enhancement of dipole strength of B800 ring because of dynamics in B850 ring.

6.3 Methods

6.3.1 Sample Preparation

LH2 was isolated based on a procedure adapted from Frank et al. Rhodobacter sphaeroides cells were grown semi-aerobically at 30°C in the dark.[7] Cells were lysed using a French press at 14,000 PSI and centrifuged (12,000 RPM JA 30.50 Ti for 20 minutes at 4°C) to remove unlysed cell debris. The supernatant was ultra centrifuged (50,000 RPM 50.2 Ti for 90 minutes) resulting in a pellet containing light harvesting complexes. The pellet was solubilized to OD 50 cm_1 at 850 nm in 0.6% Lauryldimethylamine-oxide (LDAO) 10 mM Tris-HCl and then run through a continuous 0.6 1.2 M sucrose gradient in an ultra centrifuge (50,000 RPM at 4°C) overnight. The lower red band was removed and dialysed into 5 mM imidazole 10 mM Tris-HCl 0.06% LDAO at pH 7.5. The LDAO in dialysed sample was increased by an additional 0.06% and then separated on Ni-NTA column to remove Histidine-tagged reaction center. The LH2 fraction eluted from the column under 5 mM imidazole 10 mM Tris-HCl 0.06% LDAO at pH 7.5. The LH2 fraction was then purified by a DEAE-Sephacel anion exchange column eluting with 0-320 mM NaCl 20 mM Tris-HCl 0.1% LDAO at pH 8.0. The purified isolated LH2 sample was buffer exchanged into 20 mM Tris-HCl 0.06% LDAO at pH 7.5 to 0.3 OD at 800 nm in a 200 m quartz sample cell.

6.3.2 IR144 control along with LH2

The experiments on IR144 and LH2 are done under identical conditions. We first acquire 5 runs of LYYY data on IR144 that takes approximately 20 minutes total. After taking 5 runs of data on IR144, we flow out IR144 and flow in LH2. We then acquire 5 runs of LYYY data on LH2. We then switch to RYYY polarization sequence and acquire 5 runs of LH2. After acquiring 5 runs of LH2, we flow out LH2 and flow in IR144. We then acquire 5 runs of RYYY on IR144. This procedure of data acquisition ensures that LH2 and IR144 are acquired under identical polarization conditions. As expected for an achiral molecule, IR144

does not show any difference in absorption of LCPL and RCPL, or in the ensuing dynamics. This shows that the difference in absorption of LCPL and RCPL, and the ensuing difference in dynamics of LH2 have origin in molecular chirality.

6.3.3 Two-dimensional electronic spectroscopy

We use GRAPES spectrometer that has been described in detailed elsewhere.[8–10] Briefly, a Coherent Micra Ti:sapphire oscillator seeds a Coherent Legend Elite USP-HE regenerative amplifier to generate 30 fs, transform-limited pulses centered at 805 nm (30 nm FWHM) with a 5 kHz repetition rate. Additional bandwidth is achieved by, first, focusing the pulse in argon gas (2 atm), and then refocusing the pulse in air, to generate 100 nm FWHM pulse with 0.3% power stability measured over 30 minutes. A 50:50 beam splitter and two wedged optics are used to create four pulses. The timing between pulses 1 and 2 is spatially encoded by using GRAPES mirrors that are then focused to a line in a homogeneous sample. The pulse is compressed at the sample using the multiphoton intrapulse interference phase scan method provided by Biophotonics Solution Inc. to get 12 fs pulses. 2D-ES experiments are performed with LYYY and RXXX polarization sequence. The polarizations are altered using quarter wave plate (ThorLabs), and calibrated using a Glan-Thompson polarizer (attenuation factor 10^{-5}). Data is acquired at video rate in about 3.5 seconds.

6.3.4 Controlling and analyzing polarization of pulses

We first remove any ellipticity that might be present in the pulses by using Glan-Thompson (GT) polarizer. A combination of polarizer and analyzer is used to achieve an attenuation of 50000. Once the pulses are polarized, the 1st pulse is circularly polarized using a low-order quarter wave ($\lambda/4$) plate. The axis of the $\lambda/4$ plate is identified using a GT polarizer-analyzer combination to an attenuation factor of about 50000. We get LCPL and RCPL by turning the $\lambda/4$ by $+45^\circ$ and -45°. To analyze the circularly polarized light we use Fresnel Rhomb. Fresnel Rhomb converts circularly polarized light to linearly polarized light, and vice versa.

After $\lambda/4$ plate converts linearly polarized light to circularly polarized light, Fresnel Rhomb converts it back to linearly polarized light which can be analyzed through a GT analyzer. The better the $\lambda/4$ plate makes circularly polarized light, the better the attenuation through the analyzer.

6.4 References

[1] van Amerongen, H., Valkunas, L., and van Grondelle, R. *Photosynthetic Excitons*; World Scientific: Singapore, 2000.

[2] Hu, X. C., Ritz, T., Damjanovic, A., and Schulten, K. (1997) Pigment organization and transfer of electronic excitation in the photosynthetic unit of purple bacteria. *Journal of Physical Chemistry B 101*, 3854–3871.

[3] Sundstrom, V., Pullerits, T., and van Grondelle, R. (1999) Photosynthetic light-harvesting: Reconciling dynamics and structure of purple bacterial LH2 reveals function of photosynthetic unit. *Journal of Physical Chemistry B 103*, 2327–2346.

[4] Cho, M., Vaswani, H. M., Brixner, T., Stenger, J., and Fleming, G. R. (2005) Exciton Analysis in 2D Electronic Spectroscopy. *The Journal of Physical Chemistry B 109*, 10542–10556.

[5] Abramavicius, D., and Mukamel, S. (2006) Chirality-induced signals in coherent multi-dimensional spectroscopy of excitons. *Journal of Chemical Physics 124*, 004MR Times Cited:21 Cited References Count:72.

[6] Choi, J.-H., and Cho, M. (2007) Quadrupole contribution to the third-order optical activity spectroscopy. *The Journal of Chemical Physics 127*.

[7] Frank, H. A., Chadwick, B. W., Oh, J. J., Gust, D., Moore, T. A., Liddell, P. A., Moore, A. L., Makings, L. R., and Cogdell, R. J. (1987) Triplet-triplet energy transfer in

B800850 light-harvesting complexes of photosynthetic bacteria and synthetic carotenoporphyrin molecules investigated by electron spin resonance. *Biochimica et Biophysica Acta (BBA) - Bioenergetics 892*, 253 – 263.

[8] Harel, E., Fidler, A. F., and Engel, G. S. (2010) Real-time mapping of electronic structure with single-shot two-dimensional electronic spectroscopy. *Proceedings of the National Academy of Sciences of the United States of America 107*, 16444–16447.

[9] Singh, V. P., Fidler, A. F., Rolczynski, B. S., and Engel, G. S. (2013) Independent phasing of rephasing and non-rephasing 2D electronic spectra. *Journal of Chemical Physics 139*, 211RO Times Cited:4 Cited References Count:25.

[10] Dahlberg, P. D., Fidler, A. F., Caram, J. R., Long, P. D., and Engel, G. S. (2013) Energy Transfer Observed in Live Cells Using Two-Dimensional Electronic Spectroscopy (vol 4, pg 3636, 2013). *Journal of Physical Chemistry Letters 4*, 3977–3977, 259WS Times Cited:0 Cited References Count:1.

CHAPTER 7

FUTURE DIRECTIONS

In the previous chapters I presented work on technical and theoretical advances that, along with other developments, have helped in making GRAPES a powerful spectrometer. I presented work where such advances were very crucial in addressing outstanding questions in coherent ultrafast energy transfer dynamics of light harvesting complexes. But perhaps the most exciting development that GRAPES has brought about is development of Chiral Two-Dimensional Electronic Spectroscopy (C2DES).[1] C2DES has enabled us to encode delocalization dynamics of excited states along with its ultrafast dynamics. Further application of C2DES led to the discovery of chiral dynamics in light harvesting complex 2 (LH2). C2DES can make significant contributions towards understand ultrafast dynamics of excitons if it is applied to study other light harvesting complexes such as LH1, LHC2 and whole cells. Such studies require enabling GRAPES to perform C2DES experiments over a wide range of wavelengths. Below, I propose an alternate design for GRAPES to enable it to perform C2DES experiments over a broad range of wavelengths. I also talk about future applications of C2DES in ultrafast dynamics and photochemical reactions.

7.1 Development of broad band Chiral Two-Dimensional Electronic Spectroscopy

One of the challenges in performing C2DES experiments is maintaining polarization of the pulse in broad band experiments. The difficulty in these experiments is two fold. First, pulse's polarization is usually controlled using $\lambda/4$ or $\lambda/2$ waveplates, that operate within a relatively narrow bandwidth. Second, working with broad band pulses necessitates use of silver mirrors instead of dielectric mirrors. However silver mirrors add ellipticity to the polarization of the pulse.

In order to overcome these difficulties we need to bring about changes in GRAPES

geometry and using optical elements other than waveplates to control polarization. Figure 7.1 shows the current GRAPES geometry for performing C2DES experiments.[2;3] The GRAPES mirrors GM1, GM23 and GM4 direct the beams towards the sample and the signal is acquired in the rephasing direction. Figure 7.1(b) is a simplified ray diagram to show how wedge optics WO12 and WO34, and the GRAPES mirrors are aligned to acquire the signal in the rephasing direction.

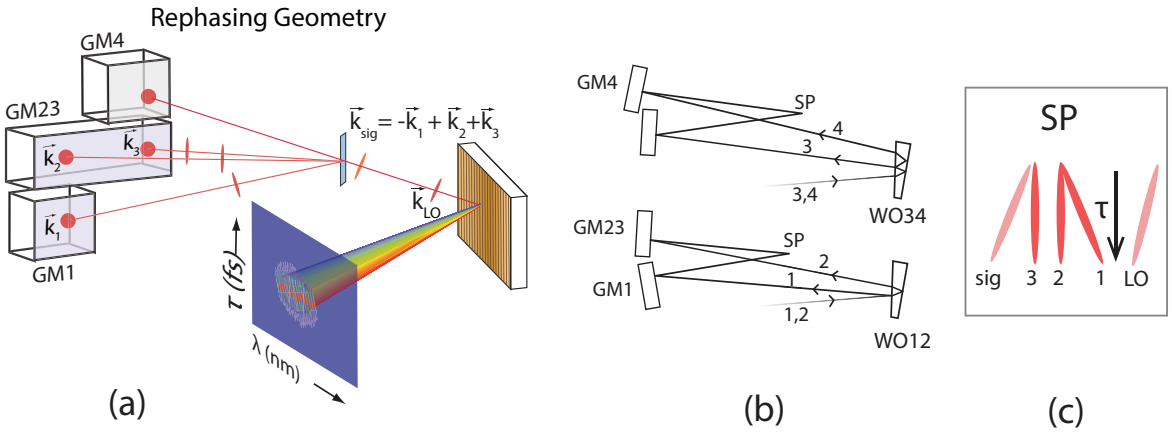

Figure 7.1: (a) Old geometry of GRAPES for acquiring rephasing signals. Beam 1 bounces off mirror labeled GM1, beam 2 and 3 bounce off mirror labeled GM34 and beam 4 bounces off mirror labeled GM4. (b) The alignment of wedge optics, WO12 and WO34, that make copies of pulses by taking from and back reflection of the incoming pulse. WO12 gives pulse 1 and pulse 2. WO34 gives pulse 3 and pulse 4. The mirrors GM1, GM23 and GM4 direct the beams 1, 2, 3 and 4 at the sample position labeled SP. (c) Timing of beams at the sample position, SP.

The first step in improving the quality of polarization is use a couple of Glan-Thompson polarizers in the path of beams 1-2 and 3-4 before they hit WO12 and WO34. The use of Glan-Thompson polarizer helps to remove ellipticity that may be present in the beams. After the beams bounce off WO12 and WO34 the beams 1,2,3 and 4 propagate along non-parallel paths. While the beams 2,3 and 4 are linearly polarized as needed, beam 1 has to be circularly polarized. In the current geometry, a $\lambda/4$ waveplate is used to convert linearly polarized beam 1 to circularly polarized. The use of waveplate limits the bandwidth that can be used in the experiments. In the proposed new geometry, use of Fresnel rhomb will enable C2DES in the broadband regime. However Fresnel rhomb shifts the path of the incoming

beam as shown in figure 7.2(b). This necessitates moving GM1 from below GM23 to above GM23, as shown in figure 7.2(a). In order to acquire rephasing signal in the $-\vec{k}_1 + \vec{k}_2 + \vec{k}_3$ direction, we have to take redefine the local oscillator. Instead of taking the second back reflection from WO34, if we take the front reflection from WO34 and move GM4 from above GM34 to below GM34, then beam 4 propagats in the direction $-\vec{k}_1 + \vec{k}_2 + \vec{k}_3$ and can be used as a local oscillator. Moving GM1 above GM23 and GM4 below GM23 reverses the

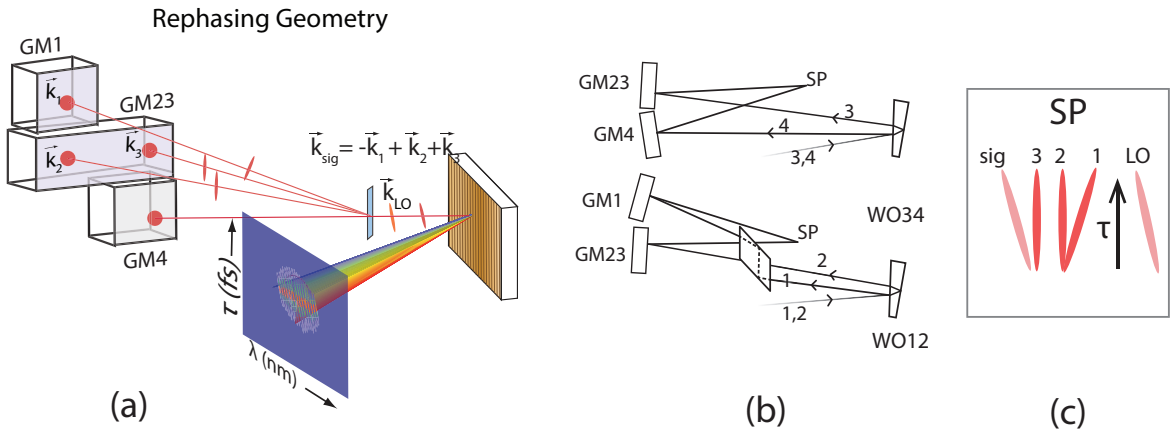

Figure 7.2: (a) New geometry of GRAPES for acquiring rephasing signals. Beam 1 bounces off mirror labeled GM1, beam 2 and 3 bounce off mirror labeled GM34 and beam 4 bounces off mirror labeled GM4. (b) The alignment of wedge optics, WO12 and WO34, that make copies of pulses by taking from and back reflection of the incoming pulse. WO12 gives pulse 1 and pulse 2. WO34 gives pulse 3 and pulse 4. The mirrors GM1, GM23 and GM4 direct the beams 1, 2, 3 and 4 at the sample position labeled SP. (c) Timing of beams at the sample position, SP.

direction in which coherence time τ is encoded at the sample position as shown in figure 7.2 (compared to figure 7.1(c)). Figure 7.3 compares the beams as they get focused into the sample. The top and the bottom row give a lens view of phase matching condition in the current and proposed geometry for performing broadband C2DES with GRAPES.

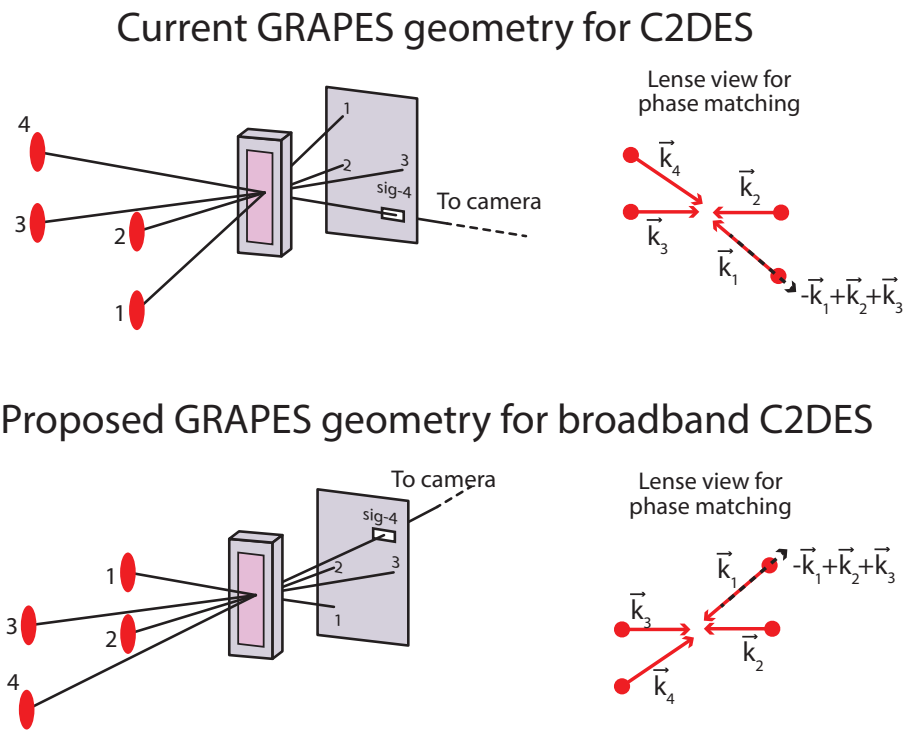

Figure 7.3: Top row shows the current geometry of GRAPES at the sample position. Bottom row shows the proposed geometry for broadband C2DES with GRAPES

7.2 Simultaneous study of photosynthetic antenna complexes and metal nano-particles

Light harvesting complexes are studied to understand the design principles that make energy transfer efficient, so that these design principles could be incorporated into artificial systems to address the problem of renewable energy. There is also a lot of experimental effort put into understanding ultrafast dynamics of nano-materials for the same reason. Combining light harvesting complexes with nano-materials can bring about significant advances in our understanding of both, light harvesting complexes and nano-materials.

Metal nano-particles provide high dielectric medium and hence enhanced electromagnetic field in its vicinity. Such high dielectric medium has resulted in many interesting phenomena such surface-enhanced Raman spectroscopy and surface-enhanced infrared absorption. Lately, there have been reports on enhanced circular dichroism, in chiral as well as achiral

substrate molecules. Circular dichroism (CD) has a special place among other forms of spectroscopy because CD spectroscopy is more sensitive to structure when compared with other forms of spectroscopy. Therefore it is intutive to combine CD spectroscopy with ultrafast spectroscopy if we want to understand the effect of structure on ultrafast dynamics. However, this idea has met with a lot of technical challenge. First and fore-most is the extremely weak strength of CD signals. Docking light harvesting complexes on metal nanoparticles will significantly improve the strength of CD signals and enable study of ultrafast dynamics with information from circular dichroism encoded in it.

7.3 References

[1] Fidler, A. F., Singh, V. P., Long, P. D., Dahlberg, P. D., and Engel, G. S. (2014) Dynamic localization of electronic excitation in photosynthetic complexes revealed with chiral two-dimensional spectroscopy. *Nature communications 5*.

[2] Harel, E., Fidler, A. F., and Engel, G. S. (2010) Real-time mapping of electronic structure with single-shot two-dimensional electronic spectroscopy. *Proceedings of the National Academy of Sciences of the United States of America 107*, 16444–16447.

[3] Singh, V. P., Fidler, A. F., Rolczynski, B. S., and Engel, G. S. (2013) Independent phasing of rephasing and non-rephasing 2D electronic spectra. *Journal of Chemical Physics 139*, 211RO Times Cited:4 Cited References Count:25.

CHAPTER 8

CONCLUSIONS

In this thesis I have enumerated various technical and theoretical developments that have taken place over the past few years in ultrafast spectroscopy, and the application of these techniques and theories to address the curious phenomena of efficient energy transfer in light harvesting complexes, in particular Light Harvesting Complex 2 (LH2). The goal of these spectroscopic techniques is to understand biology's underlying design principles that transpire efficient energy transfer and to incorporate those designs in synthetic systems to harvest solar energy.

I introduced the problem of efficient energy transfer in photosynthetic organisms in chapter 1, and described the properties of Light Harvesting Complex 2 (LH2) in great detail. I also described the two limits common mechanisms of energy transfer - Förster Resonance Energy Transfer (FRET) and Redfield mechanism of energy transfer, and how they are related to the governing principles of energy transfer that is succinctly captured by Fermi's golden rule. Further, in chapters 2 and 3, I explain non-linear spectroscopic techniques and a theoretical construct that helps to interpret spectroscopic signals.

In chapter 4 I describe Gradient assisted photon echo scpectroscopy (GRAPES) as a particular realization of two dimensional electronic spectroscopy. Compared to other spectrometers, GRAPES is unique in how it encodes timing between pulses by creating a spatial gradient between them, and then acquiring rephasing signal in the $-\vec{k}_1+\vec{k}_2+\vec{k}_3$ direction. As initially designed, GRAPES did not acquire non-rephasing signals. However, non-rephasing signals are required along with rephasing signals for phasing - a procedure to determine relative phase of spectroscopic signals. Lack of non-rephasing signals posed a conceptual barrier to phasing signals. Contrary to this commonly held belief, I was able to show using the projection slice theorem that rephasing and non-rephasing signals can be phased independently by comparing each to spectrally resolved pump-probe spectra. This proof operates both inside and outside the impulsive limit. I additionally corroborated my phasing procedure

with simulation, and further used a new GRAPES geometry to acquire non-rephasing signal as well.

GRAPES, being a single shot technique, enabled measuring weak signals with good signal-to-noise ratio. I used GRAPES' signal-to-noise ratio to solve one of the most fiercely debated problems in recent years in the field of coherent energy transport which is the nature of coherence observed during energy transfer. The coherence signals were initially interpreted as electronic coherence. Theoretical work showed that electronic coherence can enhance quantum efficiency in energy transfer. However, there were alternate interpretations of coherence as well - that these coherence can be vibrational in nature because vibrational coherence will comply with experimental findings as well. In chapter 5 I presented an experimental design that could distinguish between electronic and vibrational coherence. I showed that vibrational coherence are neither vibrational nor electronic, but vibronic resulting from coupling between vibrational and electronic states and breaking of Born-Oppenheimer approximation. I also developed a theoretical construct to estimate vibronic coupling.

Finally, in chapter 6 I address the issue of chirality in light harvesting complexes. Chirality is of light harvesting complexes is a ubiquitous property across different photosynthetic species. But it has not been sufficiently investigated for its effect on energy transfer dynamics. I designed experiments that revealed the role of chirality in energy transfer dynamics. The experimental results reveal that chirality significantly affects energy transfer dynamics through two mechanisms that were previously unknown. First, chirality enhances circular dichroism in a densely packed system of chromophores, such as LH2. Second, chirality affects dynamics of states with opposite angular momentum.